



HAL
open science

Modelization of dry friction damping in assembled structures

Yifan Yang

► **To cite this version:**

Yifan Yang. Modelization of dry friction damping in assembled structures. Other. Université de Lyon, 2018. English. NNT : 2018LYSEC044 . tel-02110806

HAL Id: tel-02110806

<https://theses.hal.science/tel-02110806>

Submitted on 25 Apr 2019

HAL is a multi-disciplinary open access archive for the deposit and dissemination of scientific research documents, whether they are published or not. The documents may come from teaching and research institutions in France or abroad, or from public or private research centers.

L'archive ouverte pluridisciplinaire **HAL**, est destinée au dépôt et à la diffusion de documents scientifiques de niveau recherche, publiés ou non, émanant des établissements d'enseignement et de recherche français ou étrangers, des laboratoires publics ou privés.



Numéro d'ordre NNT : 2018LYSEC044

Année : 2018

**THÈSE DE DOCTORAT DE L'UNIVERSITÉ DE LYON
OPÉRÉE AU SEIN DE L'ÉCOLE CENTRALE DE LYON**

**ÉCOLE DOCTORALE MEGA
Mécanique, Energétique, Génie civil et Acoustique**

Spécialité : Mécanique appliquée

Soutenue le 13/12/2018 par

Yifan YANG

Modelization of dry friction damping in assembled structures

Devant le jury composé de :

Sébastien BERGER	Professeur, INSA Val de Loire	Rapporteur
Scott COGAN	Chargé de Recherche, HDR, FEMTO-ST	Rapporteur
Philippe BRISTIEL	Ingénieur de Recherche, Expert Mécanique Numérique, Groupe PSA	Examineur
Thouraya BARANGER	Professeure, Polytech Lyon, Université Claude Bernard Lyon 1	Présidente
Olivier DESSOMBZ	Maître de Conférences, LTDS-ECL	Co-encadrant
Louis JÉZÉQUEL	Professeur, LTDS-ECL	Directeur de thèse

To my parents and girl friend

Acknowledgements

I would like to express in the first place my gratefulness to my thesis director Louis JÉZÉQUEL for his inspirational ideas and profound understanding of mechanics. His serious attitude towards the rigorousness of science and endless pursuit of innovation will be an unlimited driving power for my career development. At the same time, I would also like to thank him for the insights and wisdom on life that he has shared with me during the countless coffee/bear breaks. His perseverance in front of difficulties and his gut feeling in solution-finding will be one of the most important lighthouses in my spiritual world.

Secondly I owe my gratitude to my thesis co-director Olivier DESSOMBZ for his help on numerical simulation and information systems throughout my thesis, without which the preliminary try test on contact modelization would be much more difficult. I would also like to thank him for his adventurous experiences that he has shared with me. They have given me the passion to discover the world.

Thirdly, I am grateful for my tutor Philippe BRISTIEL in PSA. He has helped me a lot on the application of the proposed method in the industrial environment. The improvement that he has brought to the algorithm greatly reduces the calculation time and makes it possible for the analysis of more complex structures.

Then I would like to give my thanks to Stéphane and Lionel for their help on the experiment setup's design and assembly, as well as the tuning of the measurement system. It has enabled me to obtain a qualitatively satisfactory experimental verification of the proposed theory.

Finally, it is my privilege to thank my parents for their financial and spiritual support all along my studies from my first day in the primary school to the defense of my Ph.D. thesis. I would also like to thank my girlfriend for being with me at the most chaotic and hardest period of my doctoral studies. She has helped me refind my own life and focus on what really matters to me.

Finishing my doctoral studies is not an end, it's a new start for a lifelong pursuit of wisdom and truth.

Yifan YANG
Rueil-Malmaison, 08/03/2019

Abstract

Keywords: damping, dry friction, nonlinear mode, vibration, numerical method

The determination of a component's lifetime under vibrational excitation is one of the most difficult challenges in mechanical engineering. In order to provide a reliable estimation of lifetime, a correct calculation of stress field, which depends on the modal form and its amplitude, is needed. However, the vibrational response calculation on an assembled structure is not easy, especially with the nonlinear structural damping induced by frictional contact surface. The research in the current thesis starts from the phenomenological identification of damping with the help of 3 analytical models, in particular the sandwich plate, rotational joint and von Karman plate. Structural damping of 1st and 2nd order are identified. The influence of parameters like clamping pressure, thickness ratio and number of welding points are also analyzed. The second part of the research focuses on problems with finite dimensions. The von Karman plate serves as the subject of the study and a hybrid method which combines FDM and FEM is proposed to solve the coupling between deflection and in-plane force field. A special attention is paid to nonlinear mode theory, the conditions under which the nonlinear mode is necessary are identified. The fictive force field proposed in the study of von Kármán plate is then applied to the sandwich plate model. The slipping's propagation as well as the influence of fictive force field are studied. To verify the existence of the found phenomena in the previous studies, an experimental setup is designed and mounted for the 1st order structural damping. In the last part of the research, which is based on the observations previously obtained from academic models, a calculation method of friction-induced damping in structures with complex geometries is proposed for the application in the industrial environment. This methods enables the estimation of damping for each isolated mode.

Résumé

Mots-clés : amortissement, frottement sec, mode nonlinéaire, vibration, méthode numérique

Déterminer la durée de vie d'une pièce sous excitation vibratoire est l'un des enjeux majeurs dans l'ingénierie mécanique. Afin de donner une estimation fiable de la durée de vie, un calcul correct de champ de contrainte, qui est fortement lié à la forme et l'amplitude modale est obligatoire. Cependant, le calcul de réponse d'une structure assemblée est difficile, surtout avec la présence de frottement sec aux interfaces de liaisons qui entraîne un amortissement non linéaire. La recherche de la thèse commence par une identification phénoménologique de l'amortissement induit par le frottement sec avec 3 modèles analytiques, notamment la plaque sandwich, la rotule frottante et la plaque von Kármán. Après la caractérisation de l'amortissement structural au 1er et 2ème ordre, les influences des paramètres comme la pression de serrage, le rapport d'épaisseurs ainsi que le nombre de soudures sont analysés. La deuxième partie des travaux traite les problèmes d'amortissement avec une géométrie de dimension finie. La plaque de von Kármán est reprise dans l'étude et une méthode hybride de différences finies et d'éléments finis est adopté pour résoudre le couplage entre la flexion et les efforts internes. Une attention particulière est portée à la notion de modes non linéaires dans le cas de la plaque von Kármán. Les conditions nécessitant l'introduction de modes non linéaires sont identifiées. Le champ de force fictif qui est proposé dans l'étude sur la plaque von Kármán est ensuite introduit dans le cas de la plaque sandwich. Puis la propagation de glissement et l'influence de champ fictif sont étudiées. Afin de vérifier les phénomènes trouvés dans les études théoriques, une installation expérimentale est conçue et montée pour l'amortissement structural au premier ordre. Dans la dernière partie qui est basée sur les observations faites dans les études précédentes, une méthode de calcul de l'amortissement dans un environnement industriel est proposée. Cette méthode permet de donner un amortissement pour chaque mode isolé.

Contents

General introduction	xv
1 Introduction	1
1.1 Undamped and damped vibration	2
1.2 Damping sources	3
1.3 Damping categories	4
1.4 Energy dissipation in viscoelastic material	5
1.5 Energy dissipation in hysteretic damping	6
1.6 Logarithmic decrement	8
1.7 Relation to logarithmic decrement	9
1.8 Slip damping mechanism	11
1.9 Literature review	13
1.9.1 Analytical methods	13
1.9.2 Numerical methods	21
1.9.3 Air damping	26
1.10 Conclusion	28
2 Phenomenological study of friction damping	29
2.1 Introduction	29
2.2 First-order interface damping in sandwich beam	30
2.2.1 Analytical modelization	30
2.2.2 Analytical parametric studies	37
2.2.3 Numerical parametric studies	41
2.3 First-order boundary damping in rotational joint	49
2.3.1 Analytical modelization	49
2.3.2 Analytical parametric studies	52
2.4 Second-order boundary damping in von Kármán plate	54
2.4.1 Geometric derivation of simplified Green strain	54
2.4.2 Analytical modelization	55
2.4.3 Analytical expression of slipping boundary's trajectory	59
2.4.4 Analytical parametric studies	63
2.5 Conclusion	66
3 Semi-analytical methods of damping modelization	69
3.1 Introduction	69
3.2 Damping induced by second-order bending strain in von Kármán plate	70
3.2.1 Formulation of fictive force field	70
3.2.2 Discrete method of derivatives' evaluation	72
3.2.3 Friction properties	74
3.2.4 Solution procedure	75

3.2.5	Analytical solution of clamped-clamped plate	79
3.2.6	Analytical solution of clamped-slipping plate	80
3.2.7	Numerical solution of clamped-clamped plate	81
3.2.8	Numerical solution of clamped-slipping plate	85
3.2.9	Extension to non-linear mode	89
3.2.10	Multi-mode method with complete slipping boundary	90
3.2.11	Multi mode method with non-uniform clamping pressure	91
3.2.12	Multi mode method with half slipping boundary	92
3.3	Damping induced by first-order cross section's rotation in sandwich plate	96
3.3.1	Model description	96
3.3.2	Shear force field formulation	97
3.3.3	Solution procedure and displacement kinematics	98
3.3.4	Sticking-slipping evolution	101
3.3.5	Calculation of damping ratio	103
3.3.6	Influence of second-order fictive force field	106
3.4	Conclusion	106
4	Experiment	109
4.1	Introduction	109
4.2	Specimen design	110
4.3	Measurement system	113
4.4	Rubber washer's stiffness measurement	114
4.5	Clamping pressure's calculation	116
4.6	Dynamic model of seismic system	117
4.7	Alternative method for damping identification	118
4.8	Experiment results	120
4.9	Conclusion	124
5	Methods for industrial application	127
5.1	Introduction	127
5.2	Mode shape injection method	127
5.3	Application on infinite flat plate	130
5.4	Application on infinite curved plate	134
5.5	Application on 3D structure	136
5.6	Conclusion	138
6	General conclusion	139
A	Second order derivatives schemes	143
	List of publications	145
	Bibliography	147

List of Figures

1.1	Structures under vibrational solicitation	1
1.2	Response of a 1-DOF undamped system	3
1.3	Response of a 1-DOF damped system	3
1.4	Hysteresis loop in terms of stress and strain	6
1.5	Hysteresis loop in terms of stress and strain	7
1.6	Spring-viscous-damper system	7
1.7	Energy balance in a damped system	9
1.8	Slipping categories	11
1.9	Experimental configurations to determine slip damping	12
1.10	Analytical model used by Williams	14
1.11	Analytical model used by Earles	15
1.12	Jointed cantilever beam used by Masuko	15
1.13	Experimental verification of jointed beam	16
1.14	Jointed cantilever beam used by Masuko	17
1.15	Study on multi-layered joined beam	18
1.16	Damping study on von Kármán plate	18
1.17	Pinned-pinned beam with sliding constraint	19
1.18	Damping study on von Kármán plate	20
1.19	Damping study on sectioned beam and its result	21
1.20	Node-to-node contact	22
1.21	Application of thin layer element	24
1.22	Four bolt modelization methods	25
1.23	Node-to-node contact	27
2.1	Sketch of jointed sandwich beam	30
2.2	Free body diagram of the sandwich beam	31
2.3	Partially clamped beam	35
2.4	Influence of pressure on damping ratio	37
2.5	Influence of coefficient of friction on damping ratio	38
2.6	Influence of global contact quality on damping ratio	39
2.7	Influence of clamping pad's position on damping ratio	40
2.8	Influence of clamping pad's area on damping ratio	41
2.9	Influence of welding points number on dissipated and stocked energy	42
2.10	Influence of welding points number on damping ratio	43
2.11	Influence of thickness ratio on dissipated and stocked energy	44
2.12	Influence of thickness ratio on damping ratio	44
2.13	Illustration of protrusions on contact surface	45
2.14	Influence of protrusion's height on dissipated and stocked energy	45
2.15	Influence of protrusion's height on damping ratio	46
2.16	Influence of protrusion's number on dissipated and stocked energy	47

2.17	Influence of protrusion's number on damping ratio	47
2.18	Influence of endpoint locking on dissipated and stocked energy	48
2.19	Influence of endpoint locking on damping ratio	49
2.20	Sketch of rotational damping beam	50
2.21	Decomposition of slipping state in rotational damping	50
2.22	Influence of pressure on rotational damping	53
2.23	Influence of clamping pad's radius on rotational damping	53
2.24	Geometric illustration of Green strain	54
2.25	Sketch of boundary friction model	56
2.26	The position of phase 1	59
2.27	The position of phase 2	60
2.28	The position of phase 3	61
2.29	The position of phase 4	62
2.30	Slipping boundary trajectories under 3 different pressures	62
2.31	Influence of clamping pressure on damping ratio	63
2.32	Influence of coefficient of friction on damping ratio	65
2.33	Influence of contact area on damping ratio	65
3.1	Mesh for finite element method and derivatives calculation	72
3.2	Derivatives comparison between FDM and analytical expression	74
3.3	Clamped-clamped plate model	79
3.4	Finite element model of clamped-clamped plate	82
3.5	Fictive force field from the first mode	82
3.6	Comparison of nonlinear term $R(N_i, \phi_i)$ between analytical and numerical method	83
3.7	Psi_{ii} obtained by analytical and numerical method	83
3.8	λ obtained from analytical and numerical solution	84
3.9	Fictive force field of the first mode shape	84
3.10	λ and η versus modal amplitude	85
3.11	Frequency response curve under three different modal forces	85
3.12	Rectangular plate with one slipping boundary	86
3.13	Trajectories comparison	86
3.14	Average frictional force and displacement on the slipping edge	87
3.15	Comparison of nonlinear term $R(N_i, \phi_i)$ between sticking and slipping phase	87
3.16	Comparison of nonlinear term ψ_{ii} between sticking and slipping phase	88
3.17	λ and η versus modal amplitude	88
3.18	Frequency response curve with one slipping boundary	89
3.19	The three retained linear modes	91
3.20	Rectangular plate with non-uniform clamping pressure	92
3.21	Influence of clamping pressure distribution of λ and η evolution	92
3.22	Rectangular plate with half slipping boundary	93
3.23	The three retained linear modes	93
3.24	Fictive force fields of the three linear modes	93

3.25	Participation factors with half slipping boundary	94
3.26	Influence of mode shape change on λ and η evolution	94
3.27	Excitation force position on the plate	95
3.28	Influence of mode shape change on frequency response	96
3.29	3D sandwich model	96
3.30	Shear stress on contact interface	97
3.31	Shear stress field on contact interface	98
3.32	Displacement components	100
3.33	Fictive force field of first mode in sandwich plate	101
3.34	Displacement components	101
3.35	The evolution of slipping state with the increase in modal amplitude	102
3.36	Slipping state at $q = 5$	103
3.37	η evolution obtained by numerical and analytical methods	105
3.38	η evolution under real numerical and approximated analytical mode shape	105
3.39	η evolution with and without second-order fictive force field	106
4.1	Cantilever sandwich beam specimen	110
4.2	Optimal position for maximum damping at $q = 1$ mm	112
4.3	Finite element analysis of specimen	112
4.4	Mechanical model of subsystem	113
4.5	Measurement system set-up	113
4.6	Measurement system set-up	114
4.7	Rubber washer's stiffness measurement	115
4.8	Rubber stiffness calculation	115
4.9	Rubber washer's stiffness measurement	116
4.10	Seismic system	117
4.11	Dynamic mass-spring model	119
4.12	Frequency response curve under 4.35 MPa	120
4.13	Frequency response curve under 2.74 MPa and 0.67 MPa	121
4.14	Frequency response curve under 2.74 MPa and 0.67 MPa	122
4.15	Theory-experiment comparison under 4.35 MPa and 0.67 MPa	122
4.16	Theory-experiment comparison under three different pressures	123
5.1	Illustration of the load case for industrial application	128
5.2	Mode shape injection methods	129
5.3	Mesh on flat plate	130
5.4	Normalized mode shapes to generate interface damping	130
5.5	Mesh on flat plate	131
5.6	Hysteresis loops of first mode	132
5.7	Hysteresis loops of second mode	132
5.8	Accumulated energy dissipation of mode 1 and mode 2	133
5.9	Energy dissipation on hysteresis loop	134
5.10	Mesh on curved plate	134

5.11 Mode shapes of curved infinite plate	135
5.12 Hysteresis loops of curved plate	135
5.13 Accumulated energy dissipation in curved plate	136
5.14 Geometry of the 3D model	136
5.15 Mode shape and imposed displacement region	137
5.16 Mode shape and imposed displacement region	138

List of Tables

2.1	Beam dimensions and mechanical properties	37
3.1	First derivatives schemes	73
4.1	Beam dimensions and mechanical properties	111
4.2	Resonance frequencies under $\mu = 0$ and $\mu = \infty$	112
4.3	Components' thickness	116
4.4	Pressures on the left clamp	117
4.5	Pressures on the right clamp	117
4.6	Pressures chosen	117
A.1	Second order derivatives schemes	143

General introduction

The vibration behavior of mechanical assemblies is always a subject with the implication of complex nonlinearity not only for academic researchers but also for industrial engineers. The current thesis will focus on the aspect of modelization of dry friction damping on the contact surface. Damping is considered as a key factor which regulates the vibration amplitude as well as the consequently dependent property of fatigue resistance. A good and reliable modelization of the damping value can contribute to a precise estimation of the vibration response. The current thesis adopts a progressive approach in the study. It starts from a fundamental phenomenological study of friction damping realized mainly by analytical models, then a more refined model built by FEM is proposed to study the nonlinear aspects induced by friction damping, at last the retained conclusions in the previous chapters serve as the basis for the development of a simplified method for industrial applications. The content of the thesis is divided into 5 chapters, the main idea of each chapter is presented below.

Chapter 1 gives in the first place a general introduction of the notion of damping in vibration systems. The difference between viscous damping and friction damping is presented by mathematical demonstrations. The metric of damping – logarithmic decrement or damping ratio, are explained in details and the relationship between them is established. The literature review presents in a chronological order the state of the art of damping modelization. The modeling approaches can be divided into two categories: analytical methods and numerical methods. The concrete examples and important conclusions are also presented.

Chapter 2 is dedicated to the phenomenological study of friction damping on the basis of three academic models, the development of which is inspired by the analytical models that have been used in the literature, namely infinite sandwich plate, rotational joint and von Kármán plate. The three models are all analytical and will enable a parametric study of influencing parameters like clamping pressure and coefficient of friction. The influences of other parameters like thickness ratio, curvature of contact surface as well as boundary condition are analyzed by FEM on the infinite sandwich plate. The phenomenological study gives a preliminary view of the friction damping and reveals its dependence on modal amplitude. According to the evolution of damping ratio in terms of the magnitude of displacement, the friction damping can be categorized into first-order damping and second-order damping.

Chapter 3 is a further research based on the discovered phenomena presented in chapter 2. It mainly deals with the planarization of friction problems in structures having geometry nonlinearity, namely the von Kármán plate. Considering the difficulty in analytical solution, FEM and FDM are adopted in the discretized

formulation of the problem. The hardening/softening effect due to in-plane forces as well as its influence on nonlinear mode coupling will be discussed. The notion of planarization of contact problems will then be extended to the sandwich plate with finite dimensions and the results obtained will show that the planarization will give a satisfactory estimation of damping ratio compared to analytical method.

Chapter 4 is an experimental verification of the phenomena revealed in the previous chapters. A partially clamped symmetric sandwich plate is adopted as the experiment specimen. The advantages of the symmetric structure will be presented and the design procedure will be explained. The experiment results will show that frictional damping is sensitive to clamping pressure and model amplitude. The $\eta - q$ curves found in the experiment gives the same variation tendency in terms of displacement as predicted by the numerical and analytical methods.

Chapter 5 will propose an simplified method for damping modelization within the framework founded on the conclusions from the previous theoretical studies, i.e. the resonance frequency along with the mode shape cannot be drastically changed by the presence of frictional contact, the damping is determined only by the linear mode shape and its corresponding amplitude. This simplification enables the engineers of PSA to calculate the damping associated with a given mode shape in a quasi-static way within the commercial FEM softwares. The proposed method is based on ABAQUSTM subroutine DISP which is capable of imposing an user-defined displacement to the structure according to the directions defined in the mode shape. The mode shape injection method will be applied in the first place on 2D models and then on an industrial-sized 3D model. The results will show that the proposed method is simple and efficient in damping estimation.

The current thesis is a complete study on frictional damping in assembled structures. It starts from the basic notions of frictional damping obtained in academic models and transits progressively to a simplified method for industrial application. I hope my work will be useful for scientists and engineers who are interested in the complexity of friction damping in assembled structures and shed light for the future research.

CHAPTER 1

Introduction

In the current industrial design, a key evaluation factor of the product is the fatigue resistance under vibrational solicitation, especially for domains where security and robustness are primordial criteria for clients, for example in automobile and aerospace industries. Apart from the security consideration, vibration also plays an important role for the comfort perceived by the clients. A relatively weak vibration level will surely give clients a feeling of reliability and high-end quality. The automobile constructor Groupe PSA spares no effort in the permanent perfection of its products, during the course of which the vibration reduction stays one of the most important research directions, especially for components like metallic body, drive train and suspension system. The proposal of the current thesis lies in this industrial context.



Figure 1.1: Structures under vibrational solicitation

However the prediction of vibrational behavior during the conception phase is still a difficult task, especially in operating conditions near the resonance. The difficulty is mainly due to the insufficiently understood damping property which is determinant for the vibration amplitude. Thus to understand even to correctly model damping properties is the final key to solve vibration problems.

Vibration analysis has already become a common practice in automobile engineering. The numerical tools in the realm of Computer Aided Engineering (CAE) have already been widely used in virtual conception before passing experiment verification. These tools are of good capacity to give a correct prediction of mass and inertia, and also a relatively precise estimation of stiffness, but they are incapable

of providing a convincing value of damping, notably for automobile structures with complex geometry and loading conditions. In this case, a bad prediction of damping will result in an incorrect estimation of amplitude and thus consequently an erroneous prediction of fatigue endurance, since the fatigue endurance is directly related to internal stress field which is proportional to displacement amplitude. In order to make up this default in design phase, the current thesis will mainly deal with the problematic encountered due to damping modelization.

Industrial structures are mostly assembled structures, they are often jointed together by welded or bolted connections. Damping in these structures can be roughly classified in two categories: viscous damping and structural or hysteresis damping. Compared to structural damping, the property of viscous damping is well understood and there exists already mature industrial applications like damping enhancement by the insertion of thin viscoelastic films or rubber washer, the damping mechanism in hydraulic damper also falls into the realm of viscous damping. However, according to different studies in the bibliography, structural damping is much more elevated than viscous damping in assembled structures, which is due to the fact that energy is mainly dissipated by relative displacement under friction between different components.

The objective of the current thesis is to understand the properties of frictional damping and find a proper way to modal energy dissipation in assembled structures. Based on the knowledge derived from academic models, application methods for industrial use are then to be developed. Before the research into the notion of frictional damping, some basic theories about damping and vibration mechanics are to be reviewed.

1.1 Undamped and damped vibration

Structure vibration can be regarded as an alternative energy transfer between kinematic energy and potential energy of deformation. If no energy is lost or dissipated in friction or other resistance during oscillation, the vibration is known as undamped vibration, where all the kinematic energy can be transformed into potential energy in one cycle. The equation which describes the undamped dynamic one-degree-of-freedom system without external excitation is written as

$$m\ddot{x} + kx = 0 \tag{1.1}$$

with m the mass and k the stiffness. The temporal response of such a system is illustrated in figure 1.2.

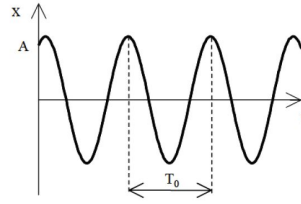


Figure 1.2: Response of a 1-DOF undamped system

If any energy is lost during the cycle, however, it is called damped vibration. In many physical systems, the amount of damping is so small that it can be disregarded for most engineering purposes. However, consideration of damping is becoming more and more important in analyzing vibratory systems near resonance. In many practical damped systems, the vibratory energy is gradually converted to heat or sound. Due to the reduction in the energy, the response, such as the displacement of the system, gradually decreases in the case without energy input. In the system with energy input, the existence of damping prevents the displacement from reaching infinity. Although the amount of energy converted into heat or sound is relatively small, the role that the damping plays is drawing more and more attention of researchers and engineers to have an accurate prediction of the vibration response, especially near resonance. The damped dynamic system with viscous damping can be written as

$$m\ddot{x} + kx + c\dot{x} = 0 \quad (1.2)$$

where $c\dot{x}$ is the damping force which signifies that viscous damping is in terms of velocity. The response of 1-DOF damped system with different damping coefficients is illustrated in 1.3.

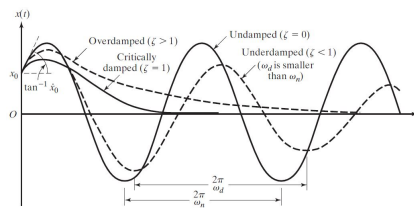


Figure 1.3: Response of a 1-DOF damped system

1.2 Damping sources

In real conditions, the undamped system presented in figure 1.2 doesn't exist, because the vibration amplitude always decreases with time due to different damping forces. These forces are in the opposite direction of movement and are thus of opposition sign to the velocity. As the structure is often exposed to complex environment, the attenuated response is the result of multiple damping sources. The damping sources can be categorized in the way below.

- External damping
 - Damping due to fluid-structure coupling: interaction between the structure in vibration and the fluid environment, for example air damping.
 - Damping due to element connected to the structure: usage of absorbent viscoelastic material, for example rubber washer and dry rub.
 - Damping due to passive, semi-active or active piezoelectric material: these materials are capable of transforming the deformation energy into electric energy or in the inverse direction. This reversibility enables to obtain intelligent systems in which a part of mechanical energy can be extracted from the system in order to control its vibration amplitude.
- Internal damping
 - Material damping: damping in the material is a complex process, it is believed that the energy dissipation comes from the dislocations of microscopic crystals and cracks. This dissipative mechanism is sensitive to temperature and frequency of the vibration. Material damping is relatively weak in metals or in mono-crystal materials.
 - Micro-slip damping: damping is generated by frictional micro-slip at the connection interface between components in assembled structures. The energy is mainly dissipated in the form of heat.

1.3 Damping categories

In order to model the damping property of vibratory systems, damping elements are introduced. A damper is assumed to have neither mass nor elasticity, and damping force exists only if there is relative velocity between the two ends of the damper. As it is difficult to include all the damping properties in one element, damping is modeled as one or more of the following types.

- **Viscous damping.** Viscous damping is the most commonly used damping mechanism in vibration analysis. When mechanical systems vibrate in a fluid medium such as air, gas, water, or oil, the resistance offered by the fluid to the moving body causes energy to be dissipated. In the amount of dissipated energy depends on many factors, for example the size and shape of the vibrating body. In viscous damping, the damping force is proportional to the velocity of the vibrating body. Typical examples of viscous damping include (1) fluid film between sliding surfaces, (2) fluid flow around a piston in a cylinder, (3) fluid flow through an orifice, and (4) fluid film around the journal of a bearing. The damping induced by "gaz-pumping" can be categorized as viscous damping.
- **Coulomb or dry-friction damping.** The damping force is constant in magnitude but opposite in direction to that of the motion of the vibrating

body. It is caused by friction between rubbing surfaces that are either dry or have insufficient lubrication.

- **Material or solid or hysteretic damping.** When a material is deformed, energy is absorbed and dissipated by the friction between the internal planes, which slip or slide as the deformations take place. When a body having hysteretic damping is subjected to vibration, the stress-strain diagram shows a hysteresis loop as shown in figure 1.5a. The area of this loop denotes the energy lost per unit volume of the body per cycle due to damping.

1.4 Energy dissipation in viscoelastic material

A viscoelastic material is characterized by possessing both viscous and elastic behavior. From a macroscopic point of view, the damping in viscoelastic material implies a conversion from mechanical energy to thermal energy due to the successive rearrangement of molecule chains when the structure is under deformation. In order to quantify the dissipation capacity of viscoelastic material, the loss factor $\eta(f)$ is employed to express its dependency on frequency. The Young's modulus of viscoelastic material can be expressed by a complex number

$$E^*(f) = E'(f) + iE''(f) = E'(f)[1 + \eta_E(f)]. \quad (1.3)$$

In the same way, the shear loss factor can be expressed from the shear modulus

$$G^*(f) = G'(f) + iG''(f) = G'(f)[1 + \eta_G(f)]. \quad (1.4)$$

$E'(f)$ and $G'(f)$ represent the modulus for energy stock while $E''(f)$ and $G''(f)$ are related to energy dissipation in the material. The relation between them is given by

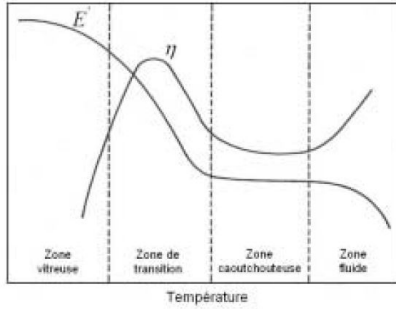
$$E^*(f) = 2(1 + \nu)G^*f. \quad (1.5)$$

Some materials have different loss factor for traction-compression and shear, however for others materials, only one loss factor is able to describe the vibration behavior. In this case we can write

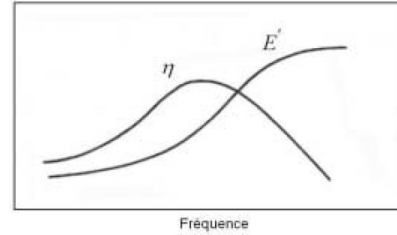
$$\eta_f = \eta_E = \eta_G. \quad (1.6)$$

It should be noted that the energy created on the microscopic level may not be evacuated on time, which will generate an temperature increase in the material. The temperature can modify the mechanical behavior of viscoelastic material in terms of the existence of glassy transition. It is found that the loss factor can reach its maximum in the transition phase when the rigidity experiences drastic change, as illustrated in figure 1.4a. The behavior on frequency is completely the inverse of that on temperature, as shown in figure 1.4b. Under low frequencies, the rigidity of the material is big, with the increase in frequency, the rigidity becomes bigger and

saturates to an asymptotic value. Between the two zones, there exists a transition frequency on which the loss factor of the material reaches its maximum [1].



(a) Influence of temperature on viscoelastic material



(b) Influence of frequency on viscoelastic material

Figure 1.4: Hysteresis loop in terms of stress and strain

1.5 Energy dissipation in hysteretic damping

When a force is applied on a body with frictional hysteretic damping, the loading and unloading curve don't coincide and forms a hysteresis loop. As the loading force increases, the stress σ and the strain ε also increase, the area under the $\sigma - \varepsilon$ curve, given by

$$E = \int \sigma d\varepsilon, \quad (1.7)$$

denotes the energy injected in per unit of the volume. When the load on the body is gradually removed, the elastic energy will be recovered. When the loading path is different from the unloading path, the area ABC in figure 1.5b is equivalent to the energy dissipated per unit volume of the body. The area inside the circle in figure 1.5a quantifies the total energy loss in one loading cycle. The hysteresis loop can also be formed with the magnitude of the loading force and the displacement of the excitation point. The damping capacity of different structures can easily be compared by the size of hysteresis loop under the same level of strain.

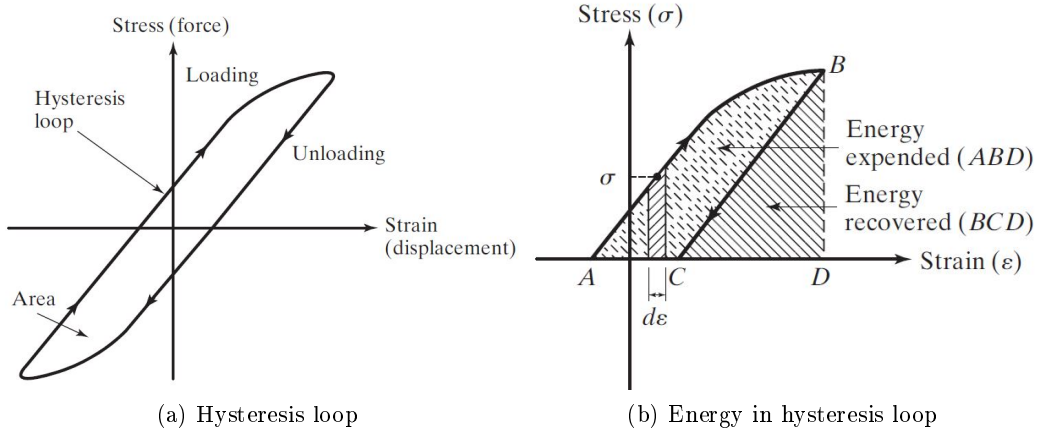


Figure 1.5: Hysteresis loop in terms of stress and strain

The quantification of hysteretic damping can start from the modelization of a spring-viscous-damper system in figure 1.6.

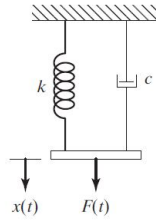


Figure 1.6: Spring-viscous-damper system

For this system, the force needed to to cause a displacement $x(t)$ is given by

$$F = kx + c\dot{x}. \tag{1.8}$$

For a harmonic motion of of frequency ω and amplitude X ,

$$x(t) = X \sin \omega t. \tag{1.9}$$

Equation 1.8 and 1.9 yield

$$\begin{aligned} F(t) &= kX \sin \omega t + cX\omega \cos \omega t \\ &= kx \pm c\omega \sqrt{X^2 - (X \sin \omega t)^2} \\ &= kx \pm c\omega \sqrt{X^2 - x^2} \end{aligned} \tag{1.10}$$

When F versus x curve plotted, it represents a closed loop, the area of the loop denotes the energy dissipated by the damper in a cycle of motion and is given by

$$\Delta W = \oint F dx = \int_0^{2\pi/\omega} (kX \sin \omega t + cX\omega \cos \omega t) (\omega X \cos \omega t) dt = \pi\omega cX^2. \quad (1.11)$$

It has been found experimentally that the energy loss in frictional hysteresis damping is independent of the frequency and proportional to the displacement, in order to achieve this observed behavior and establish an equivalence on the level of dissipated energy, we can introduce a hysteresis damping coefficient c_h , which is inversely proportional to the frequency.

$$c_h = \frac{h}{\omega}. \quad (1.12)$$

Replace c by c_h in equation 1.11, the hysteretic energy dissipation can thus be expressed as

$$\Delta W = \pi h X^2. \quad (1.13)$$

1.6 Logarithmic decrement

Logarithmic decrement is a temporal view of damping, it describes the amplitude decreasing rate in a direct way. In order to understand the basic meaning of damping, a clear explanation of logarithmic decrement is necessary. The following derivation is given by Rao [2]. Consider firstly the famous Euler limit

$$e^x = \lim_{n \rightarrow \infty} \left(1 + \frac{x}{n}\right)^n. \quad (1.14)$$

Replace x by $-\delta \cdot n$ where δ is the amplitude decreasing percentage in one cycle and n is the number of cycles.

$$e^{-\delta n} = \lim_{n \rightarrow \infty} (1 - \delta)^n. \quad (1.15)$$

The initial amplitude is denoted as X_1 , after n cycles of movement, the amplitude of cycle $n + 1$ can be expressed as

$$X_{n+1} = X_1(1 - \delta)^n. \quad (1.16)$$

If the number of cycles is infinitely big, the Euler limit can be used to establish the relationship between the initial amplitude and the final amplitude.

$$\begin{aligned} X_1 \lim_{n \rightarrow \infty} (1 - \delta)^n &= X_{n+1} \\ X_1 e^{-\delta n} &= X_{n+1} \end{aligned} \quad (1.17)$$

By applying a logarithmic function to both sides of equation 1.17 and solve for δ

$$\delta = \frac{1}{n} \ln\left(\frac{X_1}{X_{n+1}}\right). \quad (1.18)$$

If we take $n = 1$, the decreasing percentage per cycle, or the so-called logarithmic decrement can be written as

$$\delta = \ln\left(\frac{X_1}{X_2}\right) = \ln\left(\frac{X_n}{X_{n+1}}\right). \quad (1.19)$$

1.7 Relation to logarithmic decrement

If a spring and a hysteresis damper are connected in parallel, the reaction force can be expressed in a similar way as used in viscous damping

$$F = kx + i\omega c_h x = kx + ihx = k\left(1 + i\frac{h}{k}\right)x = k(1 + i\eta)x, \quad (1.20)$$

where $\eta = h/k$ and is a constant indicating a dimensionless measure of damping. We can substitute h in equation 1.8 by ηk .

$$\Delta W = \pi\eta k X_m^2. \quad (1.21)$$

Under hysteresis damping, the motion can be considered to be nearly harmonic, and the decrease in amplitude per cycle can be determined by using energy balance.

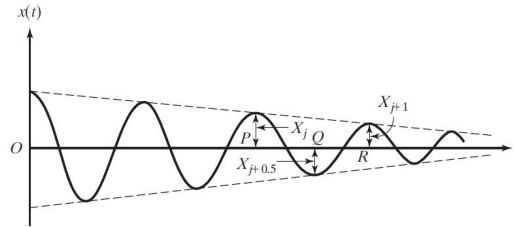


Figure 1.7: Energy balance in a damped system

The energy balance between point P and point Q can be expressed with the stocked elastic energy and dissipated energy.

$$\begin{aligned} \frac{1}{2}kX_j^2 - \frac{1}{4}\pi\eta kX_j^2 - \frac{1}{4}\pi\eta kX_{j+0.5}^2 &= \frac{1}{2}kX_{j+0.5}^2 \\ \frac{X_j}{X_{j+0.5}} &= \sqrt{\frac{2 + \pi\eta}{2 - \pi\eta}} \end{aligned} \quad (1.22)$$

From which

$$\frac{X_j}{X_{j+1}} = \frac{2 + \pi\eta}{2 - \pi\eta} = \frac{2 - \pi\eta + 2\pi\eta}{2 - \pi\eta} \approx 1 + \pi\eta. \quad (1.23)$$

Substitute equation 1.23 into equation 1.19 and suppose that $\pi\eta \ll 1$,

$$\delta = \ln(1 + \pi\eta) \approx \pi\eta. \quad (1.24)$$

Another way to express η is to use the ratio between dissipated energy and maximum stocked energy in one cycle, this ratio is also called specific damping capacity.

$$\frac{\Delta W}{E_{max}} = \frac{\pi\eta k X_m^2}{\frac{1}{2}k X_m^2} = 2\pi\eta \quad (1.25)$$

$$\eta = \frac{1}{2\pi} \frac{\Delta W}{E_{max}}. \quad (1.26)$$

The η is the damping capacity per radian and is named as loss coefficient. Substitute equation 1.23 into equation 1.21, we can express logarithmic decrement in terms of specific damping capacity.

$$\delta = \frac{1}{2} \frac{\Delta W}{E_{max}}. \quad (1.27)$$

For small damping $\zeta \ll 1$, the logarithmic decrement can also be approximated in terms of the ratio between damping constant and critical damping constant in equivalent viscous damped system.

$$\delta = 2\pi\zeta = 2\pi \frac{c}{c_c} = 2\pi \frac{c}{2m\omega_n} = \frac{\pi c}{m\omega_n}. \quad (1.28)$$

$$\zeta = \frac{1}{4\pi} \frac{\Delta W}{E_{max}}. \quad (1.29)$$

Different from Rao [2], Masuko [3] provided another way to express the relationship between logarithmic decrement and damping ratio. The damping ratio Ψ can be expressed as the ratio between the total energy introduced into the system and the loss energy,

$$\Psi = \frac{\Delta W}{\Delta W + E_{max}} = \frac{1}{1 + \frac{1}{2\pi\eta}}, \quad \eta = \frac{1}{2\pi} \frac{\Delta W}{E_{max}}. \quad (1.30)$$

When amplitude of vibration is a_n , the energy stored in the system is denoted as E_n , which is equal to $E_{max} + \Delta W$, and it is easily known that $E_{n+1} = E_n - \Delta W$. Assuming that the energy stored in the system is a quadratic equation of amplitude $C a_n^2$, the relationship between the damping ratio Ψ and the logarithmic decrement can be written as follows.

$$\delta = \ln\left(\frac{a_n}{a_{n+1}}\right) = \ln\left(\frac{E_n}{E_{n+1}}\right)^{1/2} = \frac{1}{2} \ln\left(\frac{E_n}{E_n - \Delta W}\right) = \frac{1}{2} \ln\left(\frac{1}{1 - \Psi}\right). \quad (1.31)$$

In case of $\Psi \ll 1$, Maclaurin expansion of equation 1.31 is given by

$$\delta = \frac{1}{2} \ln \left(\Psi + \frac{1}{2} \Psi^2 \right) \quad (1.32)$$

where the higher order of terms more than Ψ^3 are ignored. By substituting equation 1.30 into equation 1.32 we can obtain

$$\delta = \frac{1}{2} \ln (2\pi\eta + 1). \quad (1.33)$$

1.8 Slip damping mechanism

In the hysteresis damping category, friction in micro-slip is the most commonly observed damping mechanism. Even though the assemblage structure doesn't have any kinematic degree of freedom, the relative displacement between different components is able to cause energy loss due to frictional contact. Slip damping mainly takes place in joints and it is experimentally shown that this type of damping is much larger often by a factor of 10 than material damping [4]. According to the slipping degree at the interface, two dissipation mechanisms can be defined when a tangential force T is applied on the contact surface.

- Macro-slipping: there is total slipping at the interface, all the points have relative displacement to their corresponding points on the opposite surface.
- Partial slipping: one part of the interface slips and the other is still stuck together. According to the description level of the interface (from the level of the size of asperities to the level of macroscopic shape), two types of partial slipping can be distinguished.
 - Meso-slipping: there is no total slipping between the components, only one part of the contact zone is in slipping and the other is in sticking. If the applied force T gradually increases, the slipping zone will propagate until the whole zone is in slipping.
 - Micro-slipping: no macroscopic slipping is observed, the slipping only takes place at the level of asperities.

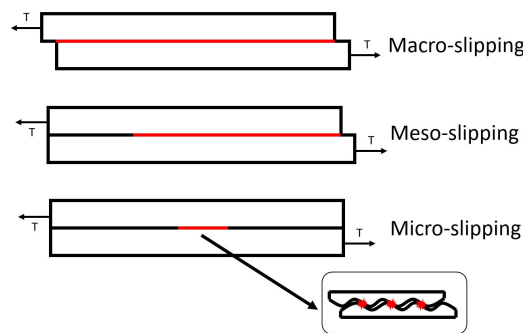


Figure 1.8: Slipping categories

In the majority of assembled structures, the components don't have mobility between them, thus the energy dissipation is mainly contributed by partial slipping. During the slipping movement, the kinematic energy is transformed into thermal energy and then dissipated in the surrounding environment. Under the action of stress and local heating, the contact surface will endure structural modification even deterioration. The surface damage caused by this alternative movement takes often the form of cracking and peeling. This surface wear and fatigue phenomenon is also called fretting.

The presence of slip damping is always related to bolted joint, which is a commonly used connecting method in assembled structures and has been the subject of damping studies for a long time. Typical values of bolt tension are between 50% and 90% of material yield, however, on the periphery of contacting surfaces interfacial stress will drop to zero and some slip will occur. This stress distribution makes it necessary to separate damping in bolted joints into two types:

- Type I is associated with the bolt itself such as the threads, washers, head and nut, whose damping value is determined from the structure in figure 1.9a.
- Type II is associated with the interface that the bolt is pressing together, whose surfaces may extend several bolt diameters away from the bolts themselves and or lie between bolt locations. The damping value of this part is evaluated by the configuration in figure 1.9b.

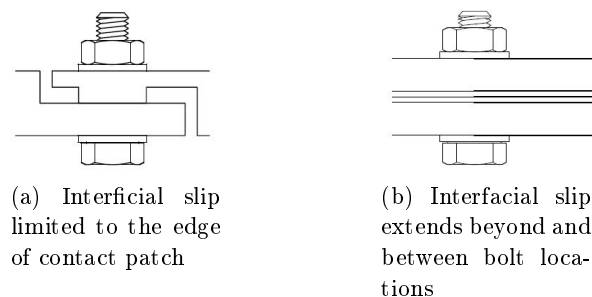


Figure 1.9: Experimental configurations to determine slip damping

Previous work of Goyder, Ind and Brown [5, 6, 7] has shown that damping of type I is small compared to damping of type II. The energy dissipation is thus mainly related to the slip on the periphery of contact surfaces. It is in such a way justifiable to ignore the energy dissipation in the joint itself and only focus on the slip damping related to the surrounding compressed surfaces.

1.9 Literature review

People start to pay attention to friction-induced damping when facing fatigue problems in engineering design. Many present-day assembled structures presenting complex geometries along with fluctuating excitation forces may at times be oscillated at or near a resonant frequency. These resonant conditions are not always harmful, but may, particularly in highly stressed components, produce fatigue failures. The insertion of viscoelastic material is an efficient way to increase fatigue endurance, but the disadvantage is that the damping capacity of the substances is dependent both on frequency and temperature. According to the investigation of Mead and Eaton [8], even though at low frequencies (around 200 Hz) the frictional damping of the metallic joint was 3 to 4 times less than for a viscoelastic joint, at higher frequencies (around 800 Hz) the damping capacity of the two joints were about the same. The damping capacity of the metallic joint can remain the same while the damping capacity of the viscoelastic joint may decrease with frequency. In this case, frictional damping caused by small relative interfacial movements at contact surfaces turns out to be an efficient alternative in damping design. The efficiency of friction damping has been proven in real applications, for example in civil engineering, the rocking timber structures can be connected by nailplates or slip friction connections. The study in [9] showed that under seismic excitation, the systems with nailplates incurred significant inelastic damages while the systems with friction devices exhibited superior performance in terms of strength degradation and absorbed seismic energy. Considering the advantages of friction damping, it has always been a subject under deep research in mechanical engineering. There are mainly two approaches: analytical modelization and numerical simulation. The study on friction-induced energy dissipation was firstly conducted on analytical models and then extended to numerical models, namely FEM simulations.

1.9.1 Analytical methods

Analytical modelization by simple academic model is the most direct way to study the mechanism of damping in assembled structures. The majority of the existing models are composed of beam or plate with frictional contact on the boundary. Here a brief literature review of the friction damping models that have been developed is given in chronological order.

The theoretical estimation of frictional damping was initiated by Goodman and Klumpp [10] in 1956, in which the optimization of frictional damping was proposed for the design of turbine blades. Four years later, a simplified exploratory analysis was carried out by Williams [11] on a cantilever beam with frictional flanges at the encastre, as illustrated in figure 1.10a. The use of analytical approach for damping modelization was thus initiated. The key point in this kind of study is to establish the relationship between energy dissipation and controlling parameters like geometry of the beam, clamping pressure as well as coefficient of friction. The existence of

optimal clamping pressure for a given amplitude was proposed in this study. The reaching of optimum damping can be considered as the moment when the energy dissipated W , expressed as a fraction of the total energy $(U + W)$, is a maximum, where U is the strain energy at the full tip amplitude. The hysteresis loop was even traced with the proposed model, as illustrated in figure 1.10b.

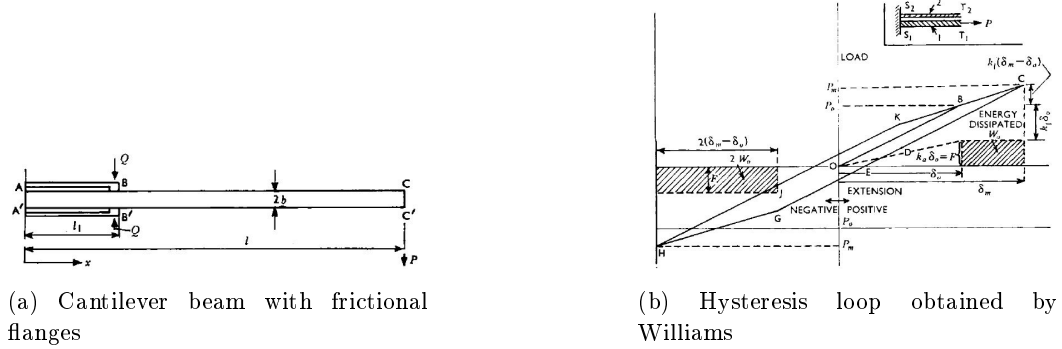


Figure 1.10: Analytical model used by Williams

In 1966, Earles [12] used an analytical overlapping plate model to study the relationship between the fatigue life of lap joint and the force transference arrangement, as illustrated in figure 1.11a. The study on the influence of uniform and non-uniform clamping pressure shows that for each clamping pressure distribution used, the maximum of damping capacity ratio occurs when the clamping force is such that the total applied force is transferred only by the friction throughout the joint. This adjustment of clamping pressure can result in a better fatigue life and a specific damping capacity substantially better than that obtained from material damping and comparable with that of viscoelastic layers. Different from Williams, the dissipated energy in this study was expressed in terms of maximum possible force transmitted by friction F .

$$\Delta W = \frac{93LF^2}{70Ebd} + \frac{9RFL}{4Ebd}, \quad (1.34)$$

where E the modulus of elasticity, L the semi-length of joint overlap, R the maximum shear force carried by the rivet, b the joint plate breadth and d the joint plate thickness. The hysteresis loop obtained in figure 1.11b show that the change in pressure distribution can modify the form of hysteresis loop.

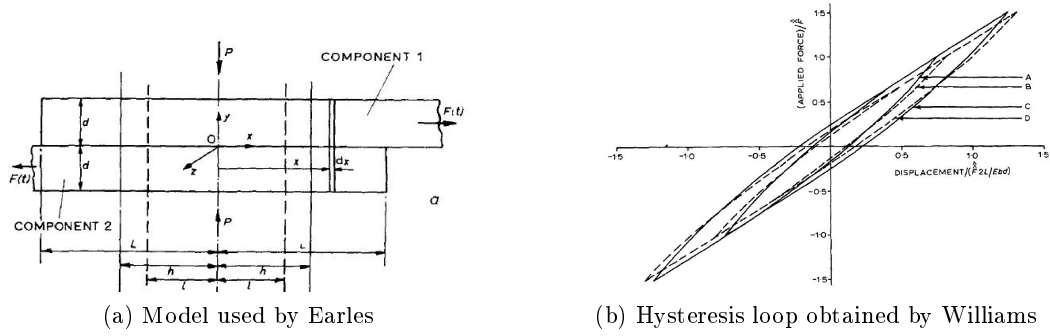


Figure 1.11: Analytical model used by Earles

The theoretical and experimental study on frictional damping modelization was then carried out on jointed cantilever beam in 1973 by Masuko *et al.* [3]. The relative displacement ΔW between the upper and lower plate can be expressed in terms of the spatial derivative of bending deflection $y(x, t)$.

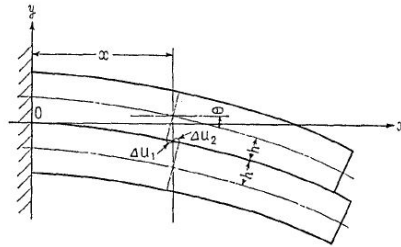


Figure 1.12: Jointed cantilever beam used by Masuko

$$\Delta U = \Delta U_1 + \Delta U_2 = 2h \tan \left(\frac{\partial y(x, t)}{\partial x} \right) \approx 2h \frac{\partial y(x, t)}{\partial x}. \quad (1.35)$$

According to the analysis of Masuko, there exists an optimum value of the interface pressure for a given coefficient of friction and full tip amplitude.

An experimental verification was then carried out on the same analytical model by Nishiwaki [13, 14]. The relationships between the frequency and the damping capacity were studied by the use of an improved band-width method with two kinds of jointed cantilever beams which are connected with a single bolt and several bolts respectively.

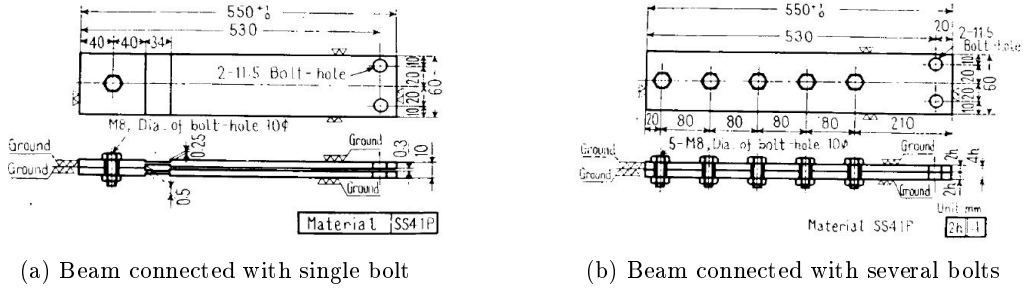


Figure 1.13: Experimental verification of jointed beam

It is shown in the experiment that for structures like jointed beam, the dynamic slip increases with an increase of frequency and amplitude of vibration, and decreases with an increase of the preload of connecting bolt. The static stiffness is a function of clamping pressure, it is constant above a certain value of the connecting preload. When the number of bolts is large, the static stiffness of the jointed beam is nearly equal to that of the equivalent solid beam when its preload is big enough. However if the number of connecting bolts is small, the theoretical static stiffness of the equivalent solid beam cannot be used to calculate the energy stored in a vibrating system.

The jointed beam stayed as a commonly used model in 1990s. Hansen and Spies [15] applied Timoshenko beam theory along with an adhesive layer of negligible thickness to study interface micro-slip damping. However it was found from the result obtained that the frictional damping resulted in a frequency-proportional damping pattern in the spectrum, which is different the common understanding that friction damping is proportional to modal amplitude. During this period, more work has been done for the refinement of the jointed beam model. Early investigators, e.g. Masuko *et al.* and Nishiwaki *et al.* all have assumed uniform intensity of pressure distribution on the contact surface without taking into account the spacing between bolts, however Gould [16] and Ziada [17] have shown that the pressure distribution at the interfaces of bolted joint is parabolic in nature and there exists an influence zone in the form of a circle with 3.5 times the diameter of the connecting bolt. In 1999 the study of Nanda [18] has made up the defects in uniform pressure due to bolt spacing in the previous studies and extended the jointed beam model to layered structures. Based on the relationship between clamping pressure and tightening torque on the bolt given by Shigley [19],

$$p = \frac{0.671P}{3\pi R_B^2}, \quad P = \frac{T}{0.2D_B} \Rightarrow p = \frac{0.17799T}{R_B^2}, \quad (1.36)$$

where R_B is bolt's radius, D_B is bolt's diameter, T is the torque applied on the bolt, the uniform pressure can be obtained by a spacing of 2 times the diameter of connecting bolts.

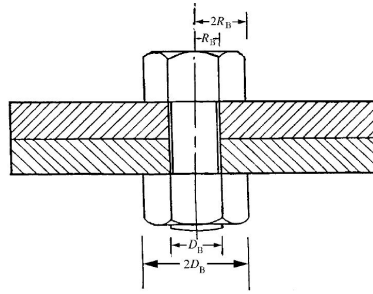


Figure 1.14: Jointed cantilever beam used by Masuko

It was found by Nanda that the natural frequency of first mode vibration of any layered and jointed structure doesn't vary appreciably with an increase in the tightening torque on the connecting bolts. This observation means that the clamping pressure cannot modify significantly the mode shape of the vibration. This experimental verification confirms the reasonability of the non-changing mode shape hypothesis that will be adopted in the following chapters.

In the 21st century, the jointed beam has always been a standard benchmark for friction-induced damping studies, but more refinements have been brought into the model. In 2007, Damisa [20] introduced linear pressure variation in the jointed beam model and applied Fourier Sine Transform to for a static analysis of slip damping. It was discovered that the characteristics of the pressure distribution can influence or modify the the amount of energy dissipated. This finding signifies that the material cannot be changed for the purpose of minimizing fretting etc. without consideration of the change in coefficient of friction. As energy dissipation is sensitive to pressure distribution, the influence of bolt's diameter was given in [21]. One year later, Damisa [22] attempted to extend the static calculation of energy dissipation in jointed beam to account for cases of realistic dynamic loading with non-uniform interfacial pressure profile. It was found that the load frequency could have a significant role to play in defining the optimal pressure for slip damping. The jointed beam model was extended to multi-layered and welded structures in [23, 24] by Singh. Both static and dynamic analysis were conducted on the model and it was inferred that damping capacity of layered and welded structures could be substantially enhanced by fabricating the structures with multiple interfaces. In addition, the decrease in damping ratio as the modal amplitude increases was also revealed both by analytical analysis and experimental verification.

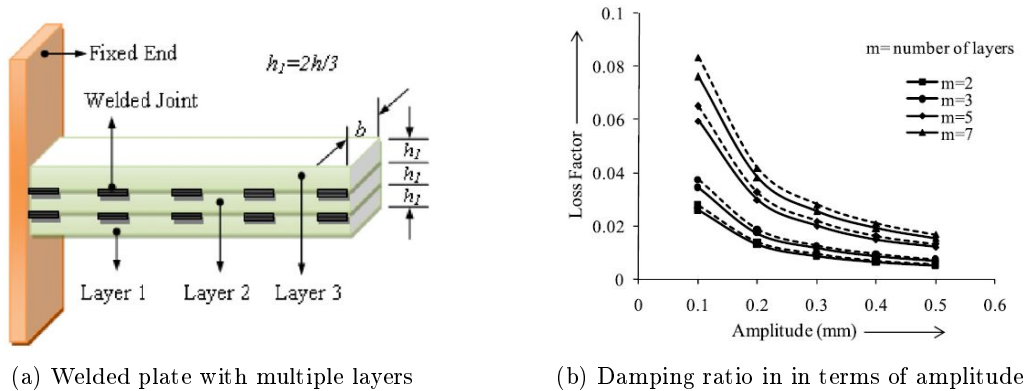


Figure 1.15: Study on multi-layered joined beam

The cantilever beam developed by Williams as well as the joined beam used by Masuko, Nanda and other researchers is a simple but representative model to study damping induced by contact friction. At the same time, other simplified friction models of assembled structures have also been developed. Jézéquel [25] proposed in 1983 a general formulation for boundary slip damping induced by second-order bending strain based on von Kármán plate equation. The modelization of friction damping by quasi-static calculation was firstly introduced by which the hardening/softening effect as well as the damping ratio can be obtained. Due to the constraint on numerical calculation capacity of the time, the proposed method was only realized on an analytical circular plate with frictional boundary, as illustrated in figure 1.16a. The characteristic of the second-order damping was firstly revealed by $\eta - q$ curve in figure 1.16b which establishes the evolution of damping ratio in terms of modal amplitude. It is shown that the damping ratio tends to a constant under big modal amplitude, which presents a remarkable difference from the damping in jointed beam illustrated in figure 1.15b.

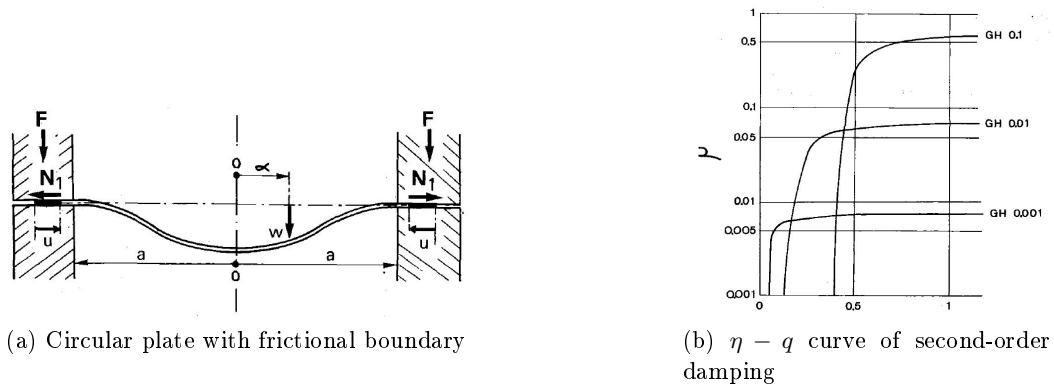


Figure 1.16: Damping study on von Kármán plate

An extended study based on the conclusion of Jézéquel was conducted three years later in 1986 by Dowell [26]. The model used in the study was a pinned-pinned beam with a sliding restraint with respect to axial motion at one end.



Figure 1.17: Pinned-pinned beam with sliding constraint

The stress-strain and strain displacement relations of geometrically non-linear beam theory allows one to write

$$N_x = Ehb \left[\frac{\partial u}{\partial x} + \frac{1}{2} \left(\frac{\partial w}{\partial x} \right)^2 \right] \quad (1.37)$$

Rearranging equation 1.37 and integrating over the length l of the beam,

$$u(x=l) + \frac{1}{2} \int_0^l \left(\frac{\partial w}{\partial x} \right)^2 dx = \frac{N_x l}{Ehb}. \quad (1.38)$$

When slipping occurs, the Coulomb dry friction gives

$$N_x = -\mu P \text{sign}[\dot{u}(x=l)]. \quad (1.39)$$

Note that N_x is constant with respect to time except when $\dot{u}(x=l) = 0$, the time derivative of equation 1.38 is expressed by

$$\dot{u}(x=l) + \int_0^l \frac{\partial w}{\partial x} \frac{\partial \dot{w}}{\partial x} dx = 0. \quad (1.40)$$

The sign of the two sides of equation 1.40 should be the same,

$$\text{sign}[\dot{u}(x=l)] = -\text{sign} \left[\int_0^l \frac{\partial w}{\partial x} \frac{\partial \dot{w}}{\partial x} dx \right]. \quad (1.41)$$

If the displacement field is expressed by a single spatial mode $w = q\phi(x)$, the equation 1.41 can also be written as

$$\text{sign}[\dot{u}(x=l)] = -\text{sign} \left(q \cdot \dot{q} \int_0^l \frac{\partial \phi(x)}{\partial x} \frac{\partial \phi(x)}{\partial x} dx \right) = -\text{sign}(q \cdot \dot{q}), \quad (1.42)$$

Substitute equation 1.42 into equation 1.39, the sign of internal force can be determined as

$$\text{sign}(N_x) = \text{sign}(q \cdot \dot{q}). \quad (1.43)$$

Whiteman [27] studied in 1996 the displacement-dependency of dry friction damping on a single-degree-of-freedom flexible beam with a displacement dependent dry friction damper, in which the normal force across the friction interface

increases linearly with the transverse displacement, as illustrated in figure 1.18a. The approximate solution used first order harmonic balance method and the beam flexural displacement was represented by a single spatial beam mode,

$$w(x, t) = z(t)\phi(x), \quad (1.44)$$

where $z(t)$ is the modal amplitude and $\phi(x)$ is the shape function. The Galerkin procedure was then performed and the equilibrium was expressed in the modal space. According to the curve of equivalent damping ratio versus displacement at midspan which can be regarded as a scaling factor of modal amplitude, the equivalent damping is inversely proportional to displacement amplitude, for higher values of amplitude, the behavior looks more like that of “viscous” damping. Further insight into the qualitative nature of the dynamic response of this model is gained by looking at the equivalent damping ratio at resonance. It was shown in the study the existence of an optimal ramp angle γ to obtain the maximum damping ratio, this result suggests that it is possible to enhance the vibration suppression properties by dry friction through the judicious selection of the contact pressure.

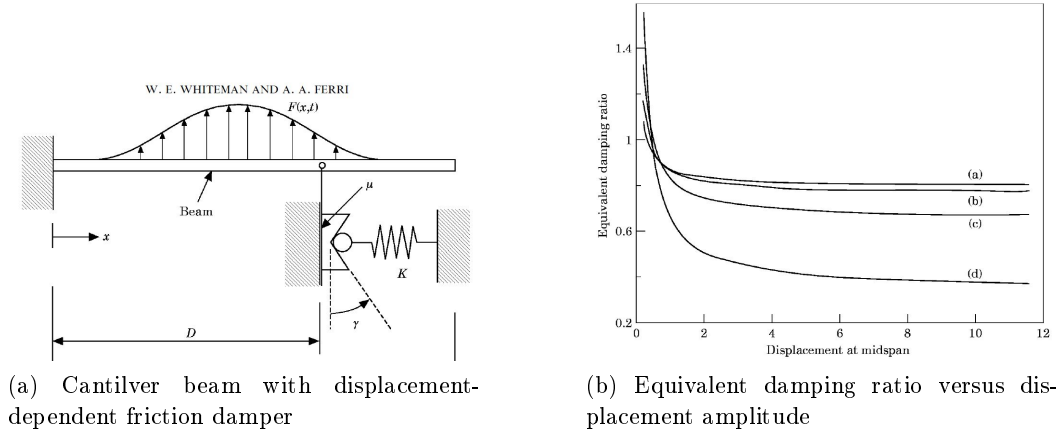


Figure 1.18: Damping study on von Kármán plate

There are also more recent models that have been developed on friction damping since 2010. The sectioned beam used by Peyret [28, 29] is one example. The structure is composed of three successive beams, with lengths $l/4$, $l/2$ and $l/4$. The beams are linked by two planar joints with contact and friction. The three parts are linked by an axial load N . This configuration was derived from a monolithic beam with a transverse load applied to the middle. At the positions where the beam is cut, the bending moment is equal to zero, therefore, in those sections, there are only shear stresses. In this way the normal force is only brought by the axial force N and a uniform clamping pressure can be guaranteed. The shear stress profile on the cut surface is parabolic, with the increase in transverse load, the shear stress will be saturated to the value $\mu\sigma_n$ where σ_n is the normal stress on the contact surface. The shear stress field is expressed in equation 1.38 and illustrated in figure 1.19a.

$$\tau(y) = -\frac{T}{2I_{Gz}}y^2 + \frac{3T}{2S}. \quad (1.45)$$

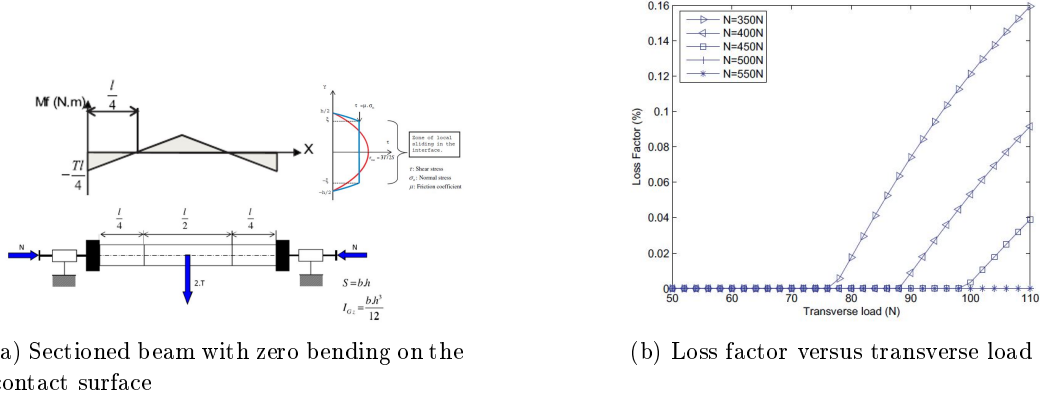


Figure 1.19: Damping study on sectioned beam and its result

The parabolic stress field enables the appearance of partial sliding. This model describes the phenomenon of sticking-slipping transition with a new stress distribution: the micro-slip originates at the center of the contact region. According to the relationship between loss factor and transverse load, the clamping pressure was shown to have a significant influence on damping property. Under bigger pressure, a bigger load is needed to activate slipping and consequently the energy dissipation. It can also be expressed in terms of displacement and indicates that friction-induced damping depends on the amplitude of displacement.

The beam model is a commonly employed element in friction-induced damping studies, especially for analytical analysis. Whether it is used for the modelization of lap joint or layered structures, all the results have pointed to the conclusion that friction damping is proportional to displacement amplitude. This conclusion will be reinforced by the proposed academic models in the second chapter. Even though analytical analysis is shown to be more direct in revealing damping properties, it is restricted to models with simple geometry. The next section will present the state of art in numerical modelization of frictional damping.

1.9.2 Numerical methods

Along with the development of finite element method, contact modelization has been a critical issue in the analysis of complex structures held together by mechanical joints. The current section will present 2 contact modeling methods presented in [30, 31, 32, 33] for joint modeling with the finite element method as well as the relevant applications conducted by other researchers.

1.9.2.1 Node-to-node contact

In this approach, the contact between linear substructures with small deformations is considered. Under the assumption of small relative tangential movement in the contact area, node-to-node elements can be applied to model contact and friction in a nodal basis. If the discretization of the substructure interfaces is the same, as illustrated in figure 1.20, the equations can be formulated directly for each nodal pair.

$$\begin{bmatrix} \mathbf{M}_1 & \mathbf{0} \\ \mathbf{0} & \mathbf{M}_2 \end{bmatrix} \begin{pmatrix} \ddot{\mathbf{x}}_1 \\ \ddot{\mathbf{x}}_2 \end{pmatrix} + \begin{bmatrix} \mathbf{K}_1 & \mathbf{0} \\ \mathbf{0} & \mathbf{K}_2 \end{bmatrix} \begin{pmatrix} \mathbf{x}_1 \\ \mathbf{x}_2 \end{pmatrix} + \begin{bmatrix} \mathbf{B}_T^1 \\ \mathbf{B}_T^2 \end{bmatrix} \mathbf{f}_T + \begin{bmatrix} \mathbf{B}_N^1 \\ \mathbf{B}_N^2 \end{bmatrix} \mathbf{f}_N = \mathbf{f}_{\text{ext}} \quad (1.46)$$

The substructures are coupled by the tangential nodal forces \mathbf{f}_T and normal nodal forces \mathbf{f}_N . The matrices $\mathbf{B}_T^{(i)}$ and $\mathbf{B}_N^{(i)}$ are Boolean matrices that capture coincide pairs of physical DOFs. The tangential force is a function of relative displacement $\mathbf{x}_{\text{rel}} = \mathbf{B}_T^1 \mathbf{x}_1 - \mathbf{B}_T^2 \mathbf{x}_2$ and tangential contact stiffness \mathbf{k}_T .

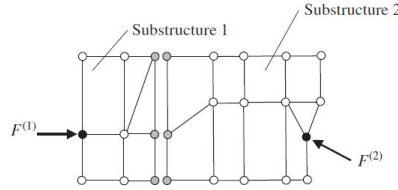


Figure 1.20: Node-to-node contact

The system expressed in equation 1.46 can be solved by the Harmonic Balance Method. The nonlinear friction force f_T (one of the discrete component of \mathbf{f}_T) can be decomposed into an in-phase part which is proportional to displacement and an out-of-phase part which is proportional to velocity.

$$F_T(x_{rel}) \approx k_{HBM} x_{rel} + d_{HBM} \dot{x}_{rel}. \quad (1.47)$$

If the first harmonics are retained, the friction force can be expressed by

$$F_T(x_{rel}) = a_0 + a_c \cos(\omega t) + a_s \sin(\omega t). \quad (1.48)$$

where a_c and a_s are the coefficients of Fourier series. With the assumption of a harmonic relative displacement $x_{rel} = \hat{x} \cos(\omega t)$ and compare the equation 1.47 and 1.48, the harmonic equivalent stiffness and damping coefficients are written as

$$k_{HBM} = \frac{\omega}{\pi \hat{x}} \int_0^{2\pi/\omega} F_T \cos(\omega t) dt, \quad d_{HBM} = -\frac{\omega}{\pi \hat{x}} \int_0^{2\pi/\omega} F_T \sin(\omega t) dt \quad (1.49)$$

Given the linearized frictional force, the response of the system can be obtained by an iterative solution procedure. The response of a system to a harmonic excitation $\mathbf{f}_{\text{ext}} = \hat{\mathbf{f}}e^{i\omega t}$ is assumed to be harmonic with $\mathbf{x} = \hat{\mathbf{x}}e^{i\omega t}$. Thus the equation of motion can be transformed into an algebraic equation

$$[\mathbf{K} + \mathbf{K}_{\text{BHM}}(\hat{\mathbf{x}}) + i\omega(\mathbf{D} + \mathbf{D}_{\text{HBM}}(\hat{\mathbf{x}})) - \omega^2\mathbf{M}]\hat{\mathbf{x}} = \hat{\mathbf{f}}. \quad (1.50)$$

The system of equations can be converted to

$$\hat{\mathbf{x}} = \mathbf{H}_{\text{HBM}}^{-1}\hat{\mathbf{f}}, \quad (1.51)$$

where \mathbf{H}_{HBM} is the dynamic stiffness matrix with

$$\mathbf{H}_{\text{HBM}} = \mathbf{K} + \mathbf{K}_{\text{BHM}}(\hat{\mathbf{x}}) + i\omega(\mathbf{D} + \mathbf{D}_{\text{HBM}}(\hat{\mathbf{x}})) - \omega^2\mathbf{M}. \quad (1.52)$$

This problem can be solved iteratively by Newton-Raphson Method with an initial value $\hat{\mathbf{x}}_0$. The modeling by node-to-node elements offers the possibility to implement various different types of friction models. In addition, nonlinear effects like sticking-slipping and separation of each node pair can be modeled. However, for large number of contact pairs the numerical calculation for each element will be very heavy and the efficiency will decrease.

1.9.2.2 Thin layer elements

The key idea in the application of thin layer elements is to model the joint interface between two substructures by a continuous element with very small but finite thickness. The existing thin layer elements are hexahedral or pentahedral elements formulated with the isoparametric concept and are available in commercial finite element programs. The joint parameters used to model with thin elements are firstly acquired from a generic joint experiment and then integrated into the finite element modelization. This method allows engineers to estimate the eigenfrequencies and modal damping factors of an assembly before the physical prototype is available. Using the model of constant hysteresis, the damping can be incorporated into the stiffness matrix in frequency domain by augmenting it with the complex-valued product of experimentally determined dissipation multipliers α_i and β_i .

$$\mathbf{K}^* = \mathbf{K} + i\omega\mathbf{D} = \mathbf{K} + i\omega \sum_{j=1}^n \alpha_i \mathbf{K}_j^{\text{Material}} + i\omega \sum_{j=1}^n \beta_i \mathbf{K}_j^{\text{Joints}}. \quad (1.53)$$

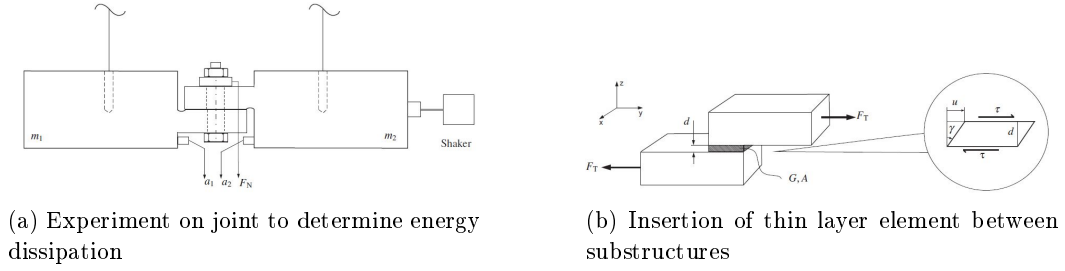


Figure 1.21: Application of thin layer element

The shear stiffness of the joint can be determined from the tangential force in the experiment and thin element's geometry.

$$\tau = G\gamma \approx G\frac{u}{d}, \quad \tau = \frac{F_T}{A} \quad (1.54)$$

where G is the shear modulus and γ is the shear angle. The shear stress can also be expressed in terms of tangential load F_T and contact area A of the generic joint. Equating the two expressions of equation 1.54, the shear modulus can be expressed as

$$G = \frac{dF_t}{uA}. \quad (1.55)$$

In the orthotropic constitutive matrix C_{ij} of $\sigma_{ij} = C_{ij}\varepsilon_{ij}$, only the terms C_{55} and C_{66} are non-zero and equal to G . The coefficients C_{ij} obtained give a generalized characterization of joint behavior and can then be used to generate the element stiffness matrix $\mathbf{K}_j^{\text{Joints}}$.

The advantage of thin layer elements is the ability to predict the damping and eigenfrequencies of a structure using experimentally determined joint parameters and this method can be applied to structures with large number of DOFs. The drawback is that it is a linear method which can only simulate structures with minimal dissipation in joints and can be used only in frequency domain.

1.9.2.3 Numerical studies on real structures

Numerical modelization by finite element method allows simulation on full-sized structures containing contact interface. One of the most studied subjects is bolted joint, to which many attempts have been made to obtain its mechanical properties such as contact stiffness and friction damping [34]. In order to accurately predict the the physical behavior of the structure with bolted joints, a detailed three-dimensional bolt model is desirable. But the limitations on model size sometimes make modeling of solid bolts impractical. Therefore, many analysts choose other methods to model bolts [35, 36, 37]. Kim *et al.* [38] studied in 2007 four kinds of finite element models: solid bolt model, coupled bolt model, spider bolt model and no-bolt model as illustrated below. The difference between the coupled

bolt model and the spider bolt model is that both the head and the nut of the bolt are modeled by beam elements in the spider model. In this study, the 3D 8-node surface-to-surface contact element CONTACT174 of ANSYSTM was used. It was found that the solid bolt model which models the full-size geometry of bolt could most accurately predict the physical behavior of the structure compared to static experiment. The coupled bolt model and the spider bolt model were shown to be more time-saving in view of effectiveness and usefulness. The no-bolt model was studied by Knight [39] with the ABAQUSTM C3D8I 8-node solid element. The washer-bearing-surface size was shown to be able to affect the the response significantly.

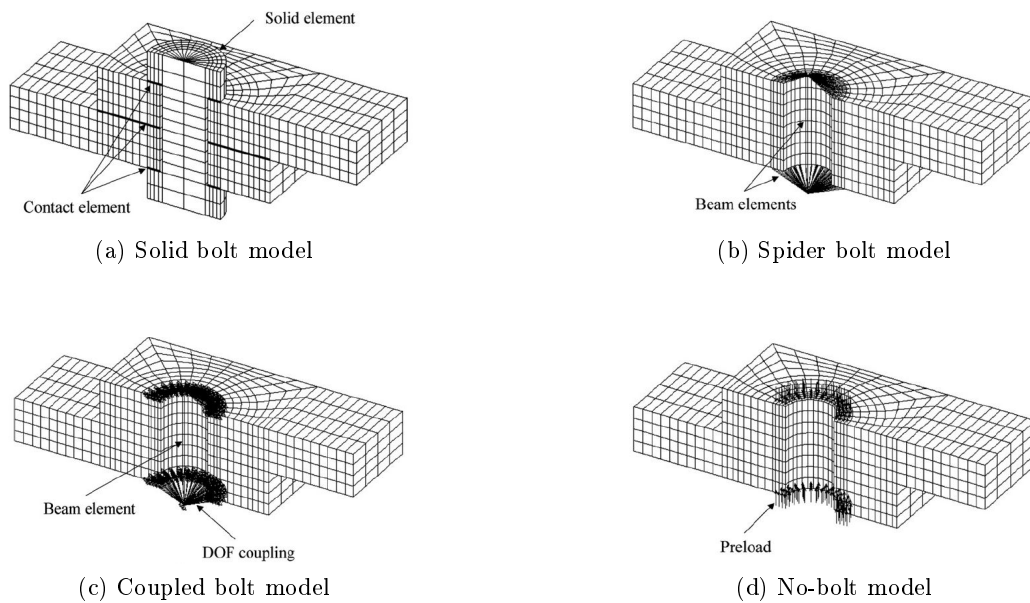


Figure 1.22: Four bolt modelization methods

The axial stiffness of bolted flange joints was studied by Luan [40] in 2012. The axial stiffness could be obtained by full-sized finite element modelization, and it was found to be different in tension and compression. Based on this nonlinear property of bolted joint, a simplified model with bi-linear springs was proposed and validated for pipe structures with bolted flange joints. The torsional property of bolted joint was analyzed by FEM calculation along with analytical modelization by Shamoto *et al.* two years later [41] in 2014. The energy dissipation in terms of displacement was shown to be a quadratic function and the damping coefficient presented the characteristic that is similar to second-order damping illustrated in figure 1.16b.

Besides the direct or indirect modelization of bolted joint, there has also been studies by FEM purely on frictional surface, such as the work of Chen and Deng [42] on the micro-slip phenomenon in the press-fit joint and the lap-shear joint. The two

joints were both modeled by two-dimensional and three-dimensional elements. The comparison between the 2D (plane stress and plane strain) and 3D modelization showed that there wasn't significant difference between the two methods in the case of press-fit joint problem. But as the width of the plate increases, the plane strain prediction is a better approximation to the 3D solution. This conclusion will justify the use of 2D plane strain elements to study the damping in sandwich plate in chapter 2.

1.9.3 Air damping

In addition to the frictional damping induced by micro-slip or macro-slip in the assembled structures, there is another dominant damping mechanism associated with "gas-pumping". Air damping is considered to be dependent on frequency and gas pressure. The energy dissipation is contributed by the gas motion tangential to the contact plane, resulting from the the relative flexural movement between the adjacent surfaces. The significant contribution of gas-pumping to the total damping in riveted structures was discovered by Ungar [34] in 1964. One year later Scacullo and Stephens [43] conducted the study of air damping in circular and rectangular plates, the results showed that the magnitude of the air damping might greatly exceed the structural damping.

The the majority of the existed studies on air damping are based on the following three assumptions [44]:

- The separation distance between the contact bodies is very small compared with the linear dimensions of the plate.
- The gas flow is assumed to be laminar and primarily viscous. This assumption implies low Reynolds numbers and parabolic velocity distributions across the gas film.
- The relationship between pressure and density at any point in the gas film is assumed described by a polytropic process with exponent n , $p\rho^{-n} = \text{const}$. The film is nearly isothermal if the relative velocities are relatively low and $n \approx 1$.

Based on the expression of fluid flow between two moving plates given by Landau [45], Maidanik [46] developed in 1967 an analytical model for semi-phenomenological study of energy dissipation associated with gas-pumping between a beam and a plate. It illustrates well the basic characteristics of damping induced by gas-pumping.

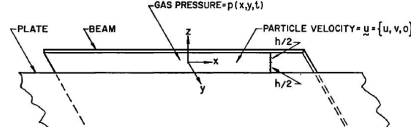


Figure 1.23: Node-to-node contact

The Mach numbers associated with the motion of the gas are assumed small as compared to unity, then the conservation of momentum can be linearized. The power dissipated in the region of overlap between the two surfaces may be approximated by the expression

$$P_{\Delta E} \approx \frac{hc_0^2 A_b}{2np_0\omega} \langle \|\nabla p\|^2 \rangle H(\theta) \quad (1.56)$$

where

$$\theta = \frac{h}{\delta}, \quad \delta = \left(\frac{2\nu}{\omega} \right)^{\frac{1}{2}} \quad (1.57)$$

and

$$H(\theta) = (\sinh \theta - \sin \theta) [\theta (\cosh \theta) + \cos \theta]^{-1}. \quad (1.58)$$

δ represents the the boundary layer thickness, ν the kinematic viscosity of the gas, ω the angular velocity of the excitation, h the separation distance, p_0 the ambient pressure of the gas, c_0 the sound speed and A_b the area under the beam. The loss factor associated with the the power dissipated by the gas can thus be obtained as

$$\eta \approx \frac{P_{\Delta E}}{A_p m_p \langle \|V_{p0}\|^2 \rangle} = \frac{A_b h c_0^2}{2A_p m_p n p_0 \omega} \frac{\langle \|\nabla p\|^2 \rangle}{\langle \|V_{p0}\|^2 \rangle}, \quad (1.59)$$

where A_p is the area of the plate ($A_p \gg A_b$), m_p represents the plate mass per unit area, and $\langle \|V_{p0}\|^2 \rangle$ the mean square velocity field on the plate. From the expression above, the loss factor due to gas-pumping is related to the geometry and mass of the contact bodies, the frequency, the pressure of ambient pressure as well as the pressure gradient between the contact surfaces.

For more recent studies who focus mainly on damping mechanism in MEMS (Microelectromechanical Systems), e.g. micro-sensors. Bao [47] developed in 2002 an energy transfer model with the Boltzmann statistics on molecules velocity. The energy loss due to the surrounding gas in one oscillation cycle is given by

$$\Delta E = 4abmn \sqrt{\frac{2kT}{\pi m}} A_0^2 \omega \pi \quad (1.60)$$

where m represents the mass of the gas molecules, n the density of the gas molecules, ab the area of the plate, k the Boltzmann constant, A_0 the amplitude

of vibration and ω the angular velocity. The energy dissipation is shown to be linearly proportional both to the area of the squeezed air film and excitation frequency.

In 2010 Biçak [48] integrated the mode shape into the plate displacement field and used Green's function to solve Reynolds equation. The use of Green function can also be found in [49]. The air-pumping force can be decomposed as an in-phase and an out-of-phase component, the out-of-phase component F_d is directly related to the damping ratio $\zeta = F_d/2\omega_n$, as explained by equation 1.49. The numerical study of air damping by FEM was conducted by De Pasquale [50] on perforated gold and silicon MEMS plates, but the results showed that the damping factors obtained were not satisfactory compared to measured results.

1.10 Conclusion

The present chapter firstly introduces the industrial context in which the subject of the current thesis is proposed. Friction-induced damping is shown to play a more dominant role compared to material damping in determining the vibration response of the assembled structures. The damping of a structure can be quantified by the logarithmic decrement δ in a free vibration or by the loss factor η between the energy dissipation in one oscillation cycle and the maximum elastic energy stocked in the system. The mathematical relationship between the two factors are derived in details. In the literature review, the precedent studies on frictional damping and air damping are summarized in chronological order. The studies on frictional damping can be divided into two parts: analytical modelization and numerical simulation. All the analytical models point to the fact that frictional damping is generally a function of modal amplitude which can also be influenced by parameters like clamping pressure and coefficient of friction. This conclusion will serve as the fundamental idea for the phenomenological study in chapter 2. Two numerical methods for contact problems are then introduced, the general method for nonlinear force linearization by HBM is presented. The current numerical studies on frictional damping focus mainly on energy dissipation in bolted joints, several modelization methods indicate that a full-sized modelization of joint can guarantee a better accuracy, but it is time-costing, so other simplified model by beam elements may replace the solid bolt model while keeping a good representation of the dynamic properties. The last section is dedicated to damping by gas-pumping. Different from the frictional damping, the energy dissipation in gas-pumping is related to oscillation frequency as well as ambient pressure. It is an energy dissipation mechanism that can also be dominant in the overall damping composition of assembled structures. The next section will only focus on friction-induced damping and give a preliminary phenomenological study of friction damping in terms of modal amplitude.

Phenomenological study of friction damping

Contents

1.1	Undamped and damped vibration	2
1.2	Damping sources	3
1.3	Damping categories	4
1.4	Energy dissipation in viscoelastic material	5
1.5	Energy dissipation in hysteretic damping	6
1.6	Logarithmic decrement	8
1.7	Relation to logarithmic decrement	9
1.8	Slip damping mechanism	11
1.9	Literature review	13
1.9.1	Analytical methods	13
1.9.2	Numerical methods	21
1.9.3	Air damping	26
1.10	Conclusion	28

2.1 Introduction

Micro-slip is considered as the most important damping mechanism in assembled structures. In order to clarify the origin of energy dissipation as well as the influence of different controlling parameters like clamping pressure, coefficient of friction and geometry characteristics, three simplified academic models are proposed in the first place to give a preliminary phenomenological insight into dry friction damping. These three models are respectively:

- First-order interface damping in sandwich beam
- First-order boundary damping in rotational joint
- Second-order boundary damping in von Kármán plate

Due to the geometrical simplicity of the three models, analytical approach is thus possible in damping modelization. Mathematical expressions of damping ratio are derived for each model, which enable a fast and comprehensive study of the influencing parameters. Several numerical studies are then conducted on the sandwich beam model in order to study the influence of parameters that cannot be analytically analyzed, such as welding points number, thickness ratio and contact geometry defaults.

2.2 First-order interface damping in sandwich beam

2.2.1 Analytical modelization

2.2.1.1 Model for perfect surface

Sandwich beam is a commonly used structure in damping studies. The model used in this section is illustrated in figure 2.1 on page 30. Two identical beams are superimposed one on another with a frictional contact interface between them, on which the Coulomb's law is used as friction property. A uniform clamping pressure is applied to both upper and lower surface of the assembled structure.

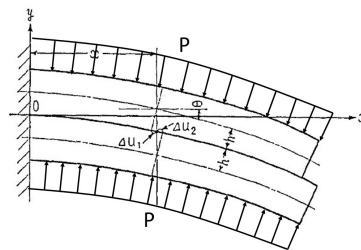


Figure 2.1: Sketch of jointed sandwich beam

A force equilibrium analysis is conducted in the first place to obtain a mathematical description of the sandwich beam, as illustrated in figure 2.2 on page 31. The derivation procedure presented here is inspired by the work of Nanda [18].

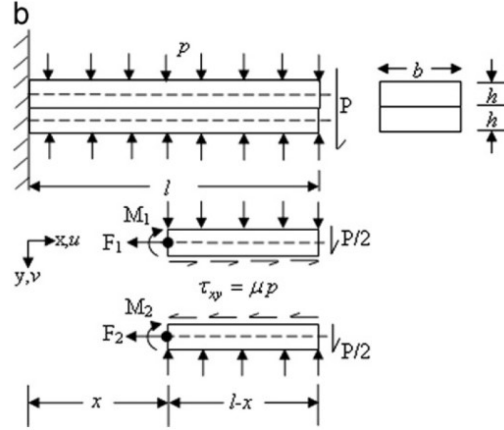


Figure 2.2: Free body diagram of the sandwich beam

The moment equilibrium with respect to the point M_1 which is denoted by distance x from the encastre is expressed by equation 2.1. The clamping pressure doesn't appear in the expression because the effect of pressure on the upper and lower surface are counteracted. It should be noted that the equilibrium established here describes the slipping stage since the tangential stress is already saturated and is uniform along all the contact interface, here P designates the exterior loading.

$$M_1 = M_2 = \frac{P}{2}(l-x) - \mu pb \frac{h}{2}(l-x). \quad (2.1)$$

The relationship between bending moment and deflection in Euler-Bernoulli beam is written as

$$M = -EI \frac{d^2 w}{dx^2} \quad \text{where } E: \text{Young's modulus, } I = \frac{1}{12}bh^3. \quad (2.2)$$

If we combine the equation 2.1 with equation 2.2, we can obtain

$$\frac{d^2 w}{dx^2} = \frac{6}{Ebh^3}(P - \mu pbh)(l-x) \quad (2.3)$$

$$\frac{dw}{dx} = \frac{6}{Ebh^3}(P - \mu pbh) \left(lx - \frac{1}{2}x^2 \right) + C_1 \quad (2.4)$$

$$w = \frac{3}{Ebh^3}(P - \mu pbh) \left(lx^2 - \frac{x^3}{3} \right) + C_1 x + C_2. \quad (2.5)$$

The two unknown coefficients can be determined by the boundary condition at the encastre endpoint $w|_{x=0} = 0$ and $\frac{dw}{dx}|_{x=0} = 0$, which can give the values of $C_1 = 0$ and $C_2 = 0$. Thus the expression for the beam's deflection can be obtained as

$$w(x) = \frac{(P - \mu pbh)l^3}{Ebh^3} \left[3 \left(\frac{x}{l} \right)^2 - \left(\frac{x}{l} \right)^3 \right]. \quad (2.6)$$

The deflection obtained here can be thought of as a result of combined influence from endpoint loading and interface friction shearing. In order to simplify the writing of equations, we introduce two constants Q and R .

$$Q = \mu pbh, \quad R = \frac{Ebh^3}{l^3}. \quad (2.7)$$

As mentioned before the derivation of deflection's expression, the equation 2.6 is valid only for slipping. Before the occurrence of slipping, the contact interface goes through a gradually increasing tangential stress. We adopt the hypothesis that the transition from sticking to slipping is brutal and that all the points on the interface slip or stick synchronously.

If we take into account the longitudinal variation due to axial force, the horizontal displacement of a point which is positioned at distance x from the encastre is given by equations 2.8 and 2.9. u_1 designates the in-plane displacement in the upper beam and u_2 refers to the in-plane displacement in the lower beam.

$$u_1 = \frac{1}{E} \int_0^x \sigma_{x_1} dx - \frac{h}{2} \frac{dw_1}{dx} \quad (2.8)$$

$$u_2 = \frac{1}{E} \int_0^x \sigma_{x_2} dx + \frac{h}{2} \frac{dw_2}{dx}. \quad (2.9)$$

According to the force equilibrium in the free body diagram in figure 2.2, average normal stresses in the two beams can be expressed as

$$\sigma_{x_1} = \frac{\mu pb(l-x)}{bh} = \frac{\mu p(l-x)}{h} \quad (2.10)$$

$$\sigma_{x_2} = -\frac{\mu pb(l-x)}{bh} = -\frac{\mu p(l-x)}{h}. \quad (2.11)$$

If we put the relation 2.10 and 2.11 into 2.8 and 2.9 and use the deflection expression given by 2.6, the relative displacement at the point x is given by

$$\Delta u = u_2 - u_1 = \frac{3h}{Rl} \left(P - \frac{4}{3}Q \right) \left[2 \left(\frac{x}{l} \right) - \left(\frac{x}{l} \right)^2 \right] \quad (2.12)$$

The expression above gives the validity criteria for equation 2.6. The equation 2.12 is positive if and only if $P - \frac{4}{3}Q > 0$, which means that the slipping can only occur under a loading which is superior to $\frac{4}{3}\mu pbh$. This value is denoted as critical loading P_{cri} . The critical deflection at the free point is denoted as q_{cri} . As there is no slip between the two clamped beams under a loading inferior to P_{cri} , the two beams can be regarded as stucked together and behave like a single block with doubled thickness. The critical amplitude to activate the slip is given by 2.13.

$$q_{cri} = \frac{P_{cri}l^3}{3EI_{doubled}} = \frac{\frac{4}{3}\mu pbhl^3}{3E \cdot \frac{1}{12}b(2h)^3} = \frac{2\mu pl^3}{3Eh^2}. \quad (2.13)$$

Here we can derive the relationship between the amplitude of deflection q and the quantity of energy dissipation. Firstly we need to express the deflection in the form of a product between amplitude and normalized shape function, as written in equation 2.14.

$$w(x) = \frac{q}{2} \left[3 \left(\frac{x}{l} \right)^2 - \left(\frac{x}{l} \right)^3 \right]. \quad (2.14)$$

According to relations 2.8 and 2.9, the longitudinal displacement in terms of amplitude q is given by

$$u_1 = \frac{1}{E} \int_0^x \sigma_{x_1} dx - \frac{h}{2} \frac{dw_1}{dx} = \frac{1}{E} \left(\frac{\mu pl}{h} x - \frac{\mu p}{2h} x^2 \right) - \frac{3hq}{4l} \left[2 \frac{x}{l} - \left(\frac{x}{l} \right)^2 \right] \quad (2.15)$$

$$u_2 = \frac{1}{E} \int_0^x \sigma_{x_2} dx + \frac{h}{2} \frac{dw_2}{dx} = -\frac{1}{E} \left(\frac{\mu pl}{h} x - \frac{\mu p}{2h} x^2 \right) + \frac{3hq}{4l} \left[2 \frac{x}{l} - \left(\frac{x}{l} \right)^2 \right]. \quad (2.16)$$

The energy dissipation can thus be obtained as

$$u_2 - u_1 = -\frac{2}{E} \left(\frac{\mu pl}{h} x - \frac{\mu p}{2h} x^2 \right) + \frac{3hq}{2l} \left[2 \frac{x}{l} - \left(\frac{x}{l} \right)^2 \right] \quad (2.17)$$

$$W_{dissip} = 4 \int_0^l \tau_{xy} \Delta u(x) b dx = 4\mu pb \int_0^l (u_2 - u_1) dx = 4\mu pbh \left(q - \frac{2\mu pl^3}{3Eh^2} \right). \quad (2.18)$$

The equation 2.18 gives another approach to obtain the critical amplitude by applying the criteria $W_{dissip} > 0$, it will give the same critical amplitude as by equation 2.13. Here a coefficient of 4 is multiplied before the integral based on the hypothesis that dissipated energy in a quarter of loading cycle is a quarter of the total energy dissipated in a full loading cycle. The next step consists of calculating the maximum elastic energy that the system can stock. The stocked energy can be divided into two parts: the energy related to elongation and the energy related to bending.

The elastic energy related to elongation of the beam can be obtained from the average normal stresses. It should be noted that the elongation energy obtained here is only valid for the stage of slipping.

$$E_{elongation} = \frac{1}{2} \int_v \sigma \cdot \varepsilon dv = \frac{1}{2} \int_v \sigma_x \cdot \frac{\sigma_x}{E} dv = \frac{1}{2E} \int_0^l \frac{\mu^2 p^2 (l-x)^2}{h^2} b h dx = \frac{\mu^2 p^2 l^3 b}{6Eh} \quad (2.19)$$

The elastic energy related to bending of the beam can be obtained from the deflection's expression 2.14.

$$\begin{aligned}
E_{bending} &= \frac{1}{2} \int_v \sigma \cdot \varepsilon dv = \frac{1}{2} \int_v E \left(\frac{\partial^2 w}{\partial x^2} z \right)^2 dv = \frac{E}{2} \int_l \left(\frac{\partial^2 w}{\partial x^2} \right)^2 \int_A z^2 dA dx \\
&= \frac{E bh^3}{2 \cdot 12} \int_0^L \left[\frac{1}{2} q \left(\frac{6}{l^2} - \frac{6x}{l^3} \right) \right]^2 dx \\
&= \frac{Ebh^3}{8l^3} q^2
\end{aligned} \tag{2.20}$$

From the previous deduction, we can establish the relationship between deflection amplitude and damping ratio. What's more, the expression for the dissipated energy is a piecewise function.

$$W_{dissip} = \begin{cases} 0 & \text{if } q \leq q_{cri} \\ 4\mu p b h \left(q - \frac{2\mu p l^3}{3Eh^2} \right) & \text{if } q > q_{cri}. \end{cases} \tag{2.21}$$

Similarly the damping coefficient is also a piecewise function and can be obtained by using the relation $E_{max} = E_{elongation} + E_{bending}$.

$$\eta = \begin{cases} 0 & \text{if } q \leq q_{cri} \\ \frac{2\mu p b h \left(q - \frac{2\mu p l^3}{3Eh^2} \right)}{\frac{\mu^2 p^2 l^3 b}{6Eh} + \frac{Ebh^3}{8l^3} q^2} & \text{if } q > q_{cri}. \end{cases} \tag{2.22}$$

The expression presented above is only valid for cases where the contact is assumed perfect and guaranteed along the total length of the beam. If the contact surface is rough or partially clamped, the contact area that contributes to energy dissipation may be modified. In this case, more detailed models need to be developed.

2.2.1.2 Model for rough surface

In order to take into account the global plane roughness of the contact surface, a global contact quality factor β is introduced and can be implemented in equation 2.21.

$$W_{dissip} = 4 \int_0^l \tau_{xy} \Delta u(x) b \beta dx = 4\beta \mu p b h \left(q - \frac{2\mu p l^3}{3Eh^2} \right). \tag{2.23}$$

The damping coefficient can thus be expressed by

$$\eta = \begin{cases} 0 & \text{if } q \leq q_{cri} \\ \frac{2\mu \beta p b h \left(q - \frac{2\mu p l^3}{3Eh^2} \right)}{\frac{\mu^2 p^2 l^3 b}{6Eh} + \frac{Ebh^3}{8l^3} q^2} & \text{if } q > q_{cri}. \end{cases} \tag{2.24}$$

2.2.1.3 Model for partially clamped surface

Here we consider a case where the two beams are not perfectly clamped, there is only one zone which is under perfect contact, which means that the global quality factor β is assumed to be 1 on this area. This particular characteristic can be modeled by a small modification in the integration's range. The range's length is noted by R and the center of the contact surface is noted by X_c . As the clamping pressure is no longer uniform on the contact interface, the expression for the normal stress is modified to a piecewise function.

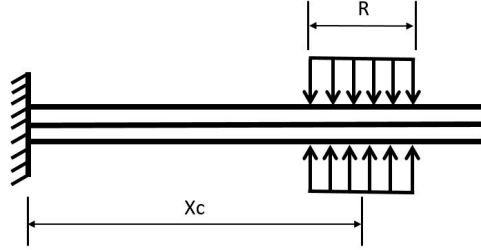


Figure 2.3: Partially clamped beam

$$\sigma_1 = \begin{cases} \frac{R\mu p}{h} & \text{if } 0 \leq x \leq X_c - \frac{R}{2} \\ -\frac{\mu p}{h} \left(x - X_c - \frac{R}{2} \right) & \text{if } X_c - \frac{R}{2} < x \leq X_c + \frac{R}{2} \\ 0 & \text{if } X_c + \frac{R}{2} < x \leq l. \end{cases} \quad (2.25)$$

$$\sigma_2 = \begin{cases} -\frac{R\mu p}{h} & \text{if } 0 \leq x \leq X_c - \frac{R}{2} \\ \frac{\mu p}{h} \left(x - X_c - \frac{R}{2} \right) & \text{if } X_c - \frac{R}{2} < x \leq X_c + \frac{R}{2} \\ 0 & \text{if } X_c + \frac{R}{2} < x \leq l. \end{cases} \quad (2.26)$$

The expressions for the elongation are thus different from equation 2.8 and 2.9.

$$u_1 = \frac{1}{E} \left[\int_0^{X_c - \frac{R}{2}} \frac{R\mu p}{h} dx - \int_{X_c - \frac{R}{2}}^x \frac{\mu p}{h} \left(x - X - \frac{R}{2} \right) dx \right] - \frac{h}{2} w'(x) \quad (2.27)$$

$$u_2 = \frac{1}{E} \left[- \int_0^{X_c - \frac{R}{2}} \frac{R\mu p}{h} dx + \int_{X_c - \frac{R}{2}}^x \frac{\mu p}{h} \left(x - X - \frac{R}{2} \right) dx \right] + \frac{h}{2} w'(x). \quad (2.28)$$

As the only zone of dissipation is $[X_c - \frac{R}{2}, X_c + \frac{R}{2}]$, the energy dissipation can be rewritten as

$$\begin{aligned} W_{dissip} &= 4\mu p b \int_{X_c - \frac{R}{2}}^{X_c + \frac{R}{2}} (u_2 - u_1) dx \\ &= \frac{bpR\mu}{6Eh^3} \{ 8l^3 \mu p R (R - 6X_c) - 3qEh^2 [R^2 + 12X_c (X - 2l)] \}. \end{aligned} \quad (2.29)$$

It's important to verify whether the critical amplitude will vary in terms of contact surface's area and position, so for this purpose we need to find the amplitude where $W_{dissip}(q_{cri}) = 0$. The q_{cri} can be obtained from equation 2.29.

$$q_{cri} = \frac{8l^3 \mu p R (R - 6X_c)}{3Eh^2 (R^2 - 24lX_c + 12X_c^2)}. \quad (2.30)$$

Here we set

$$f(X_c) = R^2 - 24lX_c + 12X_c^2, \quad \frac{R}{2} \leq X_c \leq l - \frac{R}{2} \quad (2.31)$$

In order to determine the sign of equation 2.30 in the range of X_c , we need to know its slope and two boundary values.

$$f'(X_c) = 24(X_c - l) < 0 \quad (2.32)$$

$$f\left(\frac{R}{2}\right) = 4R(R - 3l) < 0 \quad (2.33)$$

$$f\left(l - \frac{R}{2}\right) = 4R^2 - 12l^2 < 0 \quad (2.34)$$

Since $f'(X_c)$, $f\left(\frac{R}{2}\right)$ and $f\left(l - \frac{R}{2}\right)$ as well as $R - 6X_c$ are all negative in the range of X_c , we can confirm that expression 2.30 is the critical amplitude beyond which the structure is damped. It's evident that this critical amplitude is a function of contact surface's area and position. As the normal stress is no more uniform, the stocked elastic energy should also be modified as

$$E_{elongation} = \frac{b\mu^2 p^2 R^2 (6X_c - R)}{12Eh}. \quad (2.35)$$

When we take $R = l$ and $X_c = \frac{l}{2}$, we will find that equation 2.35 is the same as equation 2.19. Since the bending energy is only a function of deflection's form, it's not influenced by the distribution of normal stress. The damping ratio can thus be expressed by this more detailed model as

$$\eta = \begin{cases} 0 & \text{if } q \leq q_{cri} \\ \frac{\frac{bpR\mu}{6Ehl^3} \{-3qEh^2 [R^2 + 12X_c(X_c - 2l)] + 8l^3 \mu p R (R - 6X_c)\}}{2 \left[\frac{b\mu^2 p^2 R^2 (6X_c - R)}{12Eh} + \frac{Ebh^3}{8l^3} q^2 \right]} & \text{if } q > q_{cri}. \end{cases} \quad (2.36)$$

Equation 2.36 is a generalized version of equation 2.24 which enables a comprehensive parametric study of different influential factors like clamping pressure, coefficient of friction even the area and position of clamping forces. It's possible to implement different thicknesses in the development, but this procedure will complicate too much the expression. The study on thickness ratio will be conducted by numeric method in the following sections.

2.2.2 Analytical parametric studies

The beam's dimensions and mechanical properties used for numerical calculations are listed in table 2.1. The analytical parametric studies focus mainly on the influence of clamping pressure, coefficient of friction, contact area's size as well as its position. Since the purpose of the study is to find out the relationship between modal amplitude and friction damping, in each tracing the horizontal axis set to be the sweeping amplitude and the vertical axis to be the corresponding damping ratio. The dimensions used in the current study are listed in table 2.1.

Length (mm)	Width (mm)	Thickness (mm)	Young's modulus (MPa)	Poisson's ratio
400	30	4	210000	0.3

Table 2.1: Beam dimensions and mechanical properties

2.2.2.1 Influence of pressure

The study of the influence of pressure on damping ratio is conducted by the analytical model which assumes perfect contact along the whole length of the beam. The coefficient of friction is fixed at 0.3. The maximum amplitude is fixed at 8 mm, which is the total thickness of the assembled structure. The evolutions of damping ratio under four different pressures are illustrated in figure 2.4.

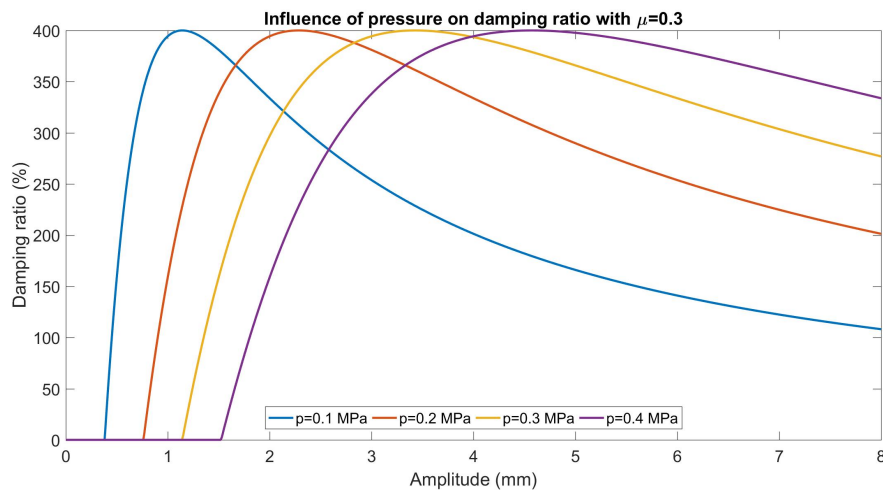


Figure 2.4: Influence of pressure on damping ratio

There are 6 important damping properties that can be summarized:

1. For a given structure, there exists a damping limit whatever the combination of clamping pressure and modal amplitude, for example the damping is bounded to 400 % in the current model.

2. For a given pressure, there exists an optimal modal amplitude under which the structure can reach its maximal damping capacity.
3. Once the maximum damping capacity is reached, the increase in modal modal amplitude will cause a decrease in damping capacity.
4. The bigger the clamping pressure is, the later the slipping occurs.
5. Under a given small modal amplitude ($q < 2$ mm in the current model), bigger clamping pressure may lead to weaker damping capacity.
6. Under a given big modal amplitude ($q > 6$ mm in the current model), bigger clamping pressure surely yield stronger damping capacity.

The fact that the damping capacity for a given structure is limited to a certain value indicates that the optimization of damping is feasible, for example in industrial applications the clamping pressure can be used as controlling parameter in adjusting the modal amplitude for assembled structures in resonance.

2.2.2.2 Influence of coefficient of friction

From the product μp both in the numerator and denominator of equation 2.36, the coefficient of friction μ and the clamping pressure p can take effect simultaneously on the damping ratio. It's logical to suppose that coefficient of friction has the same influence as clamping pressure.

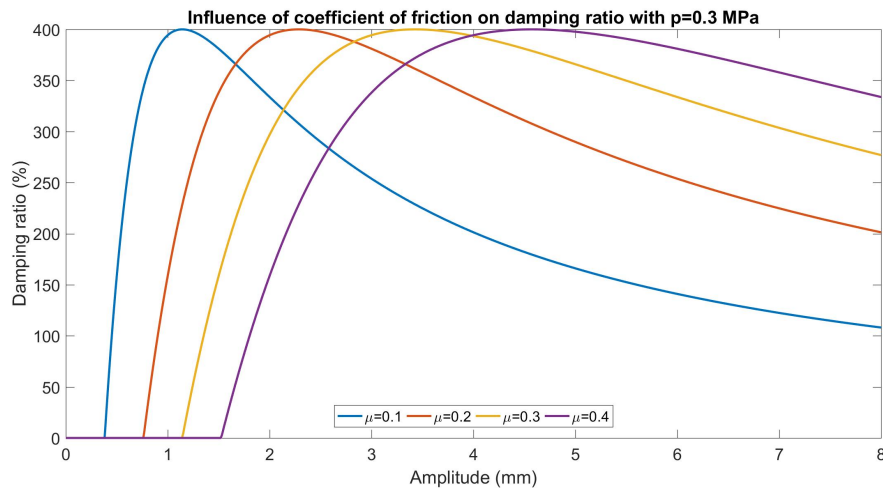


Figure 2.5: Influence of coefficient of friction on damping ratio

The study on the coefficient of friction is conducted with a uniform clamping pressure of 0.3 MPa. The evolutions of damping ratio under different coefficient of friction are illustrated in figure 2.5. The result is exactly the same as the evolutions

under the influence of clamping pressure. This observation confirms the hypothesis that the coefficient of friction plays the same role as the clamping pressure in terms of influence on damping capacity. But due to the difficulty in adjusting the coefficient of friction in real applications, clamping pressure is considered as the easiest parameter to be manipulated in damping control.

2.2.2.3 Influence of global contact quality

The global contact quality factor β is introduced to study the influence of surface's coarseness on damping capacity. An amplitude sweeping is applied to equation 2.24 and five different contact percentages are chosen from 0 to 100 %. The pressure is fixed at 0.3 MPa and the coefficient of friction at 0.3. The evolutions of damping ratio is presented in figure 2.6.

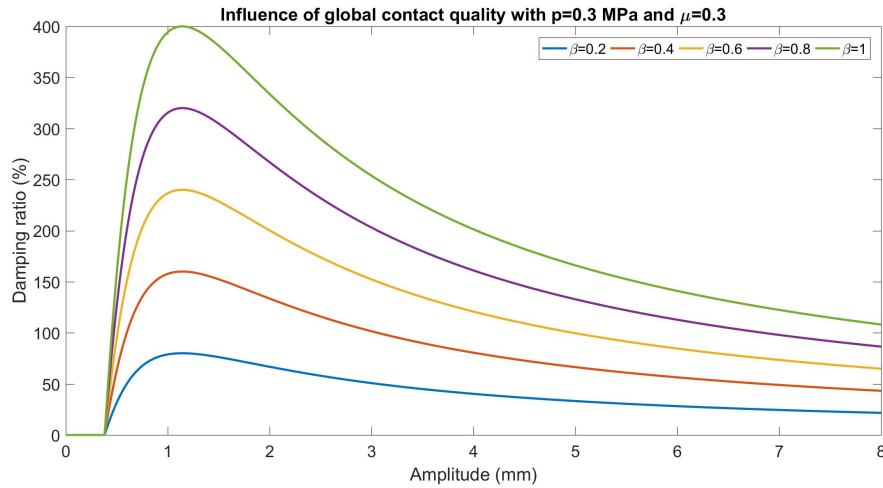


Figure 2.6: Influence of global contact quality on damping ratio

The global contact quality is shown to have no influence on the slipping activation point as well as the amplitude to reach the optimal damping. Since β is a simple linear multiplier to the dissipated energy, the damping capacity is linearly proportional to the contact surface percentage.

2.2.2.4 Influence of contact surface's position

In cases where the contact is not guaranteed on the whole contact interface, the position of clamp may modify the evolution of amplitude-damping ratio curve. In the current study, the surface under pressure is supposed to be perfectly clamped ($\beta = 1$). The calculation is based on equation 2.36 where the pressure is fixed at 0.3 MPa and the length of clamp is fixed at 50 mm. A sweeping in modal amplitude from 0 to 8 mm is conducted. The influence of clamping pad's position is illustrated in figure 2.7.

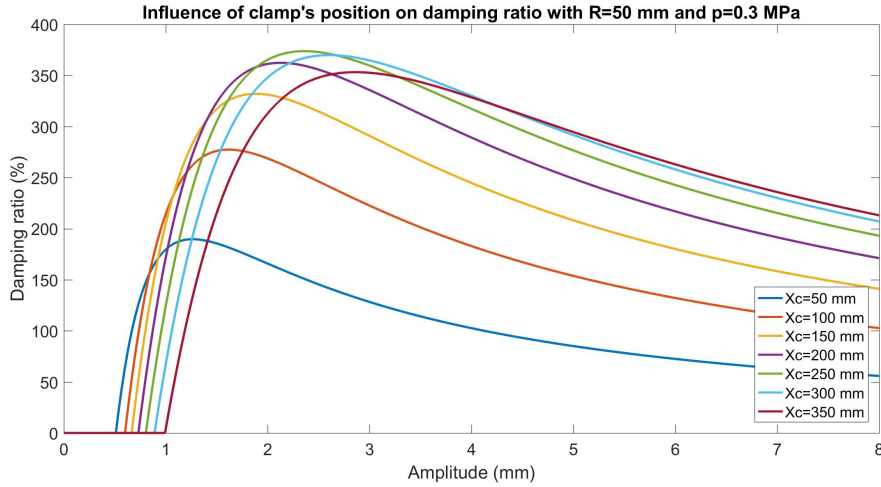


Figure 2.7: Influence of clamping pad's position on damping ratio

The parametric study shows that the clamping pad's position is a key factor in controlling the slipping activation point, it can also influence the the value of optimal damping as well as the amplitude corresponding to optimal damping. Several phenomena can be highlighted:

1. The further the clamping pad is situated from the encastre, the bigger the amplitude needed to activate slipping and logically, the bigger the amplitude needed to reach maximum damping.
2. For a given structure, some positions may lead to a relatively weak damping capacity than other positions. But there exists a position where the damping capacity of the whole structure can be optimized, in the current study this position is at around $X_c = 250$ mm.
3. For big modal amplitude ($q > 8$ mm), larger distance X_c between the clamping pad and the encastre yields stronger damping. But for small modal amplitude ($1 \text{ mm} < q < 3$ mm), there is no concrete correlation between distance X_c and damping capacity.

2.2.2.5 Influence of contact surface's area

Besides the contact surface's position, its area can also modify the damping characteristics of the assembled structure. In the current model, the center of clamping pad is situated at $X_c = 200$ mm, the clamping pressure is fixed at 0.3 MPa. The beam's width remains constant, 5 different clamping lengths R are used to modify the contact area in the study.

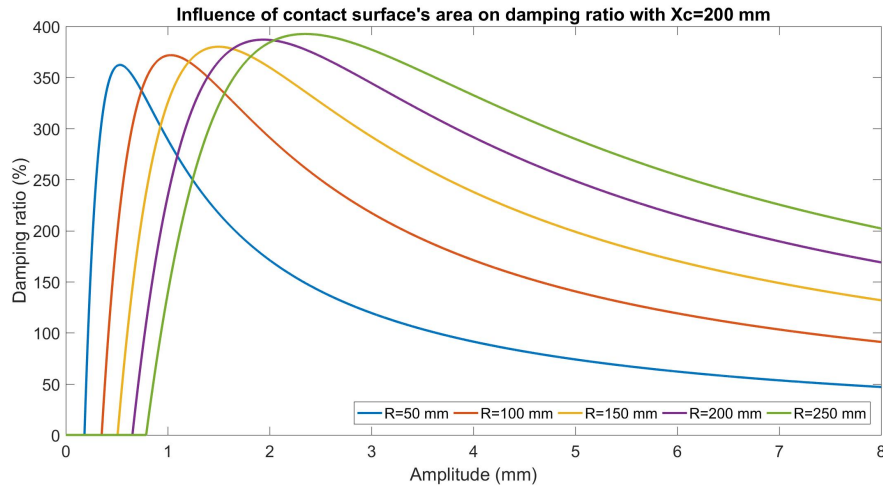


Figure 2.8: Influence of clamping pad's area on damping ratio

Besides the common characteristics of the first-order interface damping, three other features related to the influence of contact area can be found in figure 2.8.

1. the maximum damping ratio is proportional to the contact surface area. The bigger the contact area is, the more damped the structure can be at optimal damping amplitude.
2. The bigger the contact area is, the bigger the amplitude is needed to activate slipping.
3. The bigger the contact area is, the more damped the structure can be under large modal amplitude ($q > 3$ mm in the current model).

2.2.3 Numerical parametric studies

In order to study the influence of other complicated parameters like welding points, geometric defaults, thickness ratio even boundary conditions, analytical modelization is no longer capable of taking into account of these factors, in this case numerical study is necessary to give a qualitative estimation of the damping ratio under the influence of these influencing parameters.

2.2.3.1 Influence of welding point number

Welding is a commonly used fixation method in structure assembly. The structure's hardening by welding is largely acknowledged in industry but it's influence on damping is still not well investigated. In the current study, the plate is modeled by 2-D plane strain element with which the influence in the width's direction can be ignored. The welding points are uniformly distributed on the contact plan and the point pairs from the upper and lower contact surface are constrained to have the

same in-plane displacement. Different welding point numbers are tested and their influence on energies and damping ratio are illustrated as below.

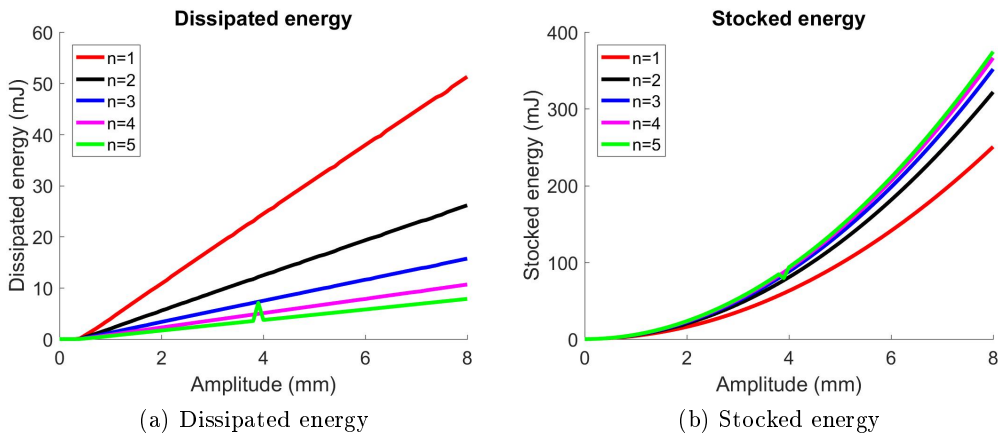


Figure 2.9: Influence of welding points number on dissipated and stocked energy

The dissipated energy is a linear function of modal amplitude, which is in coherence with equation 2.29 that presents a first-order relationship with modal amplitude. It reveals that the first-order relationship between the modal amplitude and the dissipated energy is conserved even with the presence of welding points. However the number of welding points can modify the quantity of dissipated energy. Due to the blockage of relative displacement, the more the welding points there are, the less the energy is dissipated. Besides, the slipping activation amplitude is independent of welding points number. From the figure 2.9b, the relationship between modal amplitude and stocked energy is no longer linear and presents a second-order characteristic, which is also in coherence with the analytical expression of stocked energy. The hardening of structure by a growing number of welding points is evident, but its effect is not proportional to the points number from the fact that the difference in stocked energy between 4 weldings and 5 weldings is negligible.

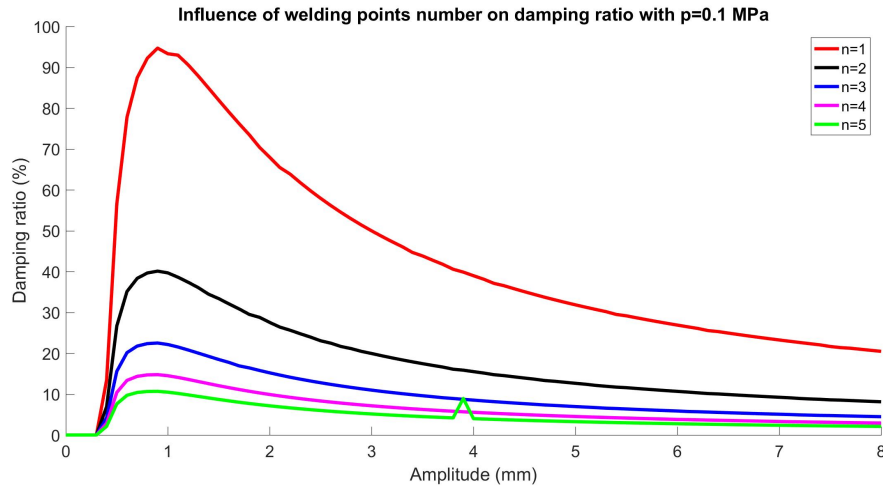


Figure 2.10: Influence of welding points number on damping ratio

Since the dissipated energy and stocked energy are respectively a negative and a positive correlation function of welding number, it can be concluded that less welding points will lead to a more damped structure.

2.2.3.2 Influence of thickness ratio

According to equation 2.27 and 2.28, the relative displacement between the upper and lower beam is a function of beam's thickness h , thus we can assume that the ratio of upper beam's thickness to lower beam's thickness is another factor that may influence the damping capacity in sandwich-type structures. In the current numerical study, the contact is assumed to be perfect on the whole interface and the sum of the two beam's thicknesses remains 8 mm, the only variable is the thickness ratio between them. The clamping pressure is fixed at 0.1 MPa and the modal amplitude ranges from 0 to 8 mm.

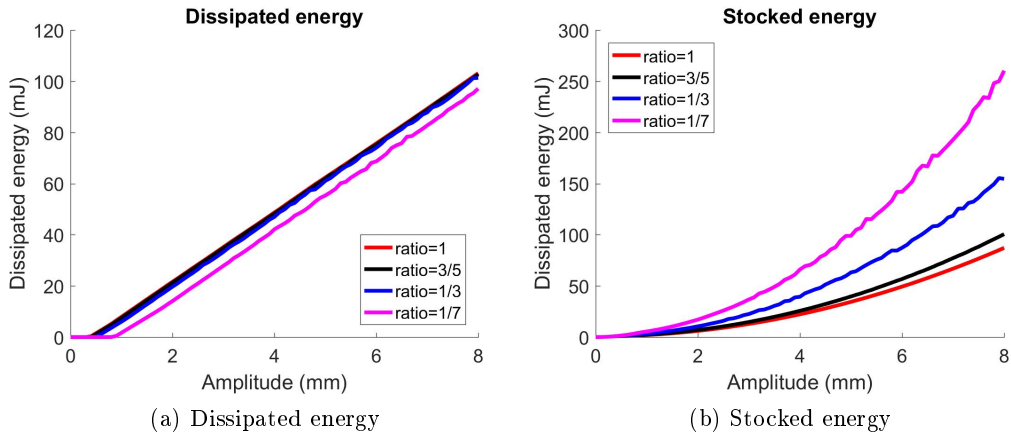


Figure 2.11: Influence of thickness ratio on dissipated and stocked energy

Similar to the phenomena presented in the study of welding points number, the dissipated energy is always a linear function of modal amplitude. However, unlike the welding number which can influence the tangent of the $E_{dissipation} - Amplitude$ relationship, the straight lines in 2.11a are parallel to each other which signifies that the thickness ratio doesn't modify the energy loss rate in terms of modal amplitude, but only influences the slipping activation point. The smaller the damping ratio is, the later the slipping occurs. Even though the total thickness of the assembled beam is maintained constant, which ensures a constant volume of the structure, the stocked energy can be influenced by the thickness ratio from the fact that smaller ratio can lead to a more elevated level of stocked energy.

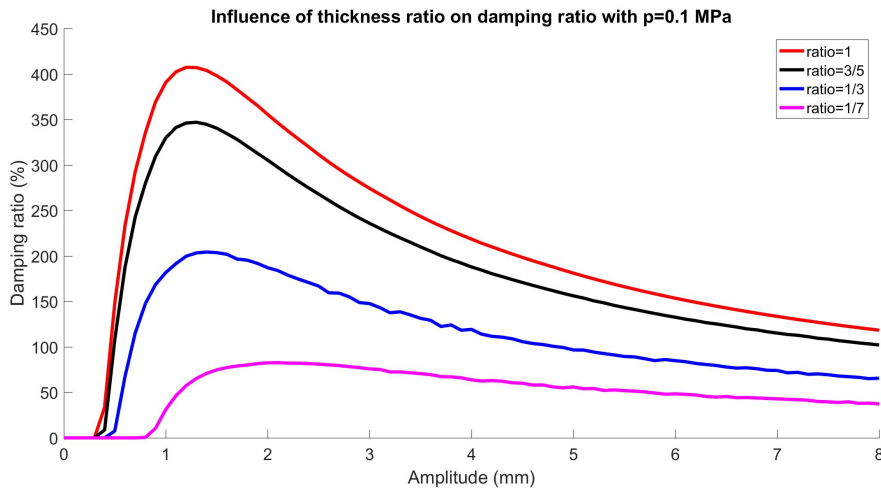


Figure 2.12: Influence of thickness ratio on damping ratio

After the slipping occurs, the maximum damping capacity can be reached when the two beams have the same thickness, the smaller the ratio is, the less damped

the structure becomes. The thickness ratio can be regarded as having no influence on optimal amplitude required for maximal damping, so that the maximal damping can only be considered as a function of clamping pressure and coefficient of friction in this study.

2.2.3.3 Influence of protrusion's height

Macroscopic geometric defaults due to machining imperfections cannot be ignored in damping calculation. The current and the next section are dedicated to the influence of macroscopic geometric default on damping formation. The defaults are modeled as protrusions only on the lower part of the contact interface as illustrated in figure 2.13. The protrusions are defined by splines whose curvature can be fixed by its horizontal interval and height. Given the number of protrusions, the height is the only variable that modifies the spline's curvature. In the current study, only one protrusion is modeled on the lower surface and the influence of 6 different heights are studied. The clamping pressure is fixed at 0.1 MPa.

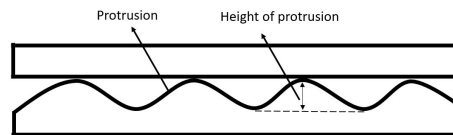


Figure 2.13: Illustration of protrusions on contact surface

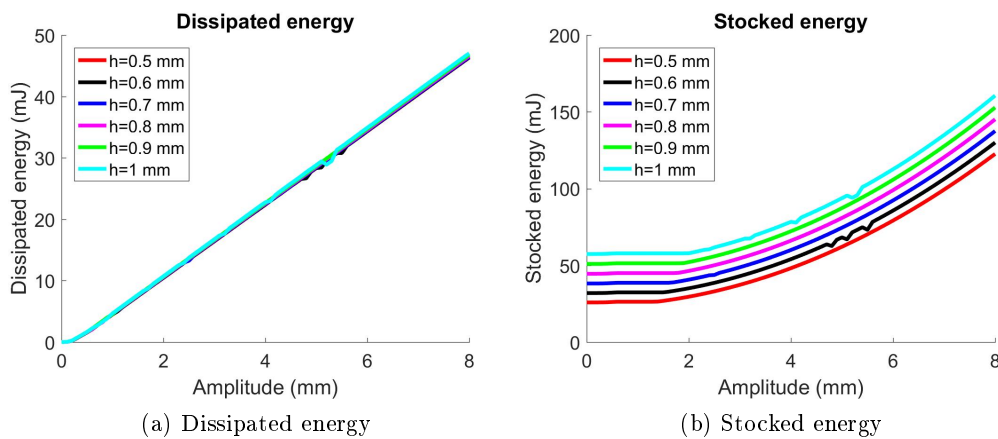


Figure 2.14: Influence of protrusion's height on dissipated and stocked energy

The protrusion's curvature is considered as having no significant influence on the dissipated energy since the energy evolutions in 2.14a are all superimposed together. However the stocked energy can be influenced by the protrusion's height due to the fact that the volume is linearly proportional to the thickness. The presence of non-

zero initial stocked energy is caused by the local stress concentration at the contact point of the protrusion during the pre-loading.

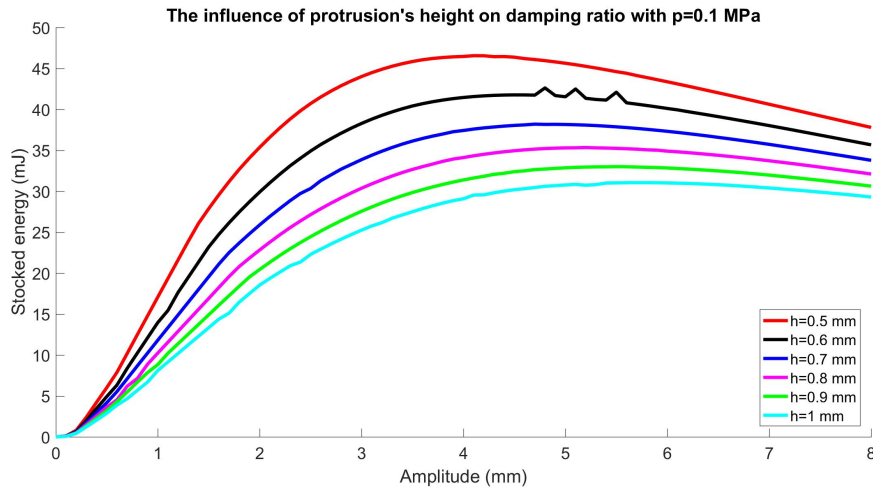


Figure 2.15: Influence of protrusion's height on damping ratio

The ratio of dissipated energy to the stocked energy is presented in figure 2.15. Since the curvature has almost no significant influence on dissipated energy, if we adopt the hypothesis that the changes in volume due to the modifications in height is negligible, the macroscopic protrusions height can be considered to have no influence on damping capacity.

2.2.3.4 Influence of protrusion's number

Based on the property of the previous section that the frictional damping doesn't depend on protrusion's curvature, the curvature's change due to horizontal interval's variation can be neglected and it is thus possible to isolate the influence of protrusion's number on damping ratio. In the current study, the protrusion's height is fixed at 0.5 mm and the clamping pressure is maintained at 0.1 MPa.

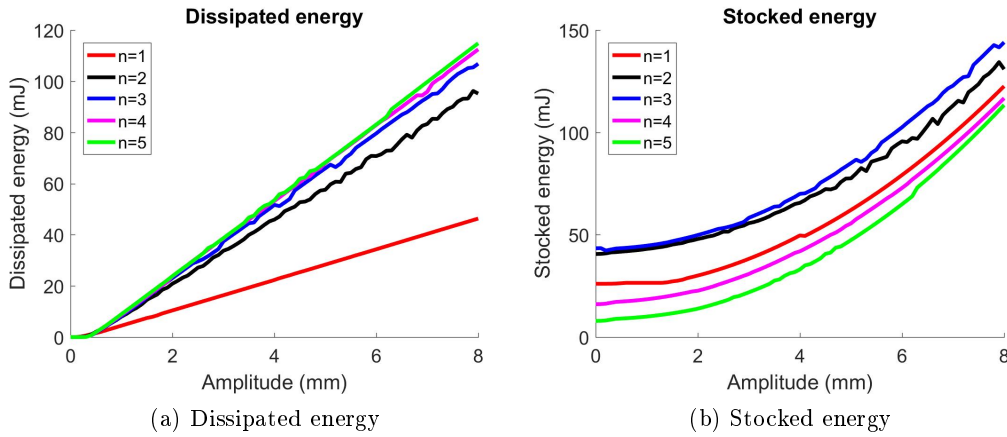


Figure 2.16: Influence of protrusion's number on dissipated and stocked energy

Based on the intuition that the contact area is directly related to the number of protrusions, the dissipated energy is surely sensitive to the change in protrusions number, which is also verified by the results in figure 2.16a. However there is no regular pattern in the relationship between dissipated energy and protrusions' number. This irregularity may be related to the fact that an infinite increase in protrusions' number is bound to lead to a limited value of contact surface, which in turn surely yields a limited damping capacity. As for the relationship in figure 2.16b, more protrusions seem to yield weaker stocked energy but the order between only 1 protrusion and 3 protrusions is inverse, which makes it difficult to find a linear relationship between the number of protrusions and the stocked energy.

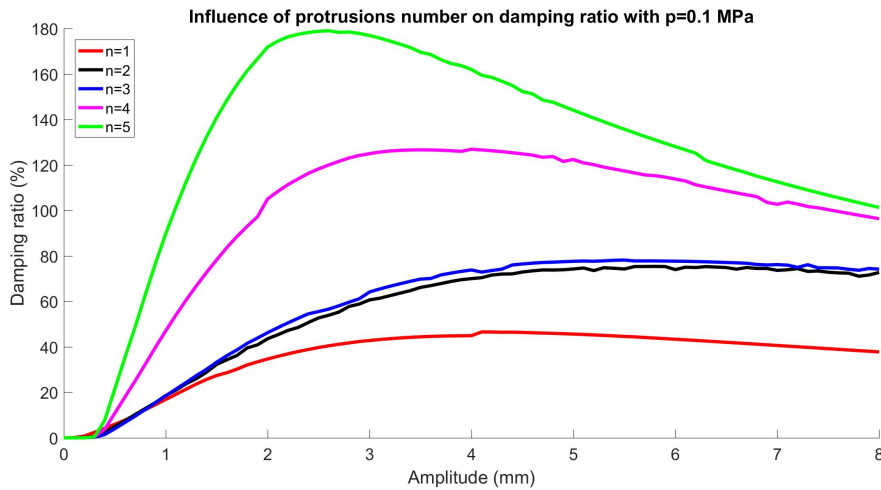


Figure 2.17: Influence of protrusion's number on damping ratio

According to the figure 2.17, 4 or 5 protrusions yield a behavior which is similar to a typical first-order damping where it's easy to locate an optimal modal amplitude,

however for 1 to 3 protrusions, the damping-amplitude relationship is more similar to an asymptote who cannot be optimized by simply finding an optimized amplitude, this phenomenon is present in second-order damping structures as will be detailed in the following sections. If we neglect the unusual behavior of 2 and 3 protrusions, more protrusions will in general lead to more damped system since more protrusions will result in a bigger contact surface.

2.2.3.5 Influence of endpoint locking

The previous sections show that the frictional damping is intrinsically a matter of energy dissipation on the contact surface, so that not only contact properties but also slipping distance can contribute to damping modifications. Since boundary conditions can have influence on slipping distance, the changes in boundary conditions at the free endpoint will inevitably modify the damping characteristics. Compared to the original free endpoint control configuration, an endpoint locking which implements a displacement equivalence at the endpoint is applied as the treatment configuration. The dissipated and stocked energy are respectively illustrated in figure 2.18a and in figure 2.18b.

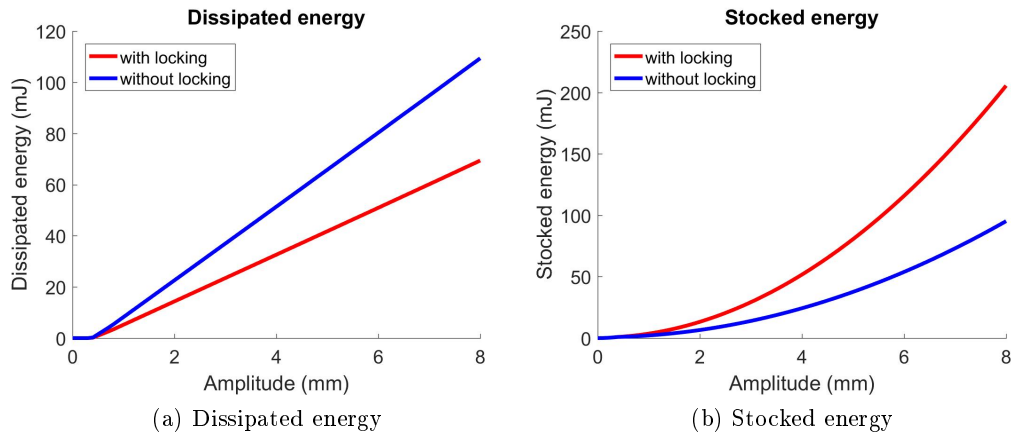


Figure 2.18: Influence of endpoint locking on dissipated and stocked energy

The figure 2.18a shows that more energy is dissipated without the presence of endpoint locking, which implies that endpoint locking is able to constrain the relative displacement at the contact surface. But the fact that the slipping takes place at the same amplitude indicates that the endpoint locking has no influence on slipping activation point. The figure on stocked energy points out that the endpoint locking can lead to a hardening which in consequence will lower the damping capacity of the structure.

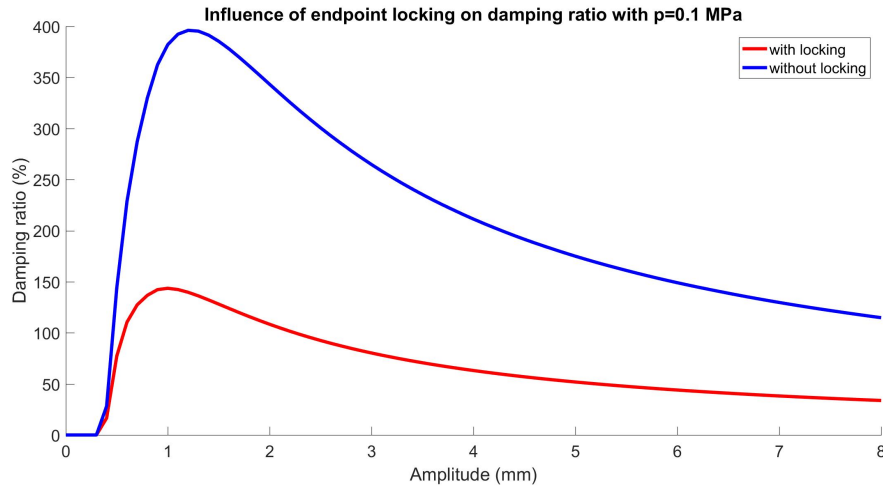


Figure 2.19: Influence of endpoint locking on damping ratio

The figure 2.19 illustrates clearly that the endpoint locking has significant influence on damping formation, since the application of endpoint locking is able to lower tremendously the damping capacity. This discovery also indicates that all methods that are apt to constrain the potential slipping should be avoided if the final goal is to make a more damped structure.

2.3 First-order boundary damping in rotational joint

2.3.1 Analytical modelization

In some flexural structures, even though translational displacement is restrained at fixed boundary borders, small rotational displacement can take place and the energy dissipation associated with them cannot be neglected. In order to study the characteristics of this damping mechanism, a simple academic cantilever beam model with one dissipative rotational boundary is employed and an analytical damping ratio expression is developed.

As is illustrated in figure 2.20, attached to the beam's left end point is a circular frictional damping pad, where the rotational displacement $\Delta\theta$ can be triggered by large modal amplitude. The coefficient of friction is designated as μ and the clamping pressure on the frictional pad as p .

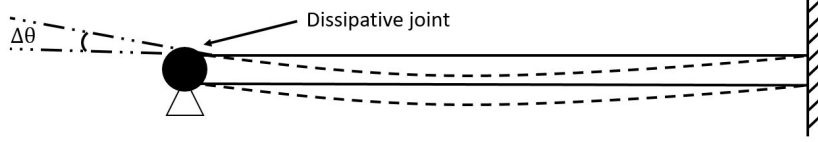


Figure 2.20: Sketch of rotational damping beam

The alternative sticking and slipping mechanism can be divided into two parts: For small modal amplitude, the clamp is firm enough to hold the end point to its original position, thus the clamping point can be regarded as encastre. Once the slipping is triggered, the end point switches to rotation and can be equivalent to a pinned connection under a friction-induced moment, as illustrated in figure 2.21.

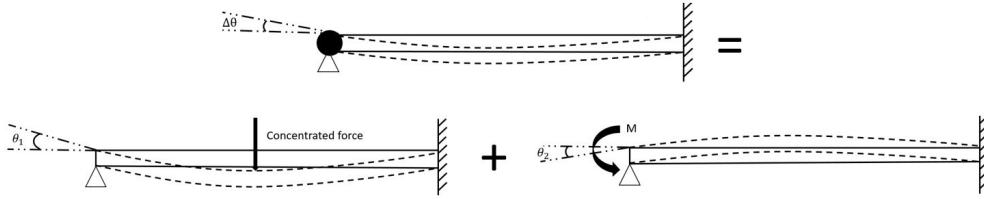


Figure 2.21: Decomposition of slipping state in rotational damping

The choice of imposed form is based on this interpretation: the first mode shape chosen is assimilated to the deflection under a mid-span concentrated load. In order to take into account the influence of end point friction, the second mode shape related to an endpoint moment should be superimposed on the first mode. According to this decomposition of mode shape, the deduction of damping ratio can be developed as follows.

The expression for a pinned-encastre beam under midspan concentrated load is

$$w_0(x) = \begin{cases} \frac{Px}{96EI}(3l^2 - 5x^2) & \text{if } 0 \leq x < \frac{l}{2} \\ \frac{P}{96EI}(x-l)^2(11x-2l) & \text{if } \frac{l}{2} \leq x < l. \end{cases} \quad (2.37)$$

The imposed mode shape can thus be formulated as a product of modal amplitude q with the normalized deflection with respect to the midspan displacement. The origin of x starts from the left end of the beam.

$$w(x) = q\bar{w}(x) = q \frac{w_0(x)}{w_0(\frac{l}{2})} = \begin{cases} \frac{8qx}{7l^3}(3l^2 - 5x^2) & \text{if } 0 \leq x < \frac{l}{2} \\ \frac{8q}{7l^3}(x-l)^2(11x-2l) & \text{if } \frac{l}{2} \leq x \leq l. \end{cases} \quad (2.38)$$

From the expression 2.38, the rotational angle θ_1 can be derived by a differentiation with respect to x

$$\theta_1 \Big|_{x=0} = \frac{\partial w}{\partial x} \Big|_{x=0} = \frac{24q(l^2 - 5x^2)}{7l^3} \Big|_{x=0} = \frac{24q}{7l}. \quad (2.39)$$

The pinned endpoint rotation under a moment M is

$$\theta_2 = \frac{Ml}{4EI}. \quad (2.40)$$

So the rotational displacement in a quarter of cycle at the clamped end point can be written as

$$\Delta\theta = \theta_1 - \theta_2 = \frac{24q}{7l} - \frac{Ml}{4EI}. \quad (2.41)$$

The moment resulting from the shear stress on the contact surface can be expressed as

$$M = \int_0^{2\pi} \int_0^R \mu pr^2 dr d\theta = \frac{2}{3} \mu p \pi R^3. \quad (2.42)$$

Once we have the rotational displacement and the corresponding moment, the energy dissipation in one cycle can easily be obtained.

$$W_{dissip} = 4M \left(\frac{24q}{7l} - \frac{Ml}{4EI} \right). \quad (2.43)$$

The second step is to express the stocked elastic energy in terms of modal amplitude q .

$$\begin{aligned} E_{max} &= \frac{1}{2} \int_v \sigma \cdot \varepsilon dv = \frac{1}{2} \int_v E \left(\frac{\partial^2 w}{\partial x^2} z \right)^2 dv = \frac{E}{2} \int_l \left(\frac{\partial^2 w}{\partial x^2} \right)^2 \int_A z^2 dA dx \\ &= \frac{EI}{2} \left[\int_0^{\frac{l}{2}} \left(-\frac{240qx}{7l^3} \right)^2 dx + \int_{\frac{l}{2}}^l \left(-\frac{48q(8l-11x)}{7l^3} \right)^2 dx \right] \\ &= \frac{384EIq^2}{7l^3}. \end{aligned} \quad (2.44)$$

The critical amplitude beyond which the slipping will occur can be obtained by equating the formula 2.43 to zero.

$$4M \left(\frac{24q}{7l} - \frac{Ml}{4EI} \right) = 0 \Rightarrow q_{cri} = \frac{7Ml^2}{96EI} \quad (2.45)$$

The expression for damping ratio is thus divided into two parts: one corresponds to sticking where there is no energy dissipation, another describes the state where slipping takes place and the damping ratio is no longer zero.

$$\eta = \begin{cases} 0 & \text{if } q \leq q_{cri} \\ \frac{4M\left(\frac{24q}{7l} - \frac{Ml}{4EI}\right)}{\frac{384EIq^2}{7l^3}} & \text{if } q > q_{cri}. \end{cases} \quad (2.46)$$

We can note from equation 2.46 that dissipated energy is a linear function of modal amplitude, however the influence of amplitude on stocked energy is quadratic.

2.3.2 Analytical parametric studies

In order to illustrate the influence of controlling parameters on rotational friction damping, two parametric studies are conducted on clamping pressure p and radius of the frictional pad R . As the coefficient of friction has the same influence as that of clamping pressure, its study is neglected in this section. The dimensions of the beam are the same as those in table 2.1. The coefficient of friction μ is set to be 0.3 and the amplitude range of interest q is from 0 to 5 mm.

2.3.2.1 Influence of pressure

The influence of pressure on rotational damping is presented in figure 2.22 on page 53. Five important conclusions can be drawn from the evolution of damping ratio:

1. Like the sandwich beam, there exists a damping limitation for a given structure, once the limit is reached, the damping capacity decreases with an increase in modal amplitude.
2. Larger amplitude is required under bigger clamping pressure to reach the damping limit.
3. The bigger the clamping pressure is, the later the slipping occurs.
4. For a given small modal amplitude ($q < 1$ mm), bigger clamping pressure may lead to weaker damping capacity.
5. For a given big modal amplitude ($q > 2$ mm), bigger clamping pressure surely yields stronger damping capacity.

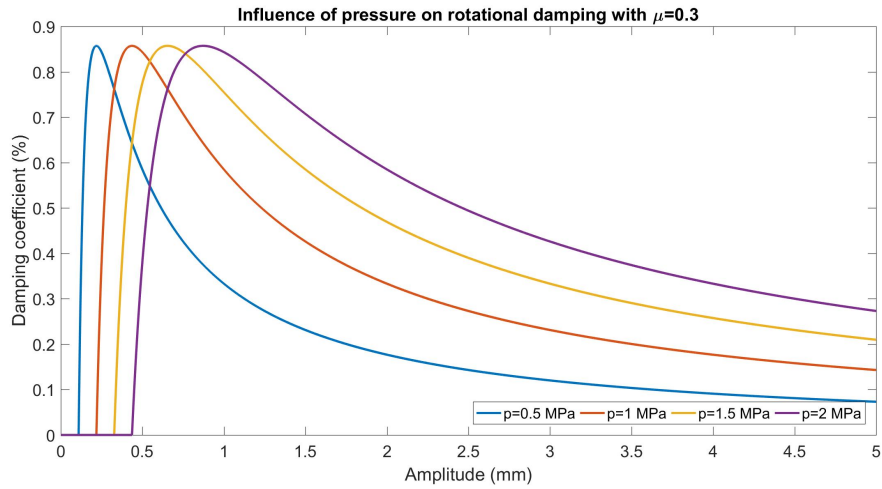


Figure 2.22: Influence of pressure on rotational damping

2.3.2.2 Influence of clamping pad's radius

The influence of clamping pad's radius is represented directly by variations in the frictional moment M . It can be observed from figure 2.23 that the evolution of damping ratio in terms of pad's radius is very similar to that of clamping pressure. The only difference is that the damping ratio is more sensitive to radius variations, this phenomenon can be explained by the fact that the dissipated energy is a function of R^6 , as formulated in equation 2.42 and 2.43.

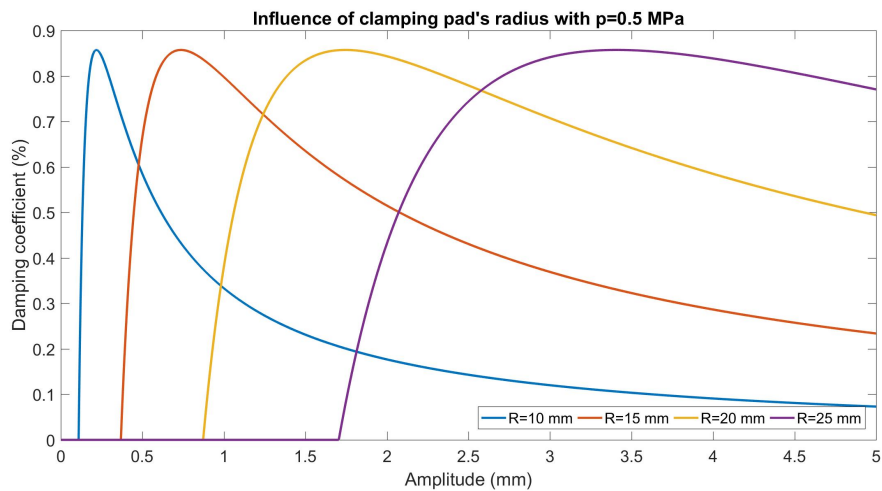


Figure 2.23: Influence of clamping pad's radius on rotational damping

2.4 Second-order boundary damping in von Kármán plate

Plates are viewed in engineering as three-dimensional components with one dimension, usually denoted by “thickness”, much smaller compared to the other two dimensions [51]. Traditional plate models such as the model of Kirchhoff-Love is developed based on small strain assumption, this model is incapable of taking into account the in-plane displacement that may be caused by large transverse deflections, e.g. the transverse deflection is of the same order of magnitude as the plate thickness. In this case, in order to study the frictional damping caused by boundary slipping under large deflections, the von Kármán plate model is thus adopted.

2.4.1 Geometric derivation of simplified Green strain

Figure 2.24 illustrates a plate under large deflection. The surface CAB defines the undeformed position and the surface $C'A'B'$ denotes the deformed state. When the plate is deformed from position CAB to position $C'A'B'$, the infinitesimal segment $AB = dx$ in the middle surface will move to $A'B'$. If the strain is truncated to the second order, the strain ε_x'' produced by large deflection in the x direction can be written as

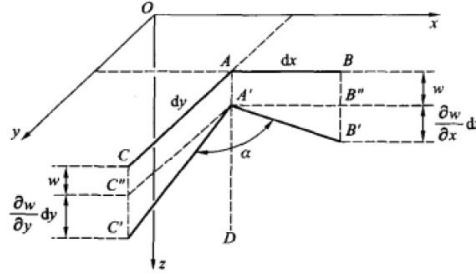


Figure 2.24: Geometric illustration of Green strain

$$\begin{aligned}\varepsilon_x'' &= \frac{A'B' - AB}{AB} = \frac{\left[dx^2 - \left(\frac{\partial w}{\partial x} dx \right)^2 \right]^{\frac{1}{2}} - dx}{dx} \\ &= \left[1 + \left(\frac{\partial w}{\partial x} \right)^2 \right]^{\frac{1}{2}} - 1.\end{aligned}\quad (2.47)$$

If we consider that $\frac{\partial w}{\partial x}$ is small and according to the approximation $(1+x)^n \approx 1+nx$, the equation 2.47 can be written as

$$\varepsilon_x'' = \frac{1}{2} \left(\frac{\partial w}{\partial x} \right)^2. \quad (2.48)$$

Similarly the second order strain induced by w in the y direction ε_y'' can be written as

$$\varepsilon_y'' = \frac{1}{2} \left(\frac{\partial w}{\partial y} \right)^2. \quad (2.49)$$

Here we define the directional cosines of segment $A'B'$ as l_1 , m_1 and n_1 respectively to the x , y and z axis. If small quantities of third order and above are neglected

$$m_1 = 0, \quad n_1 = \cos \angle B'A'D = \sin \angle B'A'B'' = \frac{\partial w}{\partial x}. \quad (2.50)$$

Similarly, we designate the directional cosines of $A'C'$ as l_2 , m_2 and n_2 where

$$l_2 = 0, \quad n_2 = \cos \angle C'A'D = \sin \angle C'A'C'' = \frac{\partial w}{\partial y}. \quad (2.51)$$

The angle α between $A'B'$ and $A'C'$ can thus be expressed as

$$\cos \alpha = l_1 l_2 + m_1 m_2 + n_1 n_2 = \frac{\partial w}{\partial x} \frac{\partial w}{\partial y}. \quad (2.52)$$

According to the definition of shear strain $\gamma_{xy} = \frac{\pi}{2} - \alpha$, if we neglect the small quantities of third order and above,

$$\gamma_{xy} = \sin \gamma_{xy} = \sin \left(\frac{\pi}{2} - \alpha \right) = \cos \alpha = \frac{\partial w}{\partial x} \frac{\partial w}{\partial y}. \quad (2.53)$$

The total strain can thus be obtained by superimposing the middle-plane strain due to in-plane displacement with the strain induced by large deflection.

$$\varepsilon_x = \frac{\partial u}{\partial x} + \frac{1}{2} \left(\frac{\partial w}{\partial x} \right)^2 \quad (2.54)$$

$$\varepsilon_y = \frac{\partial v}{\partial y} + \frac{1}{2} \left(\frac{\partial w}{\partial y} \right)^2 \quad (2.55)$$

$$\varepsilon_{xy} = \frac{\partial u}{\partial y} + \frac{\partial v}{\partial x} + \frac{\partial w}{\partial x} \frac{\partial w}{\partial y}. \quad (2.56)$$

2.4.2 Analytical modelization

The model to be used in this section is illustrated in figure 2.25, the left boundary is an encastre and the right boundary is under a uniform pressure p which ensures a perfect frictional contact with the support. Once the plate is under a certain cyclic excitation, the corresponding vibration mode in the transverse direction will trigger an in-plane retract at the frictional bord, which in turn produces a relative displacement and accordingly an energy dissipation, this is where the damping occurs. The large strain theory implies that in-plane strain is a function of transverse displacement w , it is thus logical to suppose that the damping is also a function of

deformed shape and it's worthwhile to establish a relationship between mode shape and damping capacity. The solution to the in-plane displacement problem on von Kármán plate can follow the previously introduced method based on imposed deflection. To simplify the problem, the plate is considered to be infinitely long in the width and the influence in the y direction can be neglected.

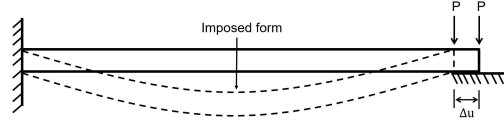


Figure 2.25: Sketch of boundary friction model

The normalized imposed form is a cosine function of x .

$$w_n(x) = \frac{1}{2} \left(\cos \frac{2\pi}{L}x - 1 \right). \quad (2.57)$$

The imposed displacement with an amplifier q as variable can thus be expressed as

$$w(x) = \frac{q}{2} (\cos \alpha x - 1), \quad \alpha = \frac{2\pi}{L}. \quad (2.58)$$

The first and second derivatives of the shape function with respect to x are

$$\frac{\partial w}{\partial x} = -\frac{1}{2}q\alpha \sin \alpha x, \quad \frac{\partial^2 w}{\partial x^2} = -\frac{1}{2}q\alpha^2 \cos \alpha x. \quad (2.59)$$

According to the in-plane strain under large deflection in equation 2.54 and the Hooke's law

$$\sigma_{ij} = \frac{E}{1-\nu^2} [(1-\nu)\varepsilon_{ij} + \varepsilon_{kk}\delta_{ij}], \quad \delta_{ij} : \text{Kronecker } \delta. \quad (2.60)$$

The normal and shear stress can be written as

$$\sigma_x = \frac{E}{1-\nu^2} (\varepsilon_x + \nu\varepsilon_y), \quad \sigma_{xy} = \frac{E}{2(1+\nu)} \varepsilon_{xy}. \quad (2.61)$$

The plate deformation can be divided into two stages. The first stage corresponds to sticking where the traverse deflection is not big enough to produce a traction force that surpasses friction force limit, so there is no energy dissipation in this stage. Once the deflection is big enough to trigger slipping, the reaction shear pressure at the slipping boundary is saturated to μp and the system enters a damping stage.

According to the stress equilibrium relationship $\sigma_{ij,j} = 0$ and the hypothesis that the influence from y direction is neglected, the equilibrium equation is thus simplified to

$$\frac{\partial \sigma_x}{\partial x} = 0 \implies \frac{E}{1-\nu^2} \left(\frac{\partial^2 u}{\partial x^2} + \frac{\partial w}{\partial x} \frac{\partial^2 w}{\partial x^2} \right) = 0. \quad (2.62)$$

We can integrate equation 2.60 to obtain the expression for in-plane displacement

$$\begin{aligned} \frac{\partial^2 u}{\partial x^2} + \left(-\frac{q}{2} \alpha \sin \alpha x \right) \left(-\frac{q}{2} \alpha^2 \cos \alpha x \right) &= 0 \\ u(x) &= \frac{1}{32} q^2 \alpha \sin 2\alpha x + C_1 x + C_2. \end{aligned} \quad (2.63)$$

Before the slipping occurs, the plate's friction point can be treated as an encastre, the rotations and translations are blocked. Here we use the translation boundary conditions to calculate the unknown coefficients.

$$u(0) = 0, \quad u(L) = 0 \implies C_1 = 0, \quad C_2 = 0. \quad (2.64)$$

The expression for in-plane displacement before slipping is

$$u(x) = \frac{1}{32} q^2 \alpha \sin 2\alpha x. \quad (2.65)$$

At this moment the strain on the cross section can be written as

$$\varepsilon_x = \frac{\partial u}{\partial x} + \frac{1}{2} \left(\frac{\partial w}{\partial x} \right)^2 = \frac{q^2 \alpha^2}{16} \cos 2\alpha x + \frac{q^2 \alpha^2}{8} \sin^2 \alpha x = \frac{1}{16} q^2 \alpha^2. \quad (2.66)$$

It should be noted that the strain on the cross section is homogeneous along the length of the plate, thus we can assert that the plate is iso-stress in the longitudinal direction.

$$N(x) = EA\varepsilon_x = \frac{1}{16} EAq^2 \alpha^2. \quad (2.67)$$

Equation 2.65 is important for the derivation of critical amplitude of displacement beyond which the slipping can be activated. Here the frictional contact area is defined as S , the clamping pressure as p and the coefficient of friction as μ .

$$\frac{1}{16} EAq^2 \alpha^2 = \mu p S \implies q_{cri} = \frac{4}{\alpha} \sqrt{\frac{\mu p S}{EA}}. \quad (2.68)$$

After the slipping occurs, the normal force in the plate is saturated to the value $\mu p S$.

$$\begin{aligned} N(x) &= EA\varepsilon_x = EA \left(\frac{\partial u}{\partial x} + \frac{1}{8} q^2 \alpha^2 \sin^2 \alpha x \right) = \mu p S \\ \frac{\partial u}{\partial x} &= \frac{\mu p S}{EA} - \frac{1}{16} q^2 \alpha^2 + \frac{1}{16} q^2 \alpha^2 \cos 2\alpha x \\ u(x) &= \left(\frac{\mu p S}{EA} - \frac{1}{16} q^2 \alpha^2 \right) x + \frac{1}{32} q^2 \alpha \sin 2\alpha x + C. \end{aligned} \quad (2.69)$$

Since there is only one unknown coefficient, the boundary condition at the encastre is sufficient to determine it.

$$u(0) = 0 \implies C = 0. \quad (2.70)$$

In this way the in-plane displacement expression after slipping is given by

$$u(x) = \left(\frac{\mu p S}{EA} - \frac{1}{16} q^2 \alpha^2 \right) x + \frac{1}{32} q^2 \alpha \sin 2\alpha x. \quad (2.71)$$

The displacement at the slipping boundary can be written as

$$u(L) = \left(\frac{\mu p S}{EA} - \frac{1}{16} q^2 \alpha^2 \right) L. \quad (2.72)$$

Even though the slipping may occur under certain deflection amplitude, energy dissipation may not take place due to compression effect during the releasing process, so it's necessary to determine the validity criteria in terms of amplitude for energy dissipation calculation. The effective amplitude beyond which energy dissipation can continue is designated as q_e . During the releasing, the frictional force is in the opposite direction until the moment when the deflection changes direction, this implies that when the plate recovers to its original position, there is a compressing force directing to the encastre on the slipping boundary. The slipping boundary's displacement under this pure frictional force is called critical displacement u_{cri} .

$$u_{cri} = \frac{\mu p S}{EA} L. \quad (2.73)$$

The displacement at the slipping boundary must be superior to u_{cri} to enable a continuous energy dissipation.

$$\begin{aligned} u(L) &= \left(\frac{\mu p S}{EA} - \frac{1}{16} q^2 \alpha^2 \right) L > \frac{\mu p S}{EA} L \\ q_e &= \frac{4}{\alpha} \sqrt{\frac{2\mu p S}{EA}}. \end{aligned} \quad (2.74)$$

We can see that q_e is independent of plate's length. Another important relationship to be extracted is

$$\frac{q_e}{q_{cri}} = \sqrt{2}. \quad (2.75)$$

The previous derivation describes only the behavior of a quarter cycle. Here we adopt the hypothesis that the dissipated energy is 4 times the dissipated in a quarter cycle, the total energy dissipation can thus be expressed as follows

$$\Delta E = \begin{cases} 0 & \text{if } q < q_e \\ 4\mu p S L \left(\frac{1}{16} q^2 \alpha^2 - \frac{2\mu p S}{EA} \right) & \text{if } q \geq q_e. \end{cases} \quad (2.76)$$

The stocked elastic energy can be divided into two parts: energy due to elongation and energy due to bending. The elongation elastic energy will be saturated when the normal force reaches $\mu p S$.

$$E_{elongation} = \frac{1}{2} \int_v \sigma \cdot \varepsilon dv = \frac{1}{2} EAL \left(\frac{q^2 \alpha^2}{16} \right)^2 = \frac{1}{512} EAL q^4 \alpha^4 = \frac{\mu^2 p^2 S^2 L}{2EA}. \quad (2.77)$$

The bending energy is a function of plate's curvature, so the bending strain can still increase regardless of normal force saturation, thus the bending stocked energy is a function of maximum shape amplitude q .

$$\begin{aligned} E_{bending} &= \frac{1}{2} \int_v \sigma \cdot \varepsilon dv = \frac{1}{2} \int_v E \left(\frac{\partial^2 w}{\partial x^2} z \right)^2 dv = \frac{E}{2} \int_l \left(\frac{\partial^2 w}{\partial x^2} \right)^2 \int_A z^2 dA dx \\ &= \frac{E b h^3}{2 \cdot 12} \int_0^L \left(-\frac{q}{2} \alpha^2 \cos \alpha x \right)^2 dx \\ &= \frac{E b h^3 q^2 \alpha^4 L}{192}. \end{aligned} \quad (2.78)$$

The damping ratio can thus be expressed as

$$\eta = \begin{cases} 0 & \text{if } q < q_e \\ \frac{4\mu p S \left(\frac{1}{16} q^2 \alpha^2 - \frac{2\mu p S}{EA} \right)}{\frac{\mu^2 p^2 S^2}{2EA} + \frac{E b h^3 q^2 \alpha^4}{192}} & \text{if } q \geq q_e. \end{cases} \quad (2.79)$$

It can be seen that the damping ratio is independent of the plate's length and the dissipated energy on the numerator is a quadratic equation of shape amplitude q , where the name second-order damping comes from.

2.4.3 Analytical expression of slipping boundary's trajectory

When the plate is under transverse deflection, the slipping boundary is in a cyclic shrinking movement. Different from the kinetics in the sandwich plate, where every slipping point can return to its original position in one cycle, the slipping boundary in von Kármán plate cannot be restored to its starting point, this is one of the main features of the current second-order damping model. The temporal behavior of the slipping point can be expressed by analytical method. The boundary movement in the stable state can be divided into four phases: sticking-slipping-sticking-slipping.

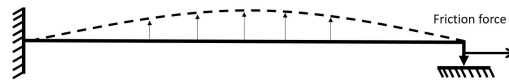


Figure 2.26: The position of phase 1

In the first sticking phase, the slipping point is blocked by the friction force and stays in its compressed position. The in-plane displacement can be described by equation 2.63 with the boundary condition $u(0) = 0$ and $u(L) = -\mu pSL/EA$. The in-plane displacement can thus be written as

$$u(x) = \frac{1}{32}q^2\alpha \sin 2\alpha x - \frac{\mu pSL}{EA}. \quad (2.80)$$

The strain corresponding to this displacement field is expressed as

$$\varepsilon_x = \frac{1}{16}q^2\alpha^2 - \frac{\mu pS}{EA}. \quad (2.81)$$

The maximum amplitude under which the structure can sustain its current position can be obtained by the force criteria,

$$\begin{aligned} N &< \mu pS, \\ EA \left(\frac{1}{16}q^2\alpha^2 - \frac{\mu pS}{EA} \right) &< \mu pS, \\ q &< \frac{4}{\alpha} \sqrt{\frac{2\mu pS}{EA}}. \end{aligned} \quad (2.82)$$

which is identical to expression 2.74. It signifies that in the range of $q \in \left[0, \frac{4}{\alpha} \sqrt{\frac{2\mu pS}{EA}} \right]$, the boundary displacement $u(L) = -\frac{\mu pSL}{EA}$.

If the modal amplitude continues to increase, the tangential frictional force will reach the maximum value μPS that the clamping pressure can provide, in this case the tangential force is saturated to the maximum friction force and the clamped point starts to slip. During this slipping phase, the friction force is maintained in its previous direction and points to the right.

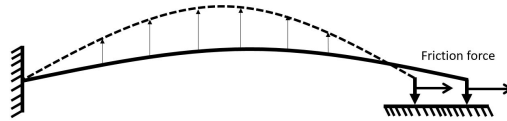


Figure 2.27: The position of phase 2

The force boundary condition should be used in the second phase to derive the slipping distance. Exactly the same with the derivation method in expression 2.69, the in-plane force is saturated to μPS . With the encastre boundary condition, the slipping point's displacement can be expressed by expression 2.72.

It means that during the second phase with slipping, if modal amplitude q in within the range of $q \in \left[\frac{4}{\alpha} \sqrt{\frac{2\mu pS}{EA}}, q_{max} \right]$, the boundary displacement is written

$$\text{as } u(L) = \left(\frac{\mu p S}{EA} - \frac{1}{16} q^2 \alpha^2 \right) L.$$

Once the maximum modal amplitude is reached, the deformed plate starts to return to its original position, the clamped point re-enters the sticking phase. The frictional force changes direction and points to the encastre point.

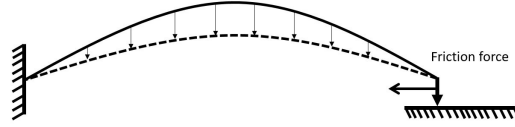


Figure 2.28: The position of phase 3

The clamped point is blocked in its previous position of phase 2, which is $\left(\frac{\mu p S}{EA} - \frac{1}{16} q_{max}^2 \alpha^2 \right) L$. The key information to be extracted in phase 3 is to determine until which amplitude level the structure can stay within the sticking phase. To this end, the constant C_1 in expression 2.64 needs to be re-evaluated.

$$u(L) = \left(\frac{\mu p S}{EA} - \frac{1}{16} q_{max}^2 \alpha^2 \right) L = C_1 L \quad \Longrightarrow \quad C_1 = \frac{\mu p S}{EA} - \frac{1}{16} q_{max}^2 \alpha^2. \quad (2.83)$$

Substitute coefficient C_1 obtained in 2.83 into expression 2.63 and write the in-plane force in the condition of sticking compression,

$$N = EA \left(\frac{1}{16} q^2 \alpha^2 + \frac{\mu p S}{EA} - \frac{1}{16} q_{max}^2 \alpha^2 \right), \quad (2.84)$$

the switching amplitude can be derived by equating the in-plane force to $-\mu p S$.

$$EA \left(\frac{1}{16} q^2 \alpha^2 + \frac{\mu p S}{EA} - \frac{1}{16} q_{max}^2 \alpha^2 \right) = -\mu p S \quad (2.85)$$

$$q = \sqrt{q_{max}^2 - \frac{32\mu p S}{EA\alpha^2}}.$$

From the development above, the amplitude boundary for sticking phase can be determined. When q is within the range of $q \in \left[\sqrt{q_{max}^2 - \frac{32\mu p S}{EA\alpha^2}}, q_{max} \right]$, the clamped end stays in its sticking position $u(L) = \left(\frac{\mu p S}{EA} - \frac{1}{16} q_{max}^2 \alpha^2 \right) L$.

The fourth phase corresponds to the re-entry into the slipping phase. The deformed plate continues to go back to its original position while the saturated friction force points always to the encastre. When the plate regains its flatness, the plate is in compression due to the remaining left-pointing friction force, so that it is impossible to be restored to its starting position, where the plate is in a zero-stress

state.

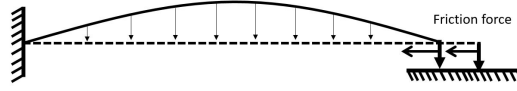


Figure 2.29: The position of phase 4

Since the internal force is known in the fourth phase, force boundary condition can be used to derive the expression of boundary point's displacement. By using equation 2.69, the internal force can be expressed as

$$N(x) = EA \left(\frac{\partial u}{\partial x} + \frac{1}{8} q^2 \alpha^2 \sin^2 \alpha x \right) = -\mu p S. \quad (2.86)$$

Apply the encastre boundary condition $u(0) = 0$ and solve for $u(x)$, the in-plane displacement field can be written as

$$u(x) = \left(-\frac{\mu p S}{EA} - \frac{1}{16} q^2 \alpha^2 \right) x + \frac{1}{32} q^2 \alpha \sin 2\alpha x. \quad (2.87)$$

Substitute $x = L$ into equation 2.87, we can get the expression for slipping point's displacement during the recovery process when q is in the range of $q \in \left[0, \sqrt{q_{max}^2 - \frac{32\mu p S}{EA\alpha^2}} \right]$.

$$u(L) = \left(-\frac{\mu p S}{EA} - \frac{1}{16} q^2 \alpha^2 \right) L. \quad (2.88)$$

In a half cycle of vibration, the sticking and slipping transitions can be divided into four phases. To illustrate the boundary's trajectory in full cycles and analyze the influence that the pressure can have on the trajectory, the same modal amplitude is imposed on the structure in a sinusoidal way $q = q_{max} \sin \omega t$ for each of the three different pressures applied. The dimensions of the plate are listed in table 2.1 on page 37.

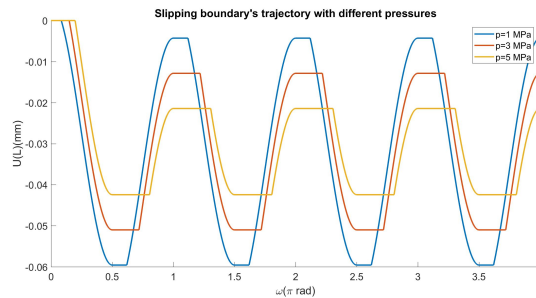


Figure 2.30: Slipping boundary trajectories under 3 different pressures

As mentioned above, the slipping end cannot return to its origin as in the following cycles the restarting point where $q = 0$ is always in a pre-compressed state. So that in the following sections dealing with damping quantification, the energy dissipation is evaluated from the second cycle. Regarding the influence of clamping pressure, a smaller pressure is shown to enable an earlier slipping and a longer slipping distance. If the pressure increases, the slipping will be activated under a bigger modal amplitude. For the reason that the compression effect in the course of releasing has a positive relation with the clamping pressure, the end point is more likely to be blocked farther from the encastre under a bigger pressure. Another phenomenon to be noted is that the slipping end point enters sticking at the same time regardless of the clamping pressure, however to reactivate slipping, a bigger pressure will postpone the reactivation to a bigger amplitude. Due to the property that slipping-sticking transition can be influenced by clamping pressure, it's natural to assume that friction damping is sensitive to pressure on the contact surface. This assumption is to be verified in the following sections with an energetic approach.

2.4.4 Analytical parametric studies

Similar to the parametric studies in the first-order interface damping, the influence of clamping pressure, coefficient of friction as well as contact surface area are to be analyzed in this section. The dimensions of the plate are listed in table 2.1 on page 37.

2.4.4.1 Influence of clamping pressure

In the parametric study on clamping pressure, the coefficient of friction μ is fixed at 0.3 and the contact surface area is 300 mm^2 , which corresponds to a contact band width of 10 mm. An amplitude sweeping from 0 to 3 mm is conducted on the model to trace the evolution of damping ratio in terms of displacement amplitude.

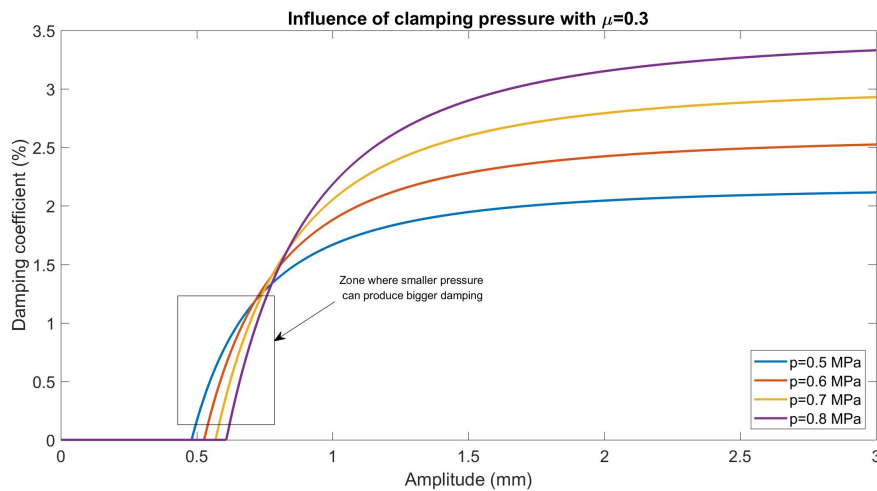


Figure 2.31: Influence of clamping pressure on damping ratio

Figure 2.31 illustrates the evolution of second-order damping ratio under 4 different clamping pressures. There are 6 characteristics to be highlighted in comparison with the first-order damping.

1. The bigger the pressure is, the later the slipping occurs.
2. For a given structure, there is no damping limit since bigger clamping pressure can surely yield a higher damping capacity limit.
3. For a given clamping pressure, the bigger the amplitude is, the more damped the structure becomes.
4. The increase in damping capacity is not proportional to vibration amplitude, as the damping ratio converges asymptotically to a limited value under big amplitude.
5. For small amplitude (0.5 mm to 1 mm), there exists a zone where smaller pressure may produce bigger damping.
6. For big amplitudes (1 mm to 3 mm), bigger pressure does produce more damping.

The asymptotic behavior of damping ratio can be attributed to the fact that dissipated and stocked energy are both quadratic functions of mode amplitude, which is different from the first-order damping whose dissipated energy is a linear function of amplitude.

2.4.4.2 Influence of coefficient of friction

As is already studied in the first-order damping mechanism, the coefficient of friction has the same influence as clamping pressure. The damping coefficient approaches to saturation at big amplitude of transverse deflection, and there exists always a zone where smaller coefficient of friction can yield bigger damping.

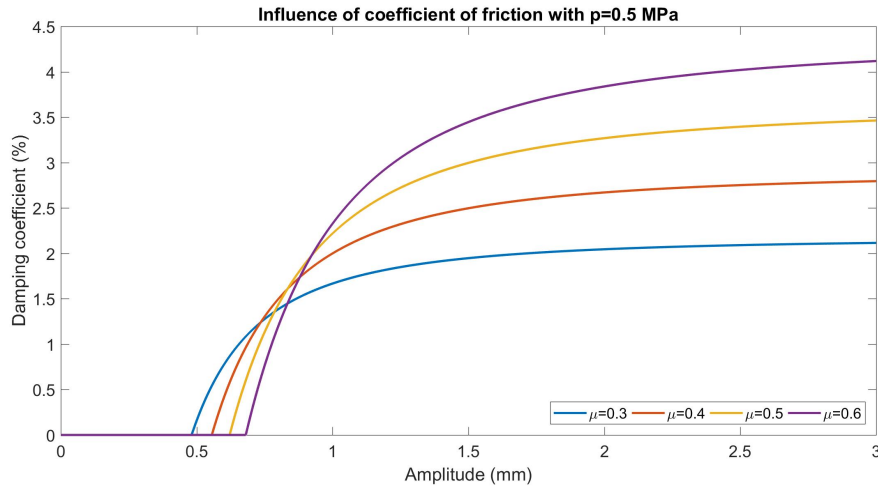


Figure 2.32: Influence of coefficient of friction on damping ratio

2.4.4.3 Influence of contact area

The contact area is adjustable by varying the parameter S in equation 2.77. Four lengths are used to give four different contact areas. Bigger area is shown to be able to postpone the occurrence of slipping and bring more damping to the structure for a given contact property in condition of big amplitude. Similar to the coefficient of friction and clamping pressure, there is an amplitude interval (0.5 mm to 1mm in the current case) where bigger contact area may result in smaller damping, even though the slipping is already present during the cyclic movement.

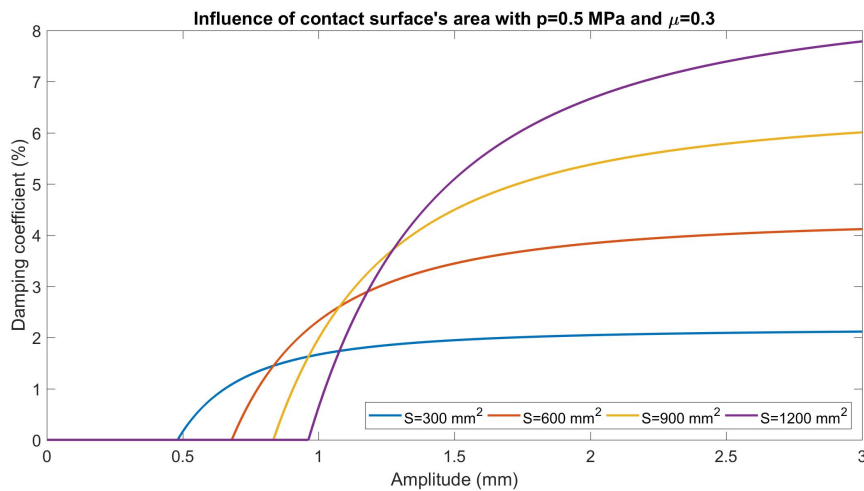


Figure 2.33: Influence of contact area on damping ratio

2.5 Conclusion

Distinct from viscous damping which is present throughout the entire structure and proportional to speed, friction damping is localized and considered to be proportional to displacement. Due to the fact that in assembled structures frictional damping is 10 to 100 times bigger than viscous damping, it is not only important to have a qualitative view of damping evolution pattern, but also an accurate estimation of energy dissipation. For these purposes, three simplified academic models constituted of beam and friction contact zone are proposed in this chapter, a quasi-static approach is adopted in the modelization.

Two types of damping patterns are identified: first-order damping and second order damping. The order of damping is determined by the order of modal amplitude in the expression for energy dissipation. The relationship between modal amplitude and energy dissipation is linear in first order damping models, whose characteristics can be revealed by sandwich beam model and rotational joint model. The main characteristic of first order damping is that there exists a maximum damping capacity that the structure cannot surpass, whatever optimization method is used. It is an intrinsic property of the structure. Once the maximum damping is reached, an increase in amplitude will result in a decrease in damping. In a similar way, the second order damping signifies that amplitude is quadratic in energy dissipation expression. In this case, the structure doesn't possess maxima in the amplitude range. The structure just becomes more damped with an increase in modal amplitude. Its evolution follows asymptotic curve and saturates under big modal amplitude.

The main influencing parameters in friction damping are coefficient of friction, clamping pressure and contact area. The way they modify damping can be different in first and second order models, but they share some common points. Clamping pressure and coefficient of friction comes always in a product, an amplifying/minifying ratio multiplied to either of them will give the same result. An increase in contact area will always postpone the occurrence of slipping and increase energy dissipation under big modal amplitude. Other influencing parameters like thickness ratio and kinematic boundary condition are also analyzed, but are restrained to the sandwich beam model and are conducted with finite element method in the software ABAQUSTM. It can be deduced that all measures facilitate interface slipping will result in an increase in damping capacity potential.

Friction damping is shown to be complex in terms of its sensitivity to geometry, friction properties as well as its dependency on modal amplitude. It can be for the moment classified into two categories, but there may exist other damping patterns. The phenomenological study in the current chapter sheds light on damping forming mechanism and shows the possibility of damping optimization. The next chapter will deal with the design of an experiment installation as well as the results obtained

to verify the exactitude of the theory proposed.

Semi-analytical methods of damping modelization

Contents

2.1	Introduction	29
2.2	First-order interface damping in sandwich beam	30
2.2.1	Analytical modelization	30
2.2.2	Analytical parametric studies	37
2.2.3	Numerical parametric studies	41
2.3	First-order boundary damping in rotational joint	49
2.3.1	Analytical modelization	49
2.3.2	Analytical parametric studies	52
2.4	Second-order boundary damping in von Kármán plate	54
2.4.1	Geometric derivation of simplified Green strain	54
2.4.2	Analytical modelization	55
2.4.3	Analytical expression of slipping boundary's trajectory	59
2.4.4	Analytical parametric studies	63
2.5	Conclusion	66

3.1 Introduction

The analytical and numerical results presented in the previous chapter show that friction damping is generally a function of modal amplitude. According to the order of displacement in the expression of energy dissipation, frictional damping can be categorized into first-order damping and second-order damping. Determined by the intrinsic characteristic of the first-order sandwich model used in the study, in which the relative displacement is a function of cross section's rotation, the first-order damping is shown to have a limited damping capacity and there exists an optimized modal amplitude at which the assembled structure can reach its most damped state. Unlike the first-order damping, the second-order damping is induced by second-order bending strain and doesn't have a maximum damping capacity in the modal amplitude range. The damping ratio increases with the deformation level, but the growth rate is decreasing which makes it similar to an asymptote.

The current chapter will continue to deepen the understanding of the two damping categories, notably the first-order damping in sandwich plate and the second-order damping in von Kármán plate. However the study will be conducted in a more subtle manner based on a semi-analytical method. In order to overcome the limitations of the analytical method which can only deal with one-dimensional structures, finite element method is employed in complement with finite difference method to enable a two-dimensional analysis of the interface slipping.

This chapter will firstly deal with the second-order damping mechanism in von Kármán plate with one slipping boundary. The notion of fictive force field will be firstly demonstrated, which enables a facilitated solution of the discretized von Kármán plate's formulation. Based on the quasi-static numerical methods that will be developed, the second-order damping phenomenon can be revealed, the hardening/softening effect induced by in-plane stress field as well as the mode shape change due to internal force coupling can also be analyzed. The second part will explain the mechanism of partial slipping in the sandwich plate model from an in-plane point of view. The results will show that the presence of partial slipping can modify the structure's damping property, if compared to the analytical model which assumes an immediate total slipping on the contact surface. In the current chapter, the comparison with analytical models is conducted in parallel with the proposed numerical method for the purpose of verification.

3.2 Damping induced by second-order bending strain in von Kármán plate

3.2.1 Formulation of fictive force field

Apart from laminated beams, there are also a large number of structures in the form of plate whose tangential displacement in the joint is induced by transverse deflection, as analytically demonstrated in section 2.4.1. The second-order strain ε''_x , ε''_y and ε''_{xy} induced by spacial derivatives of displacement w can be regarded as an external body force field applied to the structure if substituted into the dynamic equilibrium equation. This new mechanical view of plate bending is presented in the demonstration below.

The components of the three-dimensional Lagrangian Green strain tensor are defined as

$$E_{ij} = \frac{1}{2} \left(\frac{\partial u_i}{\partial x_j} + \frac{\partial u_j}{\partial x_i} + \frac{\partial u_k}{\partial x_i} \frac{\partial u_k}{\partial x_j} \right), \quad k = 1, 2, 3. \quad (3.1)$$

The von Kármán plate theory takes into account the non-linear second-order strain components that are contributed by transverse deflection, the contributions from the in-plane directions x and y are neglected and the index k is only valued at 3. The strains can thus be expressed as

3.2. Damping induced by second-order bending strain in von Kármán plate 71

$$\varepsilon_x = \frac{\partial u}{\partial x} + z \frac{\partial^2 w}{\partial x^2} + \frac{1}{2} \left(\frac{\partial w}{\partial x} \right)^2 \quad (3.2a)$$

$$\varepsilon_y = \frac{\partial v}{\partial y} + z \frac{\partial^2 w}{\partial y^2} + \frac{1}{2} \left(\frac{\partial w}{\partial y} \right)^2 \quad (3.2b)$$

$$\varepsilon_{xy} = \frac{1}{2} \left(\frac{\partial u}{\partial y} + \frac{\partial v}{\partial x} + z \frac{\partial^2 w}{\partial x \partial y} + \frac{\partial w}{\partial x} \frac{\partial w}{\partial y} \right). \quad (3.2c)$$

By using Hooke's law which establishes the relationship between stresses and strains

$$\sigma_{ij} = \frac{E}{1 - \nu^2} [(1 - \nu)\varepsilon_{ij} + \nu\varepsilon_{kk}\delta_{ij}], \quad \delta_{ij} : \text{Kronecker } \delta \quad (3.3)$$

and substitute the strain components into equation 3.3, the in-plane stresses can be calculated by firstly integrating the stress components along the thickness of the plate and secondly averaging them by N_{ij}/h . The in-plane stress components are expressed as

$$\sigma_x = \frac{E}{1 - \nu^2} \left\{ \left[\frac{\partial u}{\partial x} + \frac{1}{2} \left(\frac{\partial w}{\partial x} \right)^2 \right] + \nu \left[\frac{\partial v}{\partial y} + \frac{1}{2} \left(\frac{\partial w}{\partial y} \right)^2 \right] \right\} \quad (3.4a)$$

$$\sigma_y = \frac{E}{1 - \nu^2} \left\{ \left[\frac{\partial v}{\partial y} + \frac{1}{2} \left(\frac{\partial w}{\partial y} \right)^2 \right] + \nu \left[\frac{\partial u}{\partial x} + \frac{1}{2} \left(\frac{\partial w}{\partial x} \right)^2 \right] \right\} \quad (3.4b)$$

$$\sigma_{xy} = \frac{E}{2(1 + \nu)} \left(\frac{\partial u}{\partial y} + \frac{\partial v}{\partial x} + \frac{\partial w}{\partial x} \frac{\partial w}{\partial y} \right). \quad (3.4c)$$

These components can be divided into two parts: one part is a function of in-plane displacements u and v and another is a function of transverse displacement w .

Substituting the stress components into the infinitesimal equilibrium equation

$$\sigma_{ij,j} + f_i = 0, \quad (3.5)$$

the local equilibrium equation in terms of displacements u , v and w can be obtained. Take the equilibrium in x direction as an example

$$\begin{aligned} \frac{E}{1 - \nu^2} \frac{\partial}{\partial x} \left\{ \left[\frac{\partial u}{\partial x} + \frac{1}{2} \left(\frac{\partial w}{\partial x} \right)^2 \right] + \nu \left[\frac{\partial v}{\partial y} + \frac{1}{2} \left(\frac{\partial w}{\partial y} \right)^2 \right] \right\} \\ + \frac{E}{2(1 + \nu)} \frac{\partial}{\partial y} \left(\frac{\partial u}{\partial y} + \frac{\partial v}{\partial x} + \frac{\partial w}{\partial x} \frac{\partial w}{\partial y} \right) = 0. \end{aligned} \quad (3.6)$$

Separate the components induced by transverse deflection from the those related to in-plane displacements

$$\begin{aligned} & \frac{E}{1-\nu^2} \frac{\partial}{\partial x} \left(\frac{\partial u}{\partial x} + \nu \frac{\partial v}{\partial y} \right) + \frac{E}{2(1+\nu)} \frac{\partial}{\partial y} \left(\frac{\partial u}{\partial y} + \frac{\partial v}{\partial x} \right) \\ & + \frac{E}{1-\nu^2} \frac{\partial}{\partial x} \left[\frac{1}{2} \left(\frac{\partial w}{\partial x} \right)^2 + \frac{\nu}{2} \left(\frac{\partial w}{\partial y} \right)^2 \right] + \frac{E}{2(1+\nu)} \frac{\partial}{\partial y} \left(\frac{\partial w}{\partial x} \frac{\partial w}{\partial y} \right) = 0. \end{aligned} \quad (3.7)$$

Since the body force f_i doesn't exist, the current problem can be regarded as being transformed into a plane stress equilibrium problem expressed in first order linear strains, the excitation results from a fictive body force field which is induced by transverse deflection. The fictive body force in the x and y direction can thus be written as

$$f_x = \frac{E}{1-\nu^2} \left(\frac{\partial w}{\partial x} \frac{\partial^2 w}{\partial x^2} + \nu \frac{\partial w}{\partial y} \frac{\partial^2 w}{\partial x \partial y} \right) + \frac{E}{2(1+\nu)} \left(\frac{\partial^2 w}{\partial x \partial y} \frac{\partial w}{\partial y} + \frac{\partial w}{\partial x} \frac{\partial^2 w}{\partial y^2} \right) \quad (3.8a)$$

$$f_y = \frac{E}{1-\nu^2} \left(\frac{\partial w}{\partial y} \frac{\partial^2 w}{\partial y^2} + \nu \frac{\partial w}{\partial x} \frac{\partial^2 w}{\partial x \partial y} \right) + \frac{E}{2(1+\nu)} \left(\frac{\partial^2 w}{\partial x \partial y} \frac{\partial w}{\partial x} + \frac{\partial w}{\partial y} \frac{\partial^2 w}{\partial x^2} \right). \quad (3.8b)$$

The fictive body force field is a function of transverse displacement's spatial first and second derivatives and they can be calculated by finite difference method. This fictive field enables the solution of in-plane displacements u and v with a given w which originates from a known mode shape. Once u and v are known, they can be substituted in equation 3.4 to yield the superimposed in-plane stress field.

3.2.2 Discrete method of derivatives' evaluation

The fictive body force is a continuous 2-dimensional field. However in finite element method, the only known parameter is the nodal transverse displacement w . In order to calculate the equivalent force vector of every node in the continuous field, it is necessary to evaluate the spatial partial derivatives in equation 3.8. Once these values are known, the equivalent force vector can be determined by integration with Gauss points whose values are interpolated from nodal values. The mesh used for finite element method is illustrated in figure below. The plate is of length 600 mm and width 400 mm. Each element is a square of side length 50 mm, so that there are in total 12 elements in the x direction and 8 elements in the y direction.

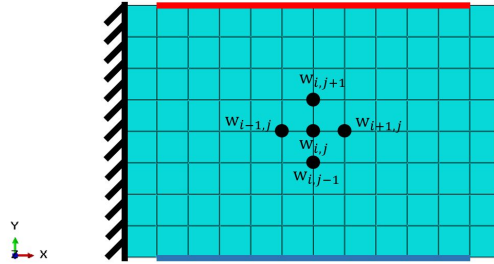


Figure 3.1: Mesh for finite element method and derivatives calculation

3.2. Damping induced by second-order bending strain in von Kármán plate 73

The left boundary of the plate is encastered and the right boundary can be regarded as a pin but with blocked rotation to the y axis, it is due to the fact that the clamp can limit the rotation of the nodes under pressure. The spatial derivatives can be expressed by neighboring nodal values with finite difference schemes.

The nodal derivatives with different boundary conditions can be expressed by the schemes in table below. The schemes for second order derivatives are presented in Appendix A. The upper and lower free nodes are respectively designated by red and blue line, the nodes under friction contact are marked by yellow line.

	$\frac{\partial w}{\partial x}$	$\frac{\partial w}{\partial y}$
Encastre	0	0
Friction	0	0
Upper free nodes	$\frac{w_{i+1,j} - w_{i-1,j}}{2dx}$	$\frac{w_{i,j} - w_{i,j-1}}{dy}$
Lower free nodes	$\frac{w_{i+1,j} - w_{i-1,j}}{2dx}$	$\frac{w_{i,j+1} - w_{i,j}}{dy}$
Other nodes	$\frac{w_{i+1,j} - w_{i-1,j}}{2dx}$	$\frac{w_{i,j+1} - w_{i,j-1}}{2dy}$

Table 3.1: First derivatives schemes

To test the precision of the finite difference schemes, the nodal derivatives are evaluated on an analytical imposed mode shape $w(x)$ which is only in terms of x , i.e. there is no curvature in the y direction.

$$w(x) = \frac{1}{2} \left(\cos \frac{2\pi}{L} x - 1 \right). \quad (3.9)$$

The derivatives obtained by finite difference schemes are compared to the analytical first and second derivatives with the imposed form, who are evaluated at the center of each element.

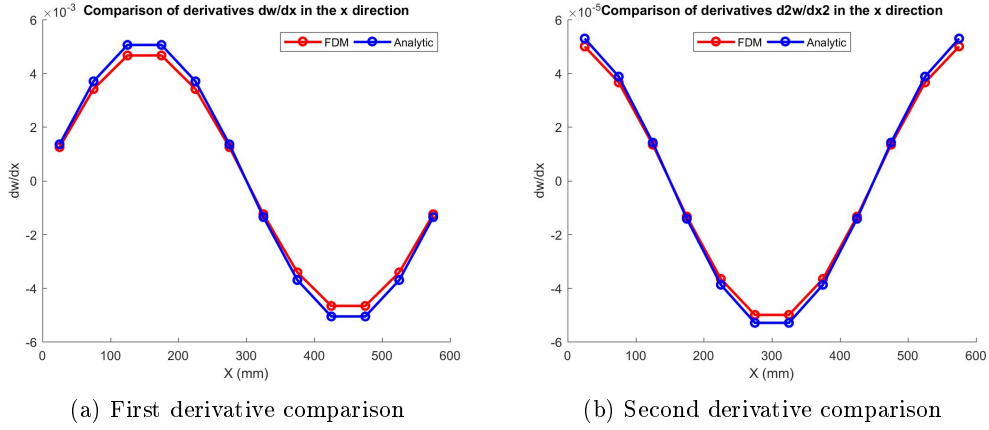


Figure 3.2: Derivatives comparison between FDM and analytical expression

The first and second derivative comparisons show that finite difference schemes adopted in the current study are able to provide a precise evaluation of the spatial derivatives required in the fictive force field calculation.

3.2.3 Friction properties

The contact property used in the current study is a two-dimensional Coulomb's friction law. The shear stress components on the contact surface are designated as τ_x and τ_y and normal stress as σ_n . When the boundary is in sticking phase, the static frictional force is in the opposite direction of reaction force. However once the shear stress resultant is bigger than the maximum frictional stress limit, the slipping occurs and the direction of frictional force is in the opposite direction of the relative movement speed. The difficulty in the integration of Coulomb's law in dynamic calculation is that the friction force's direction is not only a function of current step's stress state, but also of relative displacement.

In case of sticking, the shear stress resultant is inferior to the maximum shear stress that the contact friction can provide.

$$(\tau_x^2 + \tau_y^2)^{\frac{1}{2}} < \mu\sigma_n. \quad (3.10)$$

Once the shear stress exceeds the friction limit, the stress resultant is saturated to the value of maximum shear stress $\mu\sigma_n$ and the friction's direction is determined by the direction of the relative displacement's speed. The speed can be replaced by infinitesimal displacement increment du/dt and dv/dt . As the frictional force is always in the opposite direction of speed, a negative sign is added to the component du and dv .

3.2. Damping induced by second-order bending strain in von Kármán plate 75

$$(\tau_x^2 + \tau_y^2)^{\frac{1}{2}} = \mu\sigma_n \quad (3.11a)$$

$$\tau_x = \mu\sigma_n \cdot \frac{-du}{\sqrt{du^2 + dv^2}} \quad (3.11b)$$

$$\tau_y = \mu\sigma_n \cdot \frac{-dv}{\sqrt{du^2 + dv^2}}. \quad (3.11c)$$

The frictional property at the contact interface can be combined to the fictive force field to establish the in-plane equilibrium, from which the slipping displacement can be cumulated to calculate the total energy dissipation during one cycle in the periodic movement. The next section will present the solution procedure which is based on Ritz-Galerkin method.

3.2.4 Solution procedure

The in-plane problem can be solved by finite element method. Plane stress elements are used for discretization. By using the shape function of iso-parametric 4-node element, the equivalent nodal forces of a given element m can be expressed as

$$(\mathbf{f}_m) = \int_{-1}^1 \int_{-1}^1 [\mathbf{R}]^T \begin{pmatrix} f_x \\ f_y \end{pmatrix} h |\mathbf{J}| dsdt. \quad (3.12)$$

Where $[\mathbf{R}]$ is a (8×2) matrix of shape functions, $|\mathbf{J}|$ is the determinant of Jacobian matrix and h is the thickness of the plate. The body force f_x and f_y are evaluated at 4 Gauss points in each element, the integral in the local coordinate system is thus transformed into a sum of Gauss point values. The global equilibrium equation can be written as

$$\begin{bmatrix} \mathbf{K}_{II} & \mathbf{K}_{IB} \\ \mathbf{K}_{BI} & \mathbf{K}_{BB} \end{bmatrix} \begin{pmatrix} \mathbf{U}_I \\ \mathbf{U}_B \end{pmatrix} = \begin{pmatrix} \mathbf{F}_I \\ \mathbf{F}_B \end{pmatrix} + \begin{pmatrix} \mathbf{0} \\ \mathbf{N}_B \end{pmatrix}, \quad (3.13)$$

where index I and B corresponds respectively to inner and boundary DOFs. The vector \mathbf{F} , assembled from the equivalent nodal forces (\mathbf{f}_m) of each element, contains the discretized fictive body force field. The vector \mathbf{N} is the frictional force at the boundary which respects the friction law presented in the previous section. Since there is no frictional force on inner DOFs, the corresponding components in \mathbf{N} are $\mathbf{0}$, and the model can be condensed to boundary DOFs, which results in a smaller model with less DOFs. The condensed form is

$$[\mathbf{K}_c](\mathbf{U}_B) = (\mathbf{F}_c) + (\mathbf{N}_B). \quad (3.14)$$

where the condensed stiffness matrix $[\mathbf{K}_c]$ and fictive force vector (\mathbf{F}_c) are respectively written as

$$[\mathbf{K}_c] = [\mathbf{K}_{BB}] - [\mathbf{K}_{BI}][\mathbf{K}_{II}]^{-1}[\mathbf{K}_{IB}] \quad (3.15a)$$

$$(\mathbf{F}_c) = (\mathbf{F}_B) - [\mathbf{K}_{BI}][\mathbf{K}_{II}]^{-1}(\mathbf{F}_I). \quad (3.15b)$$

At the initialization step of the calculation, all boundary DOFs who have potential to slip are blocked. The trial reaction friction forces (\mathbf{N}_B) of step $t + 1$ are evaluated from the previous step's displacement.

$$w = q\phi(x, y). \quad (3.16)$$

According to the single mode shape representation in equation 3.16 and the expressions of fictive force field given in equation 3.8, the fictive force is a quadratic function of modal amplitude $f = f(q^2)$, so that the boundary friction force vector at step $t + 1$ can be written as

$$(\mathbf{N}_B)_{t+1} = [\mathbf{K}_c](\mathbf{U}_B)_t - q_{t+1}^2(\mathbf{F}_c), \quad (3.17)$$

where (\mathbf{F}_c) is the condensed reference body force field obtained from the normalized mode shape $\phi(x, y)$.

The obtained $(\mathbf{N}_B)_{t+1}$ should satisfy the sticking-slipping criteria in equation 3.10 and 3.11. The updated friction force $(\mathbf{N}_B)_{t+1}^{new}$ can then be carried into the equilibrium of step $t + 1$ to calculate the real boundary displacement

$$(\mathbf{U}_B)_{t+1} = [\mathbf{K}_c]^{-1} (q_{t+1}^2(\mathbf{F}_c) + (\mathbf{N}_B)_{t+1}^{new}). \quad (3.18)$$

The displacement of other DOFs at each step t can be obtained by reversing the condensation procedure with the known boundary displacement

$$(\mathbf{U}_I)_t = [\mathbf{K}_{II}]^{-1} (q_t^2(\mathbf{F}_I)_t - [\mathbf{K}_{IB}](\mathbf{U}_B)_t). \quad (3.19)$$

Since u and v are all known, the superimposed in-plane stress field can thus be obtained with equation 3.4 and the solution of dynamic von Kármán equation 3.20 is possible.

$$\rho \frac{\partial^2 w}{\partial t^2} + D\Delta^4 w - \left(N_x \frac{\partial^2 w}{\partial x^2} + 2N_{xy} \frac{\partial^2 w}{\partial x \partial y} + N_y \frac{\partial^2 w}{\partial y^2} \right) = f(x, y, t) \quad (3.20)$$

By applying the notion of modal synthesis, the transverse deflection of the plate can be approximated by a linear combination of n first normal modes $w = \sum_{i=1}^n q_i \phi_i$. The normal modes are a solution of eigenvalue problem defined in linear plate theory

$$D\nabla^4 \phi_i = \omega_i^2 \rho \phi_i. \quad (3.21)$$

Since the linear combination of ϕ_i is only an approximation, the error expression of equation 3.20 can be written as

$$e = \sum_{i=1}^n \frac{d^2 q_i}{dt^2} \rho \phi_i + \sum_{i=1}^n q_i D\nabla^4 \phi_i - \sum_{i=1}^n q_i R(N, \phi_i) - f(x, y, t) \quad (3.22)$$

3.2. Damping induced by second-order bending strain in von Kármán plate 7

where the non-linear term is abbreviated as $R(N, \phi_i)$ where

$$R(N_i, \phi_i) = N_x \frac{\partial^2 \phi_i}{\partial x^2} + 2N_{xy} \frac{\partial^2 \phi_i}{\partial x \partial y} + N_y \frac{\partial^2 \phi_i}{\partial y^2}. \quad (3.23)$$

N_i is the corresponding internal force of mode shape ϕ_i .

For the moment we are only interested in mono-mode response of the structure excited in the neighborhood of its resonance frequency ω_i , therefore the mode shape ϕ_i is dominant in the response and we consider in the first place that the shape of mode i doesn't change with amplitude. Thus only the mode shape ϕ_i is retained in equation 3.22. The Ritz-Galerkin method can be used to minimize the error function e

$$\int_v \frac{d^2 q}{dt^2} \rho \phi_i \phi_i dv + \int_v q D \nabla^4 \phi_i \phi_i dv - \int_v q R(N, \phi_i) \phi_i dv = \int_v f(x, y, t) \phi_i dv. \quad (3.24)$$

Since the mode shape ϕ_i is normalized in the way

$$\int_v \rho \phi_i \phi_i dv = 1, \quad (3.25)$$

the error function can be written in scalar form as

$$\frac{d^2 q}{dt^2} + \omega_i^2 q - \psi(t) q = f \quad (3.26)$$

where

$$\psi(t) = \int_v R(N, \phi_i) \phi_i dv. \quad (3.27)$$

The N_{ix} , N_{iy} and N_{ixy} are valued at the center of each element m for mode i and are assumed to be homogeneous within the given element. The spatial first and second derivatives are obtained by finite difference method. The discretized expression of ψ_{ii} takes the form

$$\psi_{ii}(t) = \sum_{m=1}^N \left(N_x^m \frac{\partial^2 \phi_i^m}{\partial x^2} + 2N_{xy}^m \frac{\partial^2 \phi_i^m}{\partial x \partial y} + N_y^m \frac{\partial^2 \phi_i^m}{\partial y^2} \right) \phi_i^m S^m \quad (3.28)$$

with S^m the surface area of element m , N the total number of elements.

The steady state solution for q under harmonic excitation of angular frequency ω is assumed in the form of a harmonic function of time. The excitation force's phase is taken as reference, and the phase angle is represented by a complex number \hat{q} .

$$q = \hat{q} e^{i\omega t}, \quad f = f e^{i\omega t} \quad (3.29)$$

Equation 3.26 becomes

$$-\omega^2 \hat{q} e^{i\omega t} + \omega_i^2 \hat{q} e^{i\omega t} - \psi_{ii}(t) \hat{q} e^{i\omega t} = f e^{i\omega t}. \quad (3.30)$$

By equating the imaginary part of equation 3.30

$$-\omega^2 \hat{q} \sin \omega t + \omega_i^2 \hat{q} \sin \omega t - \psi_{ii}(t) \hat{q} \sin \omega t = f \sin \omega t. \quad (3.31)$$

Since $\psi(t)$ is also a function of time t , the $\sin \omega t$ cannot be eliminated from equation 3.31 directly. The use of Harmonic Balance Method requires decomposition of the term $\psi(t) \sin \omega t$ into two harmonic components,

$$-\psi_{ii}(t) \sin \omega t = \psi_{iic} \cos \omega t + \psi_{iis} \sin \omega t, \quad (3.32)$$

where

$$\theta = \omega t \quad (3.33a)$$

$$\psi_{iic} = \frac{1}{\pi} \int_0^{2\pi} -\psi_{ii}(t) \sin \theta \cos \theta d\theta = \frac{1}{2\pi} \int_0^{2\pi} -\psi_{ii}(t) \sin 2\theta d\theta \quad (3.33b)$$

$$\psi_{iis} = \frac{1}{\pi} \int_0^{2\pi} -\psi_{ii}(t) \sin \theta \sin \theta d\theta = \frac{1}{2\pi} \int_0^{2\pi} -\psi_{ii}(t) (1 - \cos 2\theta) d\theta \quad (3.33c)$$

In this way equation 3.31 can be written as

$$-\omega^2 \hat{q} + \omega_i^2 \hat{q} \sin \omega t + \hat{q} \psi_{iic} \cos \omega t + \hat{q} \psi_{iis} \sin \omega t = f \sin \omega t \quad (3.34)$$

In order to have the same harmonic base, the rotational vector \hat{q} with $\cos \omega t$ has to be multiplied by i so as to rotate 90 degrees.

$$(-\omega^2 + \omega_i^2 + i\psi_c + \psi_s) \hat{q} \sin \omega t = f \sin \omega t \quad (3.35a)$$

$$[-\omega^2 + \omega_i^2 (1 + \lambda + i\eta)] \hat{q} = f \quad (3.35b)$$

where

$$\eta = \frac{\psi_c}{\omega_i^2}, \quad \lambda = \frac{\psi_s}{\omega_i^2} \quad (3.36)$$

The structure's hardening is proportional to the coefficient λ and damping is represented by η . The structural damping factor can be determined with greater precision by using the ratio between energy dissipation per cycle and maximum stocked elastic energy [52]. In the following calculation, the damping factor can also be defined as a function of energy dissipation.

$$\eta = \frac{1}{2\pi} \frac{\Delta W}{E_{max}} \quad (3.37)$$

with

3.2. Damping induced by second-order bending strain in von Kármán plate

$$\Delta W = \sum_{t=2}^T |(\mathbf{U}_B^t - \mathbf{U}_B^{t-1})^T (\mathbf{N}_B^t)|, \quad E_{max} = \frac{1}{2} |\hat{q}|^2 \omega_i^2. \quad (3.38)$$

The solution of equation 3.35 can be achieved by applying an iterative Newton method with an initial q as static displacement f/w_i^2 .

3.2.5 Analytical solution of clamped-clamped plate

One of the main features in the von Kármán plate theory is its capacity to reveal the hardening/softening effect due to internal stress field. This phenomenon can be demonstrated by analytical method in the case of clamped-clamped plate, as illustrated in figure 3.3.

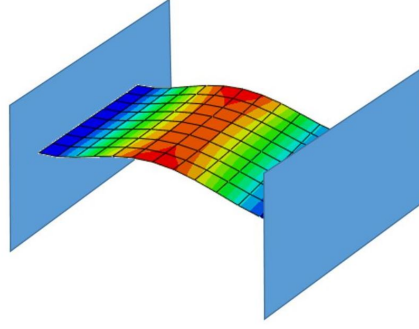


Figure 3.3: Clamped-clamped plate model

The mode shape of the first resonance is assumed in the form of cosine function, as expressed in equation 3.9, however due to the requirement that the mode shape is normalized to the mass, a coefficient k should be multiplied to equation 3.9.

$$\int_0^L \rho \left[\frac{k}{2} (\cos \alpha x - 1) \right]^2 dx = 1 \quad \implies \quad k = \sqrt{\frac{8}{3\rho L}} = \sqrt{\frac{8}{3m}}. \quad (3.39)$$

According to the expression 2.67 of constant internal force field in case of clamped-clamped boundary condition, the in-plane force per unit of width is

$$N_i = Eh \frac{q^2 \alpha^2}{16} \cdot \left(\sqrt{\frac{8}{3m}} \right)^2 = Eh \frac{q^2 \alpha^2}{6m}. \quad (3.40)$$

The non-linear term $R(N_i, \phi_i)$ in equation 3.23 can be written as

$$R(N_i, \phi_i) = Eh \frac{q^2 \alpha^2}{6m} \cdot \sqrt{\frac{8}{3m}} \cdot \frac{\partial}{\partial x^2} \left[\frac{1}{2} (\cos \alpha x - 1) \right] = -Eh \frac{q^2 \alpha^4}{6m} \cdot \sqrt{\frac{2}{3m}} \cos \alpha x. \quad (3.41)$$

As indicated in the solution procedure based on Ritz-Galerkin method, the non-linear term is weighted on the entire calculation domain with the normalized mode shape, as expressed in equation 3.27.

$$\psi_{ii}(R(N_i), \phi_i) = -Eh \frac{q^2 \alpha^4}{6m} \cdot \int_0^L \sqrt{\frac{2}{3m}} \cos \alpha x \cdot \frac{1}{2} \sqrt{\frac{8}{3m}} (\cos \alpha x - 1) b dx = \frac{-EbhLq^2 \alpha^4}{18m^2} \quad (3.42)$$

where b is the width of the plate. The non-linear term ψ_{ii} in this case is a negative-definite value.

It is assumed that the modal amplitude varies in the sinusoidal way $q = q_m \sin \theta$. The hardening factor λ and the damping ratio μ can thus be written as

$$\lambda = \frac{1}{2\pi\omega_i^2} \cdot \frac{Ebhaq_m^2 \alpha^4 L}{18m^2} \int_0^{2\pi} \sin^2 \theta (1 - \cos 2\theta) d\theta = \frac{Ebhaq_m^2 \alpha^4 L}{24\omega_i^2 m^2} \quad (3.43a)$$

$$\mu = \frac{1}{2\pi\omega_i^2} \cdot \frac{Ebhaq_m^2 \alpha^4 L}{18m^2} \int_0^{2\pi} \sin^2 \theta \sin 2\theta d\theta = 0 \quad (3.43b)$$

The clamped-clamped boundary condition infers that there is no energy dissipation, which can be confirmed by the zero damping ratio. The hardening factor is shown to be a quadratic function of modal amplitude and is positive-definite, which means that the plate is always under hardening effect.

3.2.6 Analytical solution of clamped-slipping plate

In the case of slipping, the internal force N_i is saturated to $\mu pS/b$, where S is the total contact surface and b is the width of the plate. Here we consider that the clamped side slips immediately with the imposed modal amplitude, so there is no sticking phase. The non-linear term $R(N_i, \phi_i)$ in this condition takes the following form

$$R(N_i, \phi_i) = \frac{\mu pS}{b} \frac{\partial}{\partial^2 x} \left[\sqrt{\frac{2}{3m}} (\cos \alpha x - 1) \right] = -\frac{\mu pS}{b} \sqrt{\frac{2}{3m}} \cdot \alpha^2 \cos \alpha x \quad (3.44)$$

The updated direct controlling parameter ψ_{ii} is thus written as

$$\begin{aligned} \psi_{ii}(R(N_i), \phi_i) &= \int_0^L R(N_i, \phi_i) \phi_i b dx = \int_0^L \frac{\mu pS}{b} \sqrt{\frac{2}{3m}} (-\alpha^2 \cos \alpha x) \sqrt{\frac{2}{3m}} (\cos \alpha x - 1) b dx \\ &= -\frac{\mu pS \alpha^2 L}{3m}. \end{aligned} \quad (3.45)$$

It is worth noting that the internal force takes alternative directions during one vibration cycle, that's to say

3.2. Damping induced by second-order bending strain in von Kármán plate 81

$$\psi_{ii} = \begin{cases} -\frac{\mu p S \alpha^2 L}{3m} & \text{if } 0 < q \leq \frac{\pi}{2} \\ \frac{\mu p S \alpha^2 L}{3m} & \text{if } \frac{\pi}{2} < q \leq \pi \\ -\frac{\mu p S \alpha^2 L}{3m} & \text{if } \pi < q \leq \frac{3\pi}{2} \\ \frac{\mu p S \alpha^2 L}{3m} & \text{if } \frac{3\pi}{2} < q \leq 2\pi. \end{cases} \quad (3.46)$$

In this case, the calculation of hardening factor and damping ratio is a piece-wise function.

$$\begin{aligned} \lambda &= \frac{1}{2\pi\omega_i^2} \int_0^{2\pi} (-\psi_{ii})(1 - \cos 2\theta) d\theta \\ &= \int_0^{\pi/2} -\frac{\mu p S \alpha^2 L}{3m} (1 - \cos 2\theta) d\theta + \int_{\pi/2}^{\pi} \frac{\mu p S \alpha^2 L}{3m} (1 - \cos 2\theta) d\theta \\ &+ \int_{\pi}^{3\pi/2} -\frac{\mu p S \alpha^2 L}{3m} (1 - \cos 2\theta) d\theta + \int_{3\pi/2}^{2\pi} \frac{\mu p S \alpha^2 L}{3m} (1 - \cos 2\theta) d\theta \\ &= 0, \end{aligned} \quad (3.47)$$

$$\begin{aligned} \mu &= \frac{1}{2\pi\omega_i^2} \int_0^{2\pi} (-\psi_{ii}) \sin 2\theta d\theta \\ &= \int_0^{\pi/2} -\frac{\mu p S \alpha^2 L}{3m} \sin 2\theta d\theta + \int_{\pi/2}^{\pi} \frac{\mu p S \alpha^2 L}{3m} \sin 2\theta d\theta \\ &+ \int_{\pi}^{3\pi/2} -\frac{\mu p S \alpha^2 L}{3m} \sin 2\theta d\theta + \int_{3\pi/2}^{2\pi} \frac{\mu p S \alpha^2 L}{3m} \sin 2\theta d\theta \\ &= \frac{2\mu p S \alpha^2 L}{3\pi\omega_i^2 m}. \end{aligned} \quad (3.48)$$

The zero hardening factor indicates that under immediate slipping boundary condition, the hardening and softening effect are counteracted in one cycle, so that the average stiffness doesn't change. However the damping effect can be cumulated in every quarter-cycle and results in a constant damping ratio. Contrary to the intuition that the damping ratio is a function of modal amplitude, the current result is due to the constant internal force hypothesis that is adopted before the derivation.

3.2.7 Numerical solution of clamped-clamped plate

A rectangular plate of uniform thickness 2 mm is chosen to illustrate the hardening effect as well as the damping characteristics in von Kármán plate. The length is 600 mm and the width is 400 mm. The plate is clamped at the boundary $x = 0$ and $x = 600$ mm and is excited by a cyclic force f at its first resonance frequency, which is 30.860 Hz. Since the first mode is dominant in the shape composition, according

to the theory of single mode method, only the first linear mode is retained for the calculation of fictive force field. The clamped boundary condition can be assimilated to an infinite coefficient of friction.

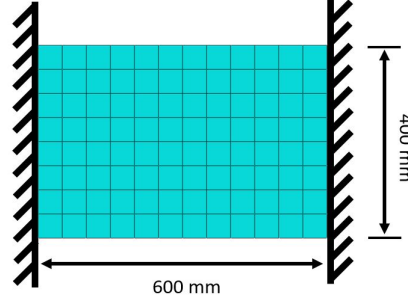


Figure 3.4: Finite element model of clamped-clamped plate

In order to verify the exactitude of the proposed numerical method, a comparison with the analytical method is necessary. Since the analytical method can only deal with simple expressions, the imposed mode shape takes the normalized form

$$\phi_i(x, y) = q \sqrt{\frac{2}{3m}} (\cos \alpha x - 1), \quad (3.49)$$

where q the modal amplitude, m the mass of the plate, $\alpha = 2\pi/L$.

The analytical mode shape's in-plane fictive force field obtained from equation 3.8 is presented in figure 3.5. The DOFs on the middle line $x = 300$ mm is in equilibrium from the left and the right force field. However the DOFs on the line $x = 150$ mm and $x = 450$ mm are in compression. The non-dependence of the y direction results in a field that is exactly parallel to the x axis. The in-plane fictive force field engenders a non-uniform stress field in the plate, which generates a different ψ at each modal amplitude increment. After the temporal integral in equation 3.33, the hardening factor λ can be obtained. The damping factor is calculated from energy dissipation in equation 3.37.

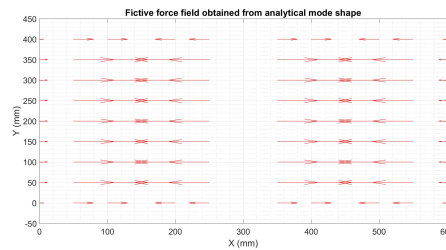


Figure 3.5: Fictive force field from the first mode

As demonstrated in the previous section, the hardening/softening factor λ is a function of ψ_{ii} , who depends on internal stress state of the plate N_i . Before

3.2. Damping induced by second-order bending strain in von Kármán plate 83

undertaking the comparison of λ obtained in two methods, a study on the nonlinear term $R(N_i, \phi_i)$ distribution in the calculation domain may give a preliminary view of the resemblance between the two solutions. As there is no variance in the y direction in the analytical method, only the distribution in terms of x is presented in figure 3.6b. The distribution obtained corresponds to a modal amplitude of 0.2.

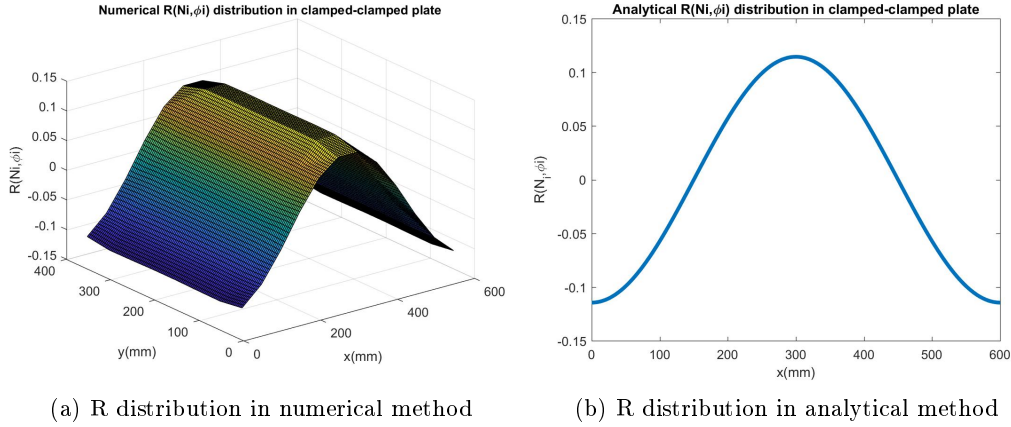


Figure 3.6: Comparison of nonlinear term $R(N_i, \phi_i)$ between analytical and numerical method

The distribution of the nonlinear term resembles the form of cosine function, which is due to the cosine-form mode shape imposed on the structure. The two methods give the same evaluation of $R(N_i, \phi_i)$ at the same modal amplitude, the only difference takes place at the longer side of the numerical model, this can be ascribed to the intrinsic error of the first-order finite difference scheme used in the fictive force field calculation. The good correlation of $R(N_i, \phi_i)$ implies that the nonlinear terms $\psi_{ii}(t)$ in the time domain obtained respectively by the two methods match also well.

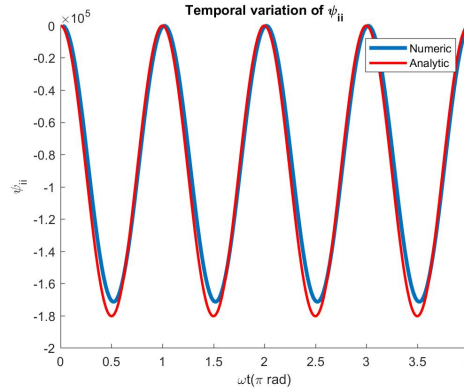


Figure 3.7: ψ_{ii} obtained by analytical and numerical method

As illustrated in figure 3.7, the nonlinear temporal term ψ_{ii} is a periodic function under the clamped-clamped condition, as with the modal amplitude, ψ_{ii} varies sinusoidally, but it stays negative-definite, which in turn guarantees a positive-definite λ and the structure is always under the hardening effect.

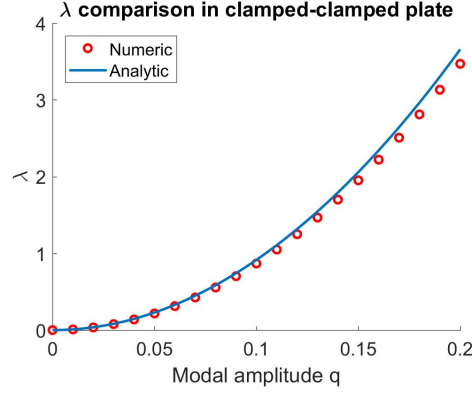


Figure 3.8: λ obtained from analytical and numerical solution

Both the spatial distribution of $R(N_i, \phi_i)$ and the temporal variation of ψ_{ii} are in good correlation, the hardening factor in this way logically shows no sign of separation between the two methods, as shown in figure 3.8. Therefore the exactitude of the numerical method is verified and it can be applied to cases with more complicated mode shapes.

Even though the previously imposed mode shape is similar to the real first resonance mode shape, its mono-dimensional property prohibits it to take into account the curvature in the y direction, which we believe may also modify the hardening effect as well as the damping property of the structure. By the same operation composed of finite difference schemes, the fictive force field can be obtained in figure 3.9.

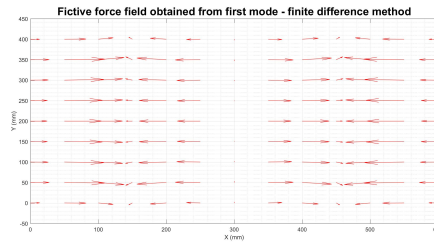


Figure 3.9: Fictive force field of the first mode shape

Regardless the similarity with the fictive force field obtained by analytical method, it should be noted that the non-zero derivatives in the y direction can result in a field that is not exactly parallel to the x axis, especially for the points on the boundary $y = 0$ mm and $y = 400$ mm. From the λ obtained in figure 3.10a, the

3.2. Damping induced by second-order bending strain in von Kármán plate 85

hardening effect is weaker in real mode shape than analytical approximation. Due to the absence of dissipative mechanism, the damping ratio is zero in clamped-clamped plate.

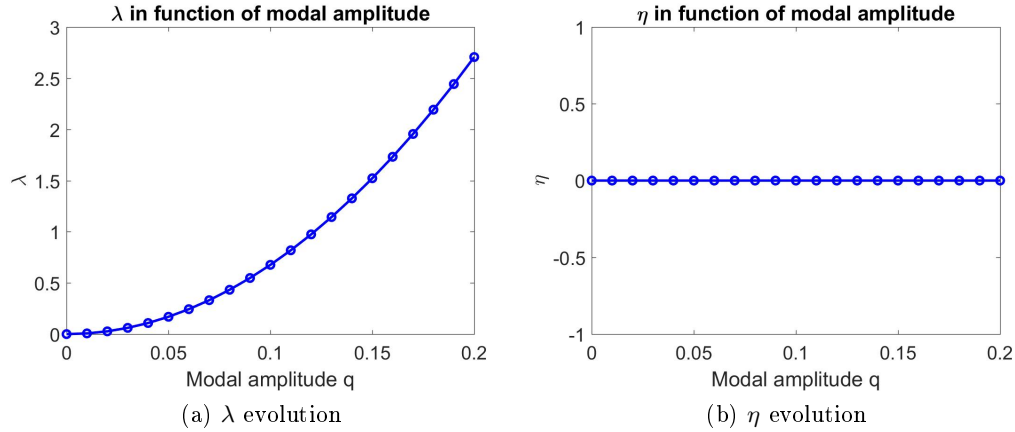


Figure 3.10: λ and η versus modal amplitude

The hardening factor increases with the increase in modal amplitude, which signifies that the structure becomes stiffer under bigger displacement.

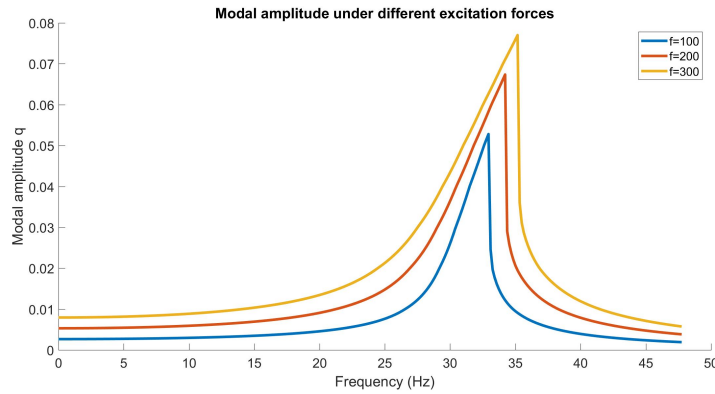


Figure 3.11: Frequency response curve under three different modal forces

The resonance moves towards higher frequencies owing to the hardening effect. For any given frequency, bigger excitation forces result in larger displacement.

3.2.8 Numerical solution of clamped-slipping plate

In the case with one slipping boundary, the left boundary is still clamped but the right boundary is subjected to a frictional clamp where the edge is supposed to slip under large modal amplitude. The contact area of 4000 mm^2 under the frictional clamp is considered to stay constant, the coefficient of friction is fixed at 0.3.

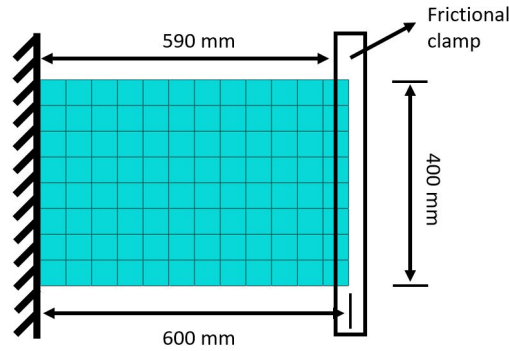


Figure 3.12: Rectangular plate with one slipping boundary

In order to verify the influence of friction when slipping is activated, a comparison of the slipping boundary's trajectory with the analytical method, which is expressed in section 2.4.3, is made. To guarantee the coherence with the analytical method, the cosine function mode shape is used for the fictive force field in the numerical solution.

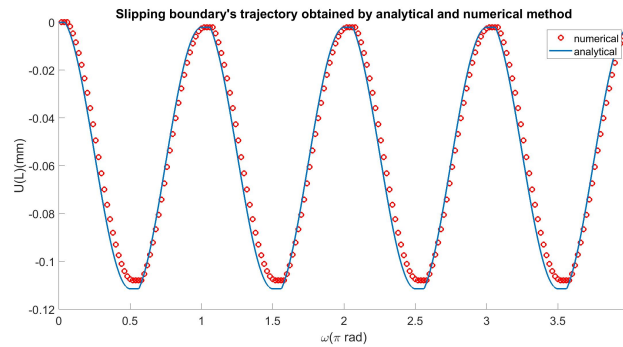


Figure 3.13: Trajectories comparison

The comparison with the analytical expression in figure 3.13 confirms the correctness of the friction property applied in the numerical solution. So that it is eligible to be used for calculations with the real mode shape. A fictive force field which corresponds to a maximum modal amplitude of 0.2 is applied to the in-plane problem, the frictional property used is presented in section 3.4, the clamping pressure is of 0.5 MPa. The alternative sticking and slipping phases can be observed under two charging cycles. The frictional force increases during the sticking period and is saturated when the slipping occurs. The compression's effect can also be observed from the fact that the right boundary can no longer return to its original position, this phenomenon is produced in the relaxing phase by the frictional force which points to the clamped edge.

3.2. Damping induced by second-order bending strain in von Kármán plate 87

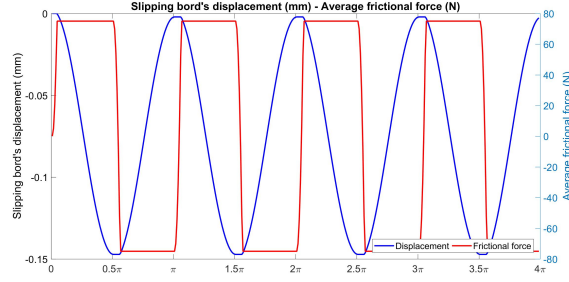
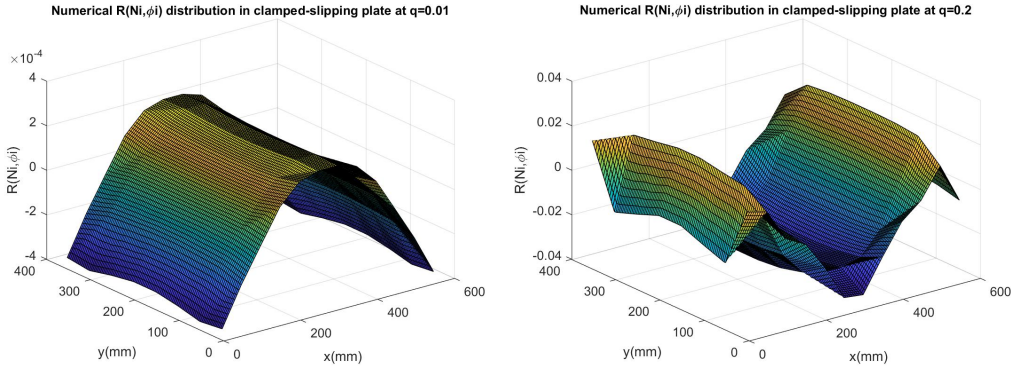


Figure 3.14: Average frictional force and displacement on the slipping edge

Here it is worth noting that the alternative sticking-slipping transition is able to change the internal stress distribution pattern under different modal amplitude, which will surely influence the hardening and damping behavior, therefore we need to analyze the nonlinear term distribution with slipping and without slipping separately.



(a) $R(N_i, \phi_i)$ distribution in sticking at $q = 0.01$ (b) $R(N_i, \phi_i)$ distribution in slipping at $q = 0.2$

Figure 3.15: Comparison of nonlinear term $R(N_i, \phi_i)$ between sticking and slipping phase

When the modal amplitude reaches $q = 0.01$, the friction force is still able to hold the slipping boundary at its original position, the internal $R(N_i, \phi_i)$ distribution is similar to that in figure 3.6a. Once the clamped boundary is released under bigger amplitude, for example if q reaches 0.2, the internal stress distribution is more complicated and its pattern resembles that of $\sin 2\alpha x$ function. This observation confirms that the internal stress-dependent term $R(N_i, \phi_i)$ is sensitive to boundary condition changes, which will in consequence influence the ψ_{ii} variation in the time domain.

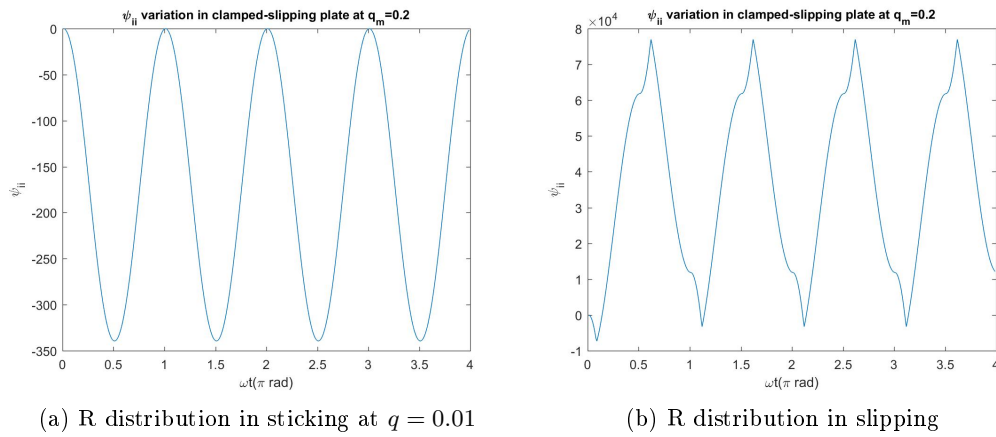


Figure 3.16: Comparison of nonlinear term ψ_{ii} between sticking and slipping phase

When the modal amplitude is not big enough to activate slipping, the plate can be regarded as under clamped-clamped boundary condition. The variation of ψ_{ii} is negative-definite, which leads to a positive λ and signifies a hardening effect. However as the amplitude increases, the structure enters an alternative transition between sticking and slipping. As illustrated in figure 3.16b, the average ψ_{ii} is a positive value, this will result in a negative λ and the structure is thus softened.

In order to analyze the influence of clamping force, the hardening and damping factors are calculated under 3 different pressures 0.5 MPa, 1 MPa and 2 MPa.

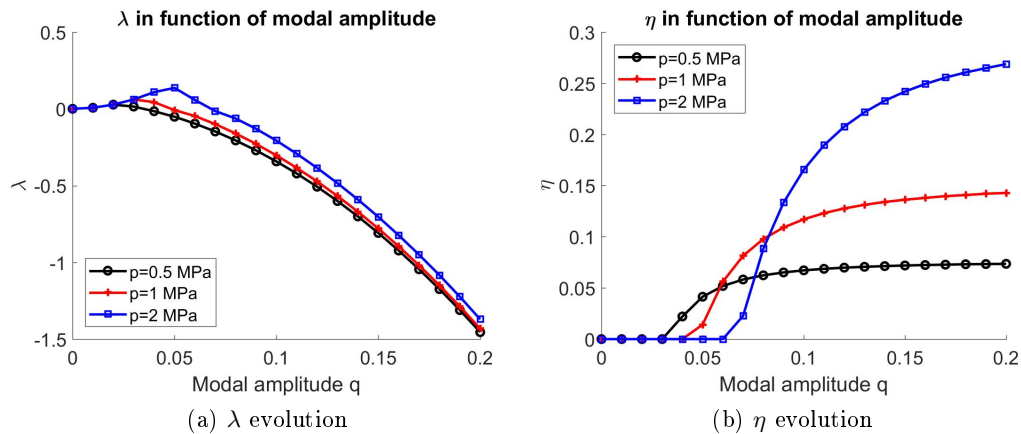


Figure 3.17: λ and η versus modal amplitude

By comparing the figure 3.17a and 3.17b, the softening effect is shown to appear earlier than the occurring of slipping. The hardening effect is gradually counteracted as the slipping phase becomes more and more dominant in one vibration cycle. In the modal range which contains slipping, bigger modal amplitude will lead to a more

softened structure.

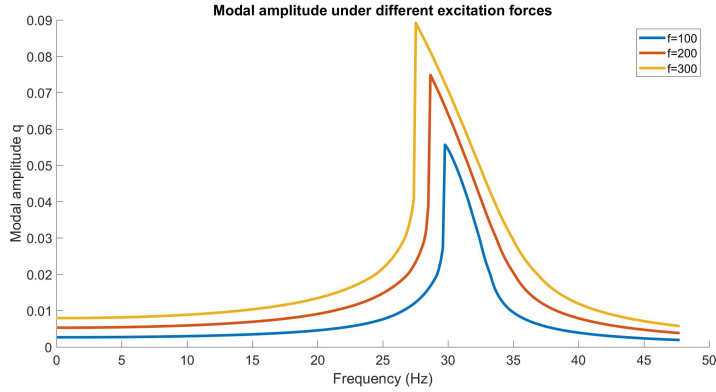


Figure 3.18: Frequency response curve with one slipping boundary

The presence of slipping boundary changes the frequency-response property of the structure. In the range of the current excitation force, the structure becomes softer with a decreasing resonance frequency under bigger modal force, which corresponds to the monotone negative value range in figure 3.17a. The slipping boundary also results in a bigger modal response under the same excitation force compared to clamp-clamp boundary condition in figure 3.11. Compared to the effect of in-plane coupling, the influence of boundary slipping is shown to be more dominant in the response under big excitation force.

3.2.9 Extension to non-linear mode

The single mode method presented in the previous sections discounts the coupling between modes by non-linear terms. This coupling can be taken into account by using the notion of non-linear mode. The non-linear mode is defined by a linear superposition of linear modes

$$\tilde{\phi}_i = \sum_{j=1}^n b_{ij}(q)\phi_j \quad (3.50)$$

where ϕ_j is the j th linear mode and $b_{ij}(q)$ are participation factors of each mode with $b_{ii} = 1$, n is number of retained linear modes. This normalization is valid only in cases where the structure is excited at its i th natural frequency and it's the i th mode that is dominant in the shape composition. The participation factor is considered as a function of modal amplitude q and satisfies the initial condition $b_{ij}(q = 0) = 0$. The non-linear mode notion presented here is always in the realm of mono-mode response calculation, the only difference compared to single mode method is that the mode chosen retains no longer its shape, but changes in function of modal amplitude.

The values of b_{ij} are solutions of the following eigenfunction system which is derived from equation 3.22 and 3.24.

$$-\tilde{\omega}_i^2(\mathbf{b}_{ij}) + ([\Omega^2] + [\lambda_{ij}])(\mathbf{b}_{ij}) = 0 \quad (3.51)$$

with

$$\lambda_{ij} = \frac{1}{2\pi} \int_0^{2\pi} -\psi_{ij}(t)(1 - \cos 2\theta) d\theta. \quad (3.52)$$

The $\tilde{\omega}_i$ is the non-linear natural frequency corresponding to non-linear mode $\tilde{\phi}_i$, and it is also a function of modal amplitude q .

Similar to expression 3.28 in the single mode method, the discretized form of ψ_{ij} can be written as

$$\psi_{ij} = \sum_{m=1}^N \left(N_{jx}^m \frac{\partial^2 \phi_j^m}{\partial x^2} + 2N_{jxy}^m \frac{\partial^2 \phi_j^m}{\partial x \partial y} + N_{jy}^m \frac{\partial^2 \phi_j^m}{\partial y^2} \right) \phi_i^m S^m. \quad (3.53)$$

The coupling effect can be quantified by the participation factor b_{ij} , this non-linear mode approach is called multi-mode method in the following sections. The response of forced vibration in multi-mode method is given by complex amplitude \hat{q} , which is the solution of the following equation

$$[\tilde{M}(q)\omega^2 + \tilde{\omega}_i^2(q)(1 + i\eta(q))]\hat{q} = \tilde{f}(q) \quad (3.54)$$

where $\tilde{M}(q)$ is the non-linear modal mass and $\tilde{f}(q)$ is the non-linear modal force, $\eta(q)$ is calculated with the non-linear mode shape $\tilde{\phi}_i$.

$$\tilde{M}(q) = \sum_{j=1}^n b_{ij}^2(q), \quad \tilde{f}(q) = \sum_{j=1}^n b_{ij}(q)f_j \quad (3.55)$$

3.2.10 Multi-mode method with complete slipping boundary

In order to explain the notion of non-linear mode, a rectangular plate with one complete slipping boundary, as illustrated in figure 3.12, is used for explanation with three linear modes. Since the eigenvalue problem is a (3×3) system which has three eigenvalues, the one which is the closest to the linear resonance is retained as the non-linear resonance, the corresponding vector is the participation factors (\mathbf{b}_{ij}).

In the first place we consider that both the excitation and boundary conditions are symmetric, in this case anti-symmetric modes don't contribute to the response composition. The three linear modes retained here are all symmetric and are listed in figure below. The corresponding frequencies are respectively 30.86 Hz, 88.45 Hz and 98.19 Hz. The second and third mode are very close together.

3.2. Damping induced by second-order bending strain in von Kármán plate

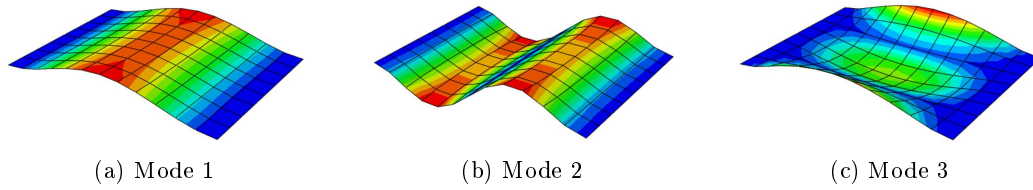


Figure 3.19: The three retained linear modes

The coupling variable ψ_{ij} is valued at each time step in quasi-static calculation. The coupling effect in the frequency domain is directly related to the λ_{ij} obtained from temporal integral. After the normalization of the first mode participation factor to 1, the evolution of (\mathbf{b}_{ij}) in terms of modal amplitude q shows that b_{11} remains 1 while b_{12} and b_{13} stay 0 for all the amplitude range. This observation signifies that the second and third mode are not coupled with the first mode under symmetric boundary conditions. This phenomenon also justifies the application of single mode method.

In order to study the participation of anti-symmetric modes, it's necessary to break the symmetry by either applying an asymmetric pressure distribution or changing the kinematic boundary conditions. The influence of different clamping pressures is firstly presented in the following section.

3.2.11 Multi mode method with non-uniform clamping pressure

Based on the fact that the coupling coefficient ψ_{ij} is a function of internal stress field which is intrinsically sensitive to boundary pressures, it's necessary to clarify its influence on inter-mode coupling. Here a non-uniform clamping pressure is applied on the clamping pad. The pressure on the lower part is twice smaller than that on the upper part. Since the rotation of the boundary DOFs are always restrained by the clamp, the boundary conditions for both upper and lower nodes can be regarded as encastre. The parametric study in terms of modal amplitude shows that force boundary conditions have no significant influence on the evolution of participation factors. The second and third mode participation factors b_{12} and b_{13} stays 0 for all the amplitude range, which means that they are not coupled with the first mode and their participations can be neglected. It is thus reasonable to infer that the participation factor is only sensitive to linear mode shapes. This deduction is to be verified in the next section.

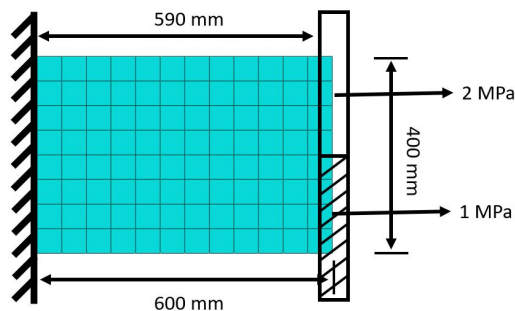
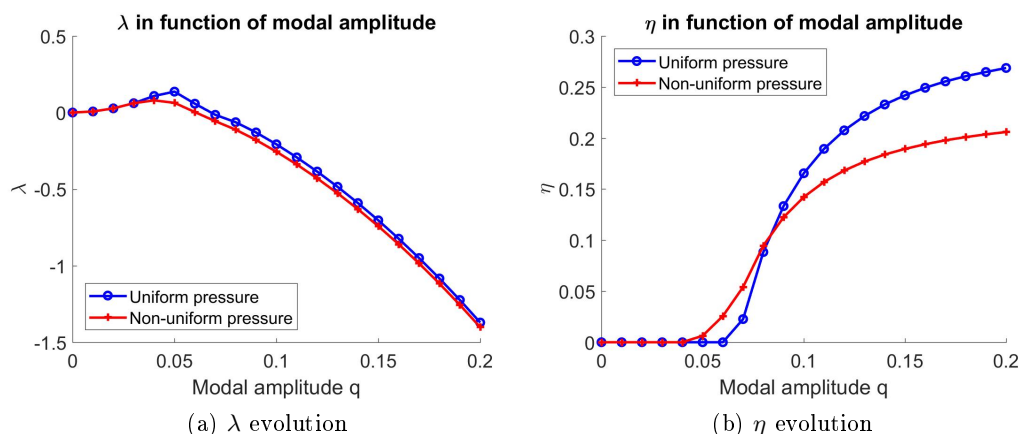


Figure 3.20: Rectangular plate with non-uniform clamping pressure

Even though the clamping pressures are not able to change the shape composition, the hardening and damping property are closely related to boundary forces. As the second and third mode are neglected, the fictive force field is generated only with the first mode shape. The comparison of coefficient λ and η under uniform and non-uniform clamping pressures are illustrated in figure below. The pressure is maintained at 2 MPa for the case with uniform clamping pressure.

Figure 3.21: Influence of clamping pressure distribution of λ and η evolution

The structure is shown to be more solidified and damped with an uniform clamping pressure along the slipping boundary. The non-uniform clamp yields a smaller average pressure which enables earlier slipping, but the maximum damping capacity is weakened.

3.2.12 Multi mode method with half slipping boundary

A drastic way to break boundary condition symmetry is to completely remove the lower part of the clamping pad. This modification changes not only force conditions, but also liberates the lower part DOFs in the linear mode calculation. The clamping pressure in this example is fixed at 2 MPa.

3.2. Damping induced by second-order bending strain in von Kármán plate

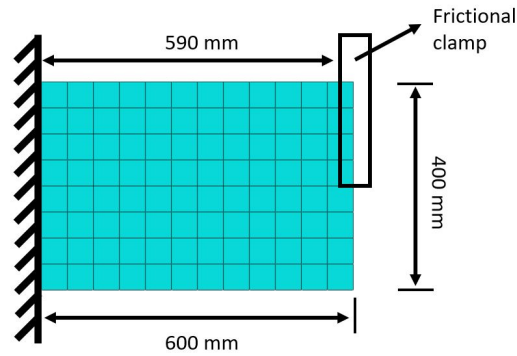


Figure 3.22: Rectangular plate with half slipping boundary

The first three modes retained for non-linear mode calculation as well as the corresponding fictive force fields are respectively illustrated in figure 3.23 and figure 3.24.

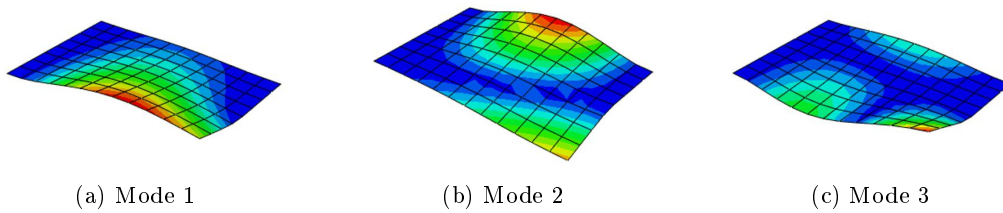


Figure 3.23: The three retained linear modes

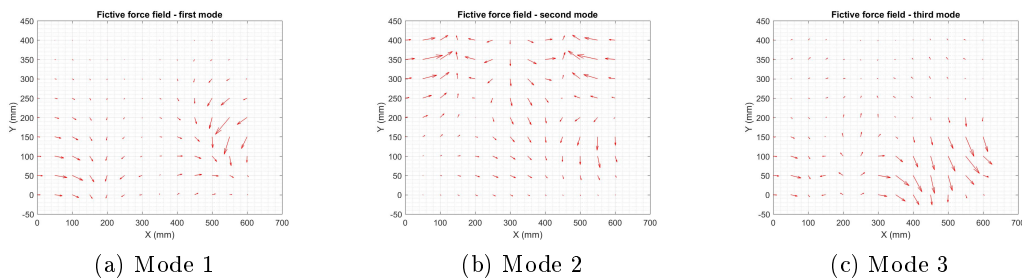


Figure 3.24: Fictive force fields of the three linear modes

The non-symmetric mode shapes will result in non-symmetric force fields, which in consequence lead to stress fields that can be coupled together. The participation factor evolution in this case is presented in figure 3.25.

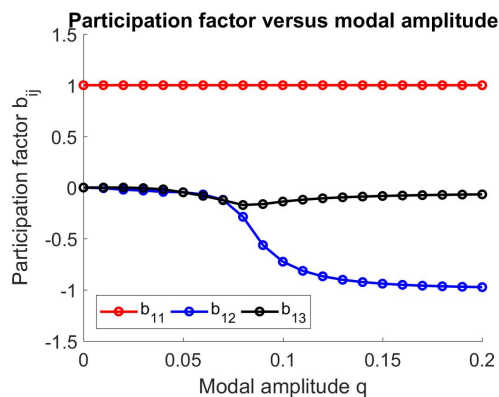
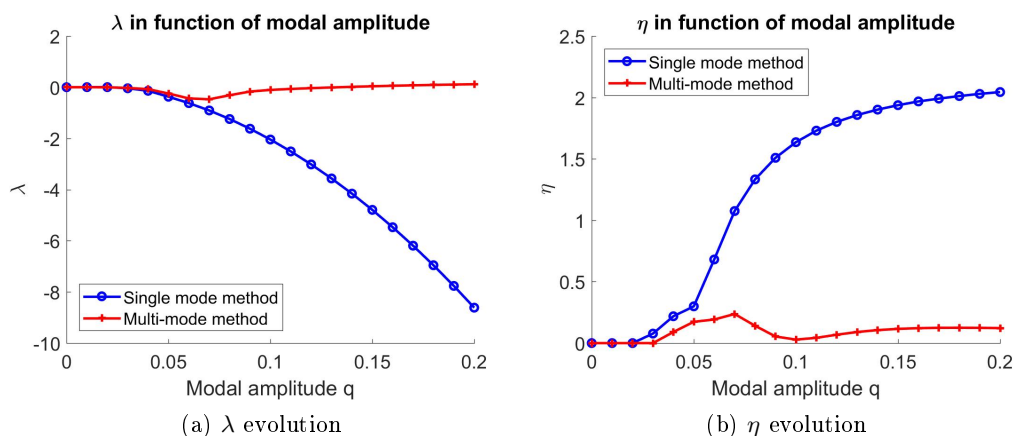


Figure 3.25: Participation factors with half slipping boundary

The second mode starts to participate in shape composition from modal amplitude of 0.05 and continues to be saturated at a constant level from 0.1. The participation of the third mode stays weak in all the range of modal amplitude. This result shows that for small modal amplitude, only one mode is sufficient to represent the overall vibration behavior of the structure, but for big modal amplitude, it's necessary to take into account the participation of other modes. In the current study, a modal amplitude of 0.05 corresponds to a physical displacement of 2 mm, which is the thickness of the plate, this deflection is already within the realm of large displacement and it is not likely to happen in vibration mechanics. Therefore the single mode method is sufficient for analysis with small displacement, even though the boundary conditions may yield inter-mode coupling, however for large modal amplitude, the participation of other modes cannot be neglected. The comparison of hardening factor λ and damping coefficient η obtained from single mode method and multi-mode method are illustrated in figure 3.26a and 3.26b.

Figure 3.26: Influence of mode shape change on λ and η evolution

The comparison shows that hardening and damping are both sensitive to mode

3.2. Damping induced by second-order bending strain in von Kármán plate

shape changes. The participation of second mode stops the on-going softening tendency and prohibits the damping capacity to grow. For small modal amplitude, it's acceptable to use only one mode shape to represent the vibration behavior since λ and η given by single and multi-mode method are almost the same, but for big modal amplitude, it's necessary to take into account the inter-mode coupling. An example of forced response is given with an oscillating excitation force applied at point A, as illustrated in figure 3.27. The excitation force amplitudes are respectively 10 N and 50 N for two different load cases.

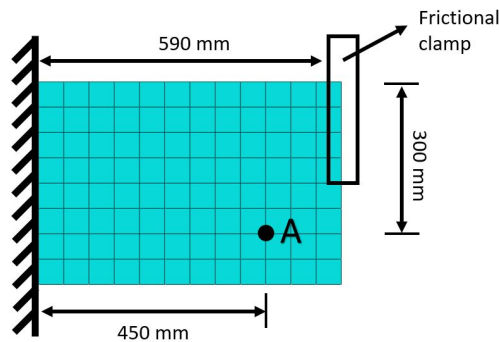


Figure 3.27: Excitation force position on the plate

The frequency-response curves in figure 3.28a and 3.28b demonstrate that for excitation forces who result in small modal amplitude, the coupling between modes is weak, so that single mode and multi-mode method provide very similar responses, however when the force is big enough to produce inter-mode coupling, the difference in response is no longer negligible. By comparing the response amplitude at resonance, the single mode method always over-estimates the damping capacity compared to multi-mode method, but for frequencies outside the resonance zone, the amplitude is relatively small and the two methods give almost the same response level, which is in consistency with the λ and η curves.

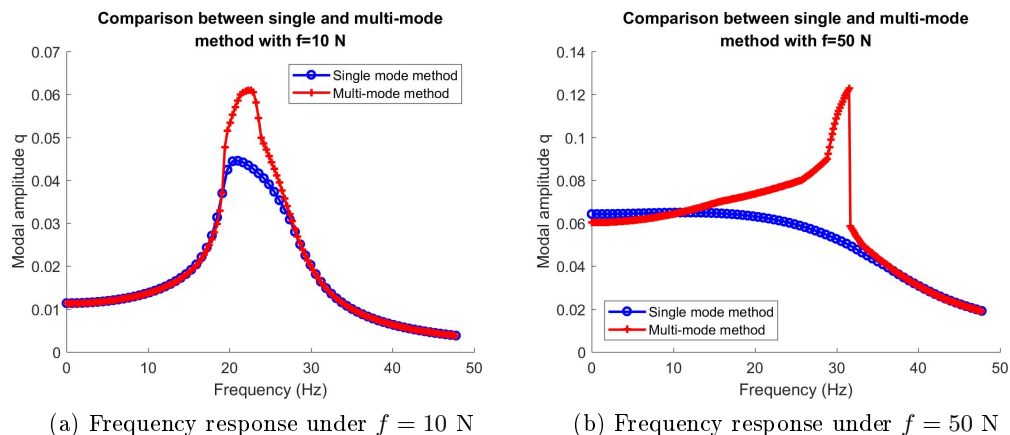


Figure 3.28: Influence of mode shape change on frequency response

3.3 Damping induced by first-order cross section's rotation in sandwich plate

3.3.1 Model description

As demonstrated in the phenomenological study of damping in sandwich plate in chapter 2, the dissipated and stocked energy are able to be expressed in analytical formulations, however this formulation is only valid when we suppose that the propagation of slipping is instantaneous, this hypothesis facilitates the derivation but neglect the possible partial slipping in real conditions. In order to make up this intrinsic deficiency in the analytical method, a numerical solution based on a 2-dimensional finite element method will be developed in this section. We are not only interested in the total energy dissipation, but also the slipping propagation during the increase in modal amplitude.

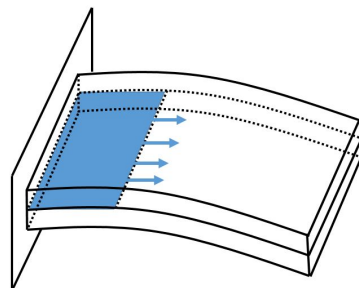


Figure 3.29: 3D sandwich model

Different from the one-layered clamped-slipping von Kármán plate, in which the slipping criteria is based on in-plane force, the slipping in sandwich plate is determined by interface stress, which depends on the rotation of the cross section.

As for the influence of the second-order fictive force field, due to the fact that the mode shape is the same for upper and lower plate, the in-plane excitation is identical for the two layers, which implies that there is no relative displacement and thus no induced frictional force. Even though the fictive force field doesn't influence the sticking-slipping transition, it can modify the in-plane displacement field, which will in turn reshape the contact interface's form.

3.3.2 Shear force field formulation

When the two plates of thickness h are pressed together by the clamping force, before the slipping occurs, they can be regarded as one plate of thickness $2h$. The shear force at the mid-plane can be obtained by the moment equilibrium on the infinitesimal element, which yields

$$\tau_{xz} = \tau_{zx} = \tau_x, \quad \tau_{yz} = \tau_{zy} = \tau_y. \quad (3.56)$$

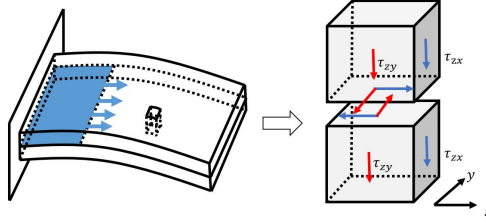


Figure 3.30: Shear stress on contact interface

As illustrated in figure 3.30, all the shear components who have the same magnitude are marked by the same color. According to Kirchhoff-Love plate theory, the shear stress at the contact interface can be expressed by

$$\tau_x = \frac{D}{h} \frac{\partial}{\partial x} \nabla^2 w, \quad \tau_y = \frac{D}{h} \frac{\partial}{\partial y} \nabla^2 w, \quad (3.57)$$

where D is the bending rigidity of the plate which takes the expression $Eh^3/(12(1-\nu^2))$, $\nabla^2 w$ is written as

$$\nabla^2 w = \frac{\partial^2 w}{\partial x^2} + \frac{\partial^2 w}{\partial y^2}. \quad (3.58)$$

It should be noted that the shear stress is zero on the free boundary, that is

$$\tau_y|_{y=0} = 0, \quad \tau_y|_{y=b} = 0, \quad \tau_x|_{x=L} = 0, \quad (3.59)$$

where b is the width and L the total length. The spatial derivatives in equation 3.58 and 3.59 can be approximated by the finite difference schemes proposed in the previous fictive force field calculation.

In this way the shear force field on the middle plane can be obtained for sticking-slipping verification. In the current step, the shear stress is only expressed on each node, the stress on other points should be interpolated by nodal values. As we are for the moment interested in the first resonance response, the shear stress field of the first mode is illustrated in figure below. The shear stress vector is in constant transition between two opposite directions, the current representation corresponds to the stress field on the upper surface of the lower plate with the deformation form in figure 3.29.

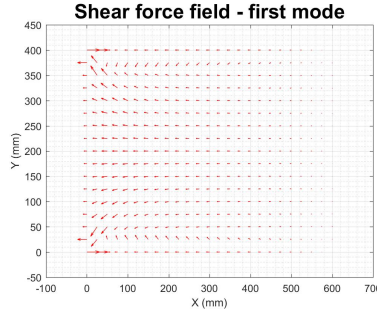


Figure 3.31: Shear stress field on contact interface

The force field reveals that the distribution of shear stress is not uniform under the deformation of the first mode. The shear stresses that are adjacent to the encastre is bigger than those in the neighboring of the free boundary on the right. When the stress reaches its maximum μP , the friction force can no longer retain the node at its original position and thus the slipping occurs. This observation implies that as the amplitude increases, the slipping starts from the fixed boundary and propagates to the free edge.

3.3.3 Solution procedure and displacement kinematics

In order to facilitate the estimation of energy dissipation, the slipping-sticking verification is element-based, which requires that the stress components valued at each node should be interpolated to the center of each element so as to be regarded as the average stress state for comparison with the friction limit. Take the modal amplitude as q , the reference nodal stress field under the normalized mode as τ_n , the reference element stress field as τ_m .

$$\tau_m = \frac{1}{4} \sum_{i=1}^4 \tau_n^i, \quad i = \text{node number of each element} \quad (3.60)$$

The incremental approach is adopted in the slipping-sticking verification. The initial stress field is zero. The stress state of step $t + 1$ can be expressed as

$$\boldsymbol{\tau}_m^{t+1} = \boldsymbol{\tau}_m^t + dq \cdot \boldsymbol{\tau}_m, \quad (3.61)$$

where dq is the modal amplitude increment.

The resultant stress τ_{mr} for a given element is written as

$$\tau_{mr} = \sqrt{\tau_{mx}^2 + \tau_{my}^2}. \quad (3.62)$$

If the stress resultant is still within the friction cone defined by contact properties,

$$\tau_{mr} < \mu P, \quad (3.63)$$

the considered element is in sticking phase. The corresponding in-plane DOFs on the upper and lower plate can be treated as being stucked together and keep the same in-plane displacement as the precedent step, moreover the friction force doesn't change its direction.

$$\mathbf{U}_{\text{lower,rotation}}^{t+1} = \mathbf{U}_{\text{lower,rotation}}^t, \quad \mathbf{U}_{\text{upper,rotation}}^{t+1} = \mathbf{U}_{\text{upper,rotation}}^t. \quad (3.64)$$

After several increments, the stress resultant will reach the friction limit and the element enters the slipping phase. Regardless the increase in modal amplitude, the stress resultant will be saturated to the value μP until the moment when the modal amplitude starts to decrease. In the slipping phase, the locking on the upper and lower DOFs is removed and the relative displacement follows the kinematic of the Kirchhoff-Love plate theory, where in-plane displacements are linearly proportional to cross-section's rotation,

$$U_{x,rotation}^{upper} = -\frac{h}{4}\theta_y, \quad U_{y,rotation}^{upper} = \frac{h}{4}\theta_x, \quad U_{x,rotation}^{lower} = \frac{h}{4}\theta_y, \quad U_{y,rotation}^{lower} = -\frac{h}{4}\theta_x, \quad (3.65)$$

where h is the total thickness of the upper and lower plate, the direction of rotation follows the right hand rule.

After the slipping occurs, the friction force points to the opposite direction of the relative speed, which can be expressed by the relative displacement in quasi-static formulation.

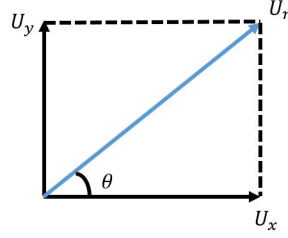


Figure 3.32: Displacement components

The friction direction for the upper plate can thus be expressed as

$$\cos \theta = -\frac{\theta_y}{\sqrt{\theta_x^2 + \theta_y^2}}, \quad \sin \theta = \frac{\theta_x}{\sqrt{\theta_x^2 + \theta_y^2}}. \quad (3.66)$$

The friction force is thus updated with the new amplitude and direction. The alternative transition of direction can be realized by function $\text{sign}(q \cdot \dot{q})$, the derivation of which is given from equation 1.37 to 1.43.

$$\begin{aligned} f_x^{upper} &= -\text{sign}(q \cdot \dot{q}) \cdot \cos \theta \cdot \mu P \\ f_y^{upper} &= -\text{sign}(q \cdot \dot{q}) \cdot \sin \theta \cdot \mu P \end{aligned} \quad (3.67)$$

Since the upper and lower plate are in a relation of action-reaction, the friction force at step t on the lower part is of the same amplitude as the upper part but of opposite direction.

$$\mathbf{f}_{\text{upper}}^t = -\mathbf{f}_{\text{lower}}^t. \quad (3.68)$$

The renewed friction force cannot be directly superimposed with the second-order strain induced fictive force field, since it is an element-based vector in which the friction force is assumed to be constant for every point on a given element. This generated friction force field needs to be transformed into an equivalent nodal force vector, which can then be substituted in the in-plane displacement calculation along with the fictive force field, the change in contact surface's form can in such a way be taken into account.

$$[\mathbf{K}_{\text{plane}}](\mathbf{U}_{\text{lower,plane}}^t) = (\mathbf{f}_{\text{lower}}^t) + (\mathbf{f}_{\text{fictive}}^t) \quad (3.69)$$

$$[\mathbf{K}_{\text{plane}}](\mathbf{U}_{\text{upper,plane}}^t) = (\mathbf{f}_{\text{upper}}^t) + (\mathbf{f}_{\text{fictive}}^t) \quad (3.70)$$

The fictive force field of the first mode is illustrated in figure 3.33. The force intensity at the encastre and free boundary are shown to be weaker than that in the middle of the plate. Given the curvature of the first mode shape, different from the frictional force field whose effect is in permanent transition between traction and compression, the effect of the fictive force field is always stretching on the upper and lower plate.

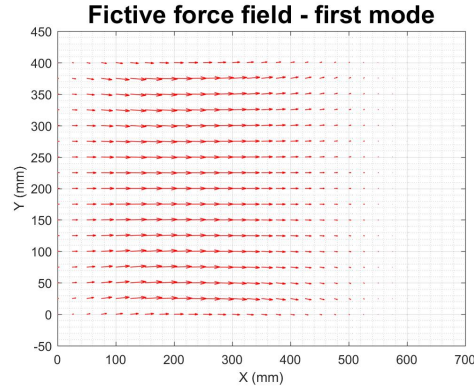


Figure 3.33: Fictive force field of first mode in sandwich plate

The relative displacement between two plates is hence divided into two parts, one is expressed in equation 3.65 where the displacement is created by cross section's rotation, another is induced by in-plane body force.

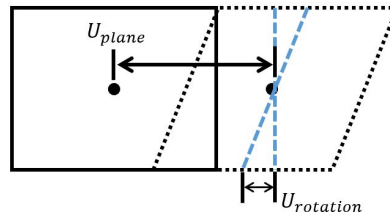


Figure 3.34: Displacement components

Here we assume that when there is no rotation-induced displacement, the in-plane displacement due to body force should be neglected since it doesn't contribute to energy dissipation. If the slipping occurs, the in-plane force induced nodal displacements are interpolated to the center of each element and superimposed with the rotation-induced movement. The displacement vector of both plates at step t is thus expressed as

$$\mathbf{U}^t = \mathbf{U}_{\text{plane}}^t + \mathbf{U}_{\text{rotation}}^t. \quad (3.71)$$

3.3.4 Sticking-slipping evolution

According to the shear stress field obtained from Kirchhoff-Love plate theory, the stress field is not uniform which implies that the slipping doesn't occur simultaneously on the contact surface. This inference can be verified by the visualized representation of the shear stress field during the modal amplitude increase. A maximum modal amplitude of 1 is applied on the structure, which corresponds to a physical displacement of 32 mm. The sticking-slipping state is illustrated under

different amplitudes. The yellow means that the element is in slipping and dark blue indicates sticking.

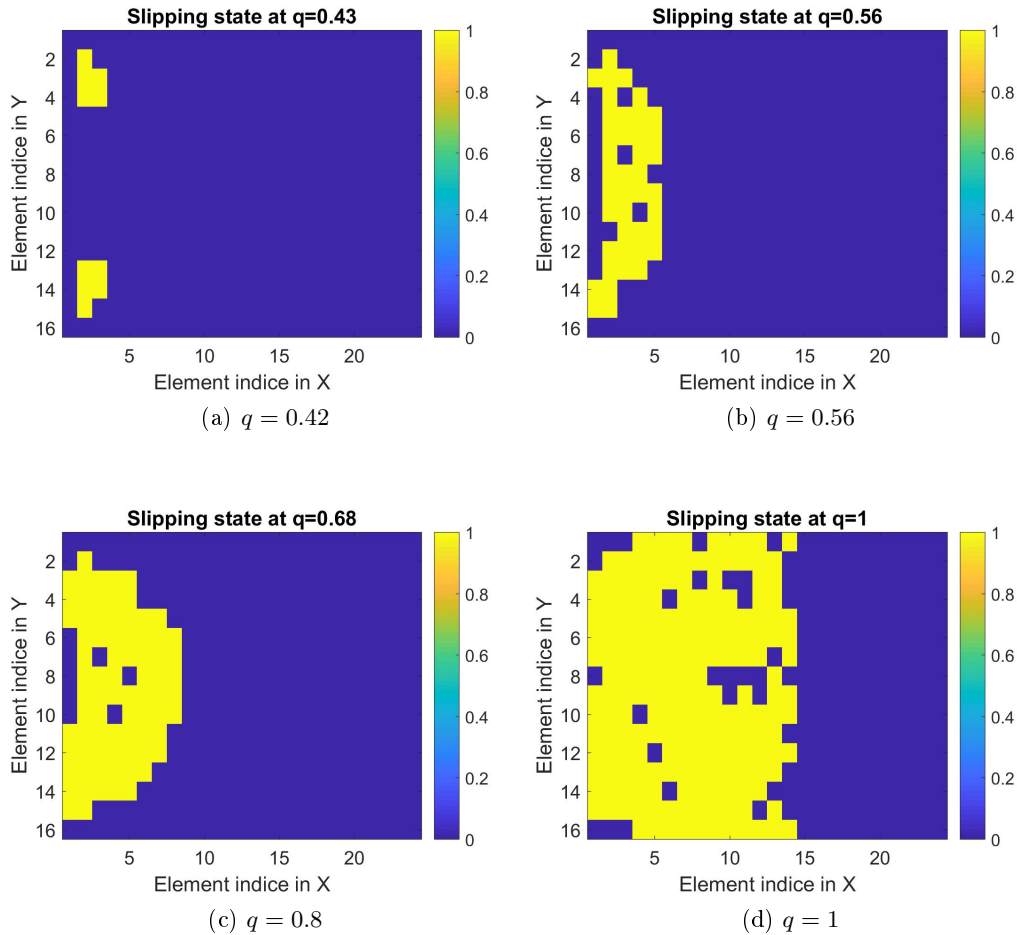


Figure 3.35: The evolution of slipping state with the increase in modal amplitude

The evolution of shear stress distribution reveals that slipping starts from the encastre boundary and propagates to the free edge. At the beginning of the slipping, the frontier between the sticking and slipping area is similar to a parabola, as the modal amplitude increases, the frontier gradually changes to a straight line and maintains its form until the maximum amplitude. It should be noted that the free edge can never enter the slipping phase based on the shear stress distribution expression in the currently proposed method.

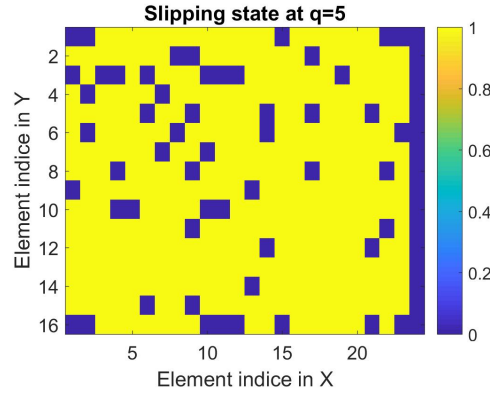


Figure 3.36: Slipping state at $q = 5$

If the modal amplitude continues to increase until it reaches 5, almost all the points on the contact surface is in slipping phase, but this modal amplitude corresponds to a physical displacement of 162 mm, on which level the material's yielding stress is already reached and is unachievable in real conditions.

3.3.5 Calculation of damping ratio

The dissipated energy can be estimated from the relative displacement between the two plates

$$\mathbf{U}_{\text{relative}} = \mathbf{U}_{\text{upper}} - \mathbf{U}_{\text{lower}}. \quad (3.72)$$

As incremental calculation is adopted in the current analysis, the total dissipated energy in one cycle is the accumulation of ΔW of all the steps.

$$\Delta W = \sum_{t=2}^n (\boldsymbol{\tau}^t)^T |(\mathbf{U}_{\text{relative}}^t) - (\mathbf{U}_{\text{relative}}^{t-1})| S, \quad (3.73)$$

where $(\boldsymbol{\tau}^t)$ is the vector which contains the average shear stress in each element at step t , S is element's area, as the elements in the current study are of the same size, the area is a constant for everyone of them.

The maximum elastic energy can be expressed in the same ways as in equation 3.38. However the elastic energy expressed in the form of resonance frequency has its own limitation, since the resonance frequency of the assembled structure changes as the clamping pressure is modified. Here we can in the first place consider two extreme cases: zero and infinite coefficient of friction. In the case of zero friction, the two plates are regarded as independent, thus the maximum elastic energy is the sum of the energy relatively stocked in each plate. In the case of infinite coefficient, the friction force blocks completely the points on the contact surface, thus the two

sticked plates forms one plate of thickness $2h$. The resonance frequency of the two cases follows the relation $\omega_{\mu=\infty} = 2\omega_{\mu=0}$. The stocked energy is thus expressed as

$$\begin{aligned} E_{max,\mu=0} &= 2 \cdot \frac{1}{2} \omega_{\mu=0}^2 q^2, \\ E_{max,\mu=\infty} &= \frac{1}{2} \omega_{\mu=\infty}^2 q^2. \end{aligned} \quad (3.74)$$

The case with infinite coefficient of friction can stock two times more energy than the case with zero friction, $E_{max,\mu=\infty}/E_{max,\mu=0} = 2$. On the one hand it is impossible to block all the points on the contact interface, on the other hand there must be a certain slipping that occurs, so that here we consider that the resonance frequency of the assembled structure is closer to $\omega_{\mu=0}$ and is weakly influenced by the friction. The stocked energy can thus be approximated by $E_{max,\mu=0}$ and the damping coefficient is written as

$$\eta = \frac{1}{2\pi} \frac{\Delta W}{E_{max,\mu=0}}. \quad (3.75)$$

In order to fully illustrate the evolution of damping coefficient in terms of modal amplitude, an amplitude $q = 5$ is necessary to reveal the maximum damping capacity even though it is unrealistic. The reliability of the proposed in-plane friction model for sandwich structure can be verified in the comparison with the analytical model in chapter 2. The applied analytic mode shape in the numerical approach, as expressed in 2.14 should be normalized to the mass to be in coherence with the von Kármán model, the normalizing coefficient α is calculated in equation 3.76.

$$\rho b h \int_0^l \frac{\alpha^2}{4} \left[3 \left(\frac{x}{l} \right)^2 - \left(\frac{x}{l} \right)^3 \right]^2 = 1, \quad \alpha = \sqrt{\frac{140}{33\rho b h l}} = \sqrt{\frac{140}{33m}}, \quad (3.76)$$

where m is the total mass of the plate. The comparison with the analytical model is presented in figure 3.37. Both models show that there exists an optimal amplitude for maximum damping coefficient under a given clamping pressure, and the damping capacity decreases as the modal amplitude continues to increase after passing the optimal point. However, the numeric model gives a later slipping activation and the change in damping coefficient is more brutal compared to the analytic solution. The difference between the two models can be ascribed to the difference in elastic stocked energy calculation. The numerical model's elastic energy is approximated by the first mode elastic energy, whereas the stocked energy in the analytic model is derived directly from the strain and stress relationship under the imposed mode shape.

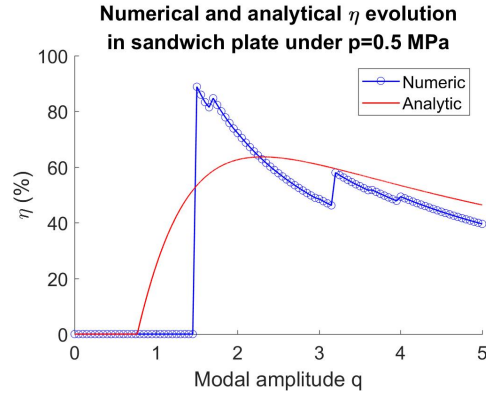


Figure 3.37: η evolution obtained by numerical and analytical methods

The damping ratio is thought to be a function of mode shape, even though the analytical mode shape can approximate and facilitate the derivation, the slight difference with the real numerical mode can result in a significant distinctness between them. The comparison of damping ratio obtained relatively obtained with the approximated analytical and real numerical mode shape is illustrated below.

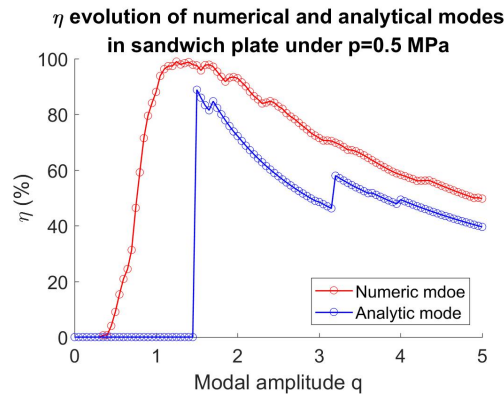


Figure 3.38: η evolution under real numerical and approximated analytical mode shape

The evolution of η under the real numerical mode is smoother than that of analytical mode, this is due to the fact that the slipping-sticking transition under the real mode shape is progressive, where points closer to the encastre starts to slip in the first place and other points follow later. However in the case of approximated analytical mode shape, the deflection's expression is obtained from a concentrated loading on the free edge, which results in a uniform shear stress along the length of the plate, therefore the shear stress on the contact surface is thus uniform which implies that all the contact nodes will slip and stick at the same time. In this way, a brutal change in dissipated energy is inevitable. Due to the similarity between the two mode shapes, the maximum damping capacity as well as the damping evolution under bigger amplitude are in good correlation.

3.3.6 Influence of second-order fictive force field

Like in any plate in bending, the in-plane force induced by transverse displacement can be regarded as an exterior excitation force, even though its influence is of second-order. Two calculation cases with and without second-order force field are superimposed in figure 3.39 to analyze the role of fictive force field on sandwich plate.

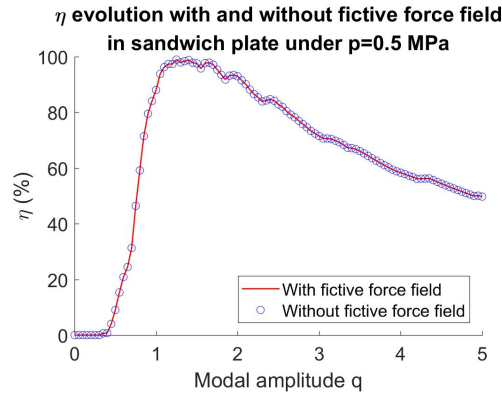


Figure 3.39: η evolution with and without second-order fictive force field

The two curves are perfectly superimposed, it signifies that the fictive force field is shown to have no influence on the evolution of damping coefficient. This is because the fictive force field applied on the upper and lower plate is the same, which results in a synchronous movement in the two layers, and thus there is no relative displacement between them. In other words, the fictive force field doesn't contribute to energy dissipation. However according to the theory in the previous section on the von Kármán plate, the hardening/softening effect due to the in-plane stress cannot be neglected.

3.4 Conclusion

Being complementary to chapter 1 which provides a preliminary introduction to analytical 1D frictional damping, the current chapter mainly deals with the difficulty encountered during the calculation of friction on a 2D plane, notably the sticking-slipping transition mechanism in numerical formulation. Just like the previous chapter, the proposed method is applied on the sandwich plate and von Kármán plate in an academic context. The challenge resides in the extension of friction force from an infinite dimension in the width direction to a limited dimension on a 2D plan, it requires that more attention should be paid to the determination of frictional force's direction during the variation of modal amplitude. Besides, the second-order in-plane force is also an influential factor in both cases

and is analyzed in the current study.

The second-order damping induced by fictive force field is treated in the first place. It is shown that the fictive force field is a function of spatial derivatives of the transverse displacement w . Due to the discretized form of the calculation domain, the derivatives are evaluated by finite difference method. The non-linear term in the von Kármán plate equation couples together the in-plane force and the mode shape, its influence can be reflected by the change in stiffness and damping property after the transformation to the frequency domain and the treatment of the HBM method. Since the internal stress field is sensitive to boundary conditions, a small modification on the boundary nodes can result in a drastic change in hardening/softening effect as well as the damping property of the whole structure. In terms of mode shape approximation, the single mode method is then extended to the multi-mode method which incarnates the notion of nonlinear mode shape. The participation factor of higher order modes is also a function of the coupling term ψ_{ij} in which the internal force field as well as the mode shape are embedded. According to the variation of the participation factors, the nonlinear mode at resonance is thought to be only composed of the first mode shape when the modal amplitude is relatively small, as the modal amplitude increases, the participation of other modes can be taken into account. As the modal amplitude in industrial applications are all in the linear range of the material, the nonlinear mode shape evolution justifies the use of single mode method for damping calculation in real conditions.

The planarization of friction problems by the use of in-plane forces can also be transplanted to the sandwich plate model. Here the initial state of the clamped plate can be considered as one whole piece, at the middle plane of which there exists a fictive friction contact surface. The stress field on the fictive plane can be obtained by the kinematic of Kirchhoff-Love plate theory, in this way the variation together with the saturation of the frictional force component in the x and y direction can be expressed as a function of modal amplitude. Due to the non-uniform distribution of the frictional stress field, the slipping-sticking transition under the first mode shape is a gradual process. The slipping starts from the encastred edge and propagates to the free boundary. This slipping pattern results in a higher maximum damping capacity, compared to the approximative mode shape used in the analytical model. In general, the damping obtained from the numerical method are in good correlation with the analytical approach both in terms of magnitude and variation trend. As for the influence of second-order bending-induced fictive force field, both plates are under the same excitation field, so that there is no induced relative displacement and supplementary energy dissipation, the second-order fictive force field doesn't affect the formation of damping, but its influence on internal stress field associated with the assembled structure's stiffness cannot be neglected.

The semi-analytical methods on two academic models in the current chapter

deepen the understanding of the formation of friction damping. They not only provide a theoretical framework of the 2D sticking-slipping mechanism, but also justifies the feasibility of damping modelization in a quasi-static calculation. Additionally, the study on nonlinear mode confirms the theoretical justification for the use of single mode method in damping calculation at resonance. Nevertheless, we should be aware of the intrinsic limitations in the proposed methods. The finite difference scheme requires that the calculation domain is structured, even of a rectangular form, which prohibits it to be applied on structures with more complex geometries. Even though the softening-hardening effect is shown for the moment to be just present in von Kármán plate, the same phenomenon must exist in shell structures, where the coupled term ψ_{ij} will be more difficult to be expressed, so as the hardening/softening effect. The extension of the current method to cases with general shapes is the path for future improvement and development.

Experiment

Contents

3.1	Introduction	69
3.2	Damping induced by second-order bending strain in von Kármán plate	70
3.2.1	Formulation of fictive force field	70
3.2.2	Discrete method of derivatives' evaluation	72
3.2.3	Friction properties	74
3.2.4	Solution procedure	75
3.2.5	Analytical solution of clamped-clamped plate	79
3.2.6	Analytical solution of clamped-slipping plate	80
3.2.7	Numerical solution of clamped-clamped plate	81
3.2.8	Numerical solution of clamped-slipping plate	85
3.2.9	Extension to non-linear mode	89
3.2.10	Multi-mode method with complete slipping boundary	90
3.2.11	Multi mode method with non-uniform clamping pressure	91
3.2.12	Multi mode method with half slipping boundary	92
3.3	Damping induced by first-order cross section's rotation in sandwich plate	96
3.3.1	Model description	96
3.3.2	Shear force field formulation	97
3.3.3	Solution procedure and displacement kinematics	98
3.3.4	Sticking-slipping evolution	101
3.3.5	Calculation of damping ratio	103
3.3.6	Influence of second-order fictive force field	106
3.4	Conclusion	106

4.1 Introduction

In order to verify the exactitude of the theory proposed in the phenomenological study, a partially clamped sandwich beam with symmetric geometry is adopted in the experimental study. The design of the specimen is based on the analytical modelization in equation 2.36. Modal amplitude is measured by two captors in a

differential system. The frequency response curve is drawn with different clamping pressures and excitation levels. The damping parameters are then found by the half-power bandwidth method.

4.2 Specimen design

The main difficulty in damping set-up design is to limit the extra energy dissipation which takes place mainly at the interface between specimen and fixation. The supplementary dissipation in the clamp may influence the damping level of the structure and consequently modify the frequency-response curve. The cantilever sandwich beam model requires that one end of the beam is encastred. The majority of the set-ups in the bibliography use clamp to build rigid fixation, but the presence of clamp will surely bring in more contact surface, and therefore more extra energy dissipation. The solution proposed here is to build a symmetric structure who is excited at its symmetry point, the suppression of extra dissipated energy can be realized by imposing an anti-resonance excitation frequency, the mode shape corresponded will automatically grantee a natural encastre in the middle with relatively weak energy dissipation. In this way, the energy dissipation can be restrained to the controlled area under the bolted clamp.

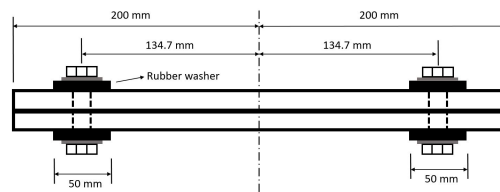


Figure 4.1: Cantilever sandwich beam specimen

The specimen designed is shown in figure 4.1. Two metallic plates are superimposed one on another. Two bolts are positioned with equal distance from the center. Rubber washers are inserted between the metallic washer and the plate for the purpose of a better contact pressure uniformity. Based on the dimensions and properties listed in table 4.1, it is necessary in the first place to find the position of bolted clamp for optimal damping capacity, then obtained position will be brought into the verification for non-interference between the resonance frequency of the whole structure and of the subsystem of bolted clamp.

Total length (mm)	400
Width (mm)	30
Plate thickness (mm)	2
Rubber washer thickness (mm)	5.5
Length of rubber washer (mm)	50
Coefficient of friction (mm)	0.3
Young's modulus of steel (MPa)	210000
Young's modulus of rubber (MPa)	10
Clamp mass (g)	50

Table 4.1: Beam dimensions and mechanical properties

In order to find the optimum position of bolted clamp under a given pressure, it is necessary to determine the maximum force that the rubber washer can support. Rubber is an elastoplastic material whose plastic deformation may cause supplementary energy dissipation, so a strain limit of 10 % is respected in the design. Here we set that the force applied corresponds to a rubber's deformation of 5 %. The pressure on the washer is given by

$$p = E\varepsilon = 0.5 \text{ MPa.} \quad (4.1)$$

The amplitude at which the structure reaches its maximum damping can be obtained by deriving equation 2.36 with respect to modal amplitude q , $\eta'(q) = 0$. The optimal amplitude can thus be written as

$$q_{\eta_{max}} = \frac{8Eh^2l^3pR^2\mu - 48Eh^2l^3pRX_c\mu}{3E^2h^4[R^2 + 12X_c(X_c - 2l)]} - \frac{\sqrt{-2E^2h^4l^3p^2\mu^2R^2(R - 6X_c)[-32l^3(R - 6X_c) + 1728l^2X_c^2 - 144lX_c(R^2 + 12X_c^2) + 3(R^2 + 12X_c^2)^2]}}{3E^2h^4[R^2 + 12X_c(X_c - 2l)]}. \quad (4.2)$$

We impose that the maximum damping takes place when the amplitude reaches 1 mm. By equating the $q_{\eta_{max}}$ to 1 in equation 4.2 and solve for X_c , we can obtain two positions

$$X_{c1} = 0.52 \text{ mm}, \quad X_{c2} = 134.7 \text{ mm.} \quad (4.3)$$

The bolt cannot be placed at X_{c1} since it is too close to the fictive encastre. X_{c2} is chosen to be the optimal position. A parametric study is conducted with the parameters above and the amplitude-damping curve is illustrated in figure 4.2. The position 134.7 mm corresponding to purple curve provides maximum damping at amplitude 1 mm.

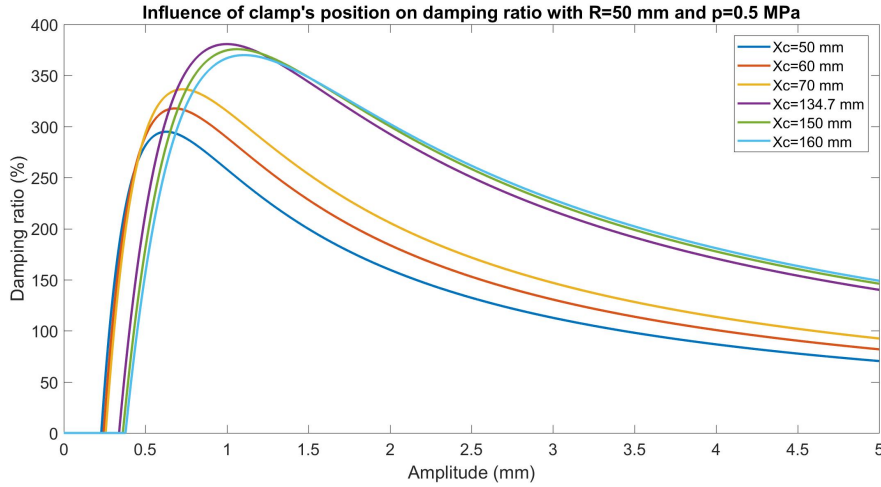


Figure 4.2: Optimal position for maximum damping at $q = 1$ mm

The second part in the set-up design is to verify if there is interference between the whole structure and the subsystem of bolted clamp at resonance frequency, e.g. the resonance of these two systems should not be too close together. The whole system is analyzed by finite element method with a point mass of 50 g at the position of bolt, which is situated at 134.7 mm from the encastre.

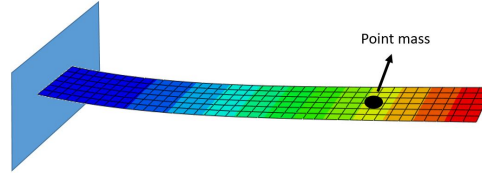


Figure 4.3: Finite element analysis of specimen

Two cases should be taken into account in the frequency analysis: in the first case there is no friction between two plates (the coefficient of friction is zero), they vibrate independently and the point mass is equally shared by the upper and lower part, e.g. the point mass for each plate is 25 g; the second case considers that the coefficient of friction is infinite, the plates can be regarded as perfectly stucked together and the point mass is supported by a plate of doubled thickness. The first resonance frequency with finite coefficient of friction should be within the range defined by these two extreme values.

$f_{\mu=0}$	$f_{\mu=\infty}$
36.487 Hz	72.878 Hz

Table 4.2: Resonance frequencies under $\mu = 0$ and $\mu = \infty$

The subsystem of bolted clamp can be simplified to a spring-mass system as

illustrated in figure 4.4.

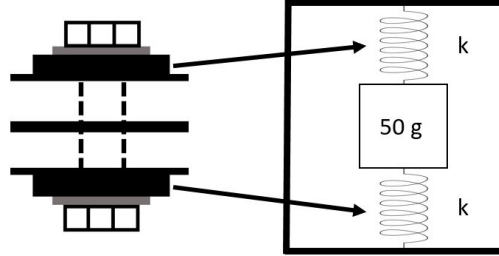


Figure 4.4: Mechanical model of subsystem

The stiffness of the rubber washer can be calculated with the Young's modulus of 10 MPa and the imposed deformation of 5 %.

$$k = \frac{\varepsilon ES}{\varepsilon h} = \frac{0.05 \times 10 \text{ MPa} \times 50 \text{ mm} \times 30 \text{ mm}}{0.05 \times 5.5 \text{ mm}} = 2727 \text{ N/mm} = 2.7 \times 10^6 \text{ N/m}. \quad (4.4)$$

The natural frequency of the subsystem can thus be expressed as

$$f_n = \frac{1}{2\pi} \sqrt{\frac{2k}{m}} = \frac{1}{2\pi} \sqrt{\frac{2 \times 2.7 \times 10^6 \text{ N/m}}{0.05 \text{ kg}}} = 1654 \text{ Hz}. \quad (4.5)$$

The natural frequencies of the two systems are far from each other, so there is no interference between them.

4.3 Measurement system

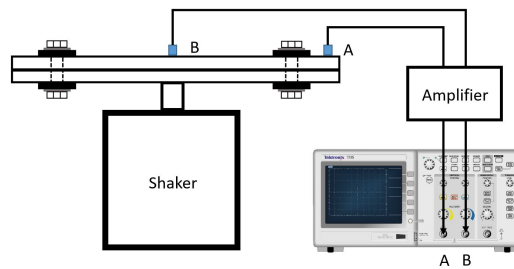


Figure 4.5: Measurement system set-up

The measurement system is illustrated in figure 4.5. Seeing that the fictive encastre is in constant movement under the sinusoidal excitation of shaker, the displacement cannot be simply measured by the accelerometer at position A. In this case, the displacement at point B should be taken into account and the relative displacement between point A and point B is the actual amplitude that we look for. The acceleration at point A and B are respectively noted as two rotational vectors γ_A and γ_B ,

we assume that they are both sinusoidal and that the displacement can be obtained by dividing the acceleration by ω^2 . The vectorial subtraction can give the vector of relative displacement. The maximum projection of the relative displacement vector on x axis is the maximum amplitude for damping calculation.

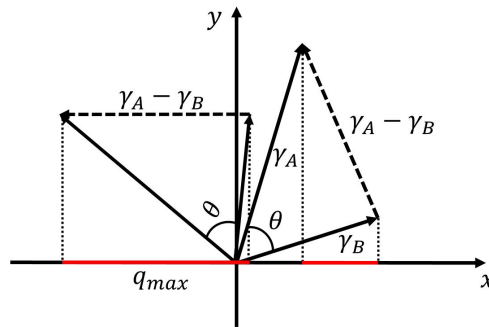


Figure 4.6: Measurement system set-up

The amplitude can thus be written as

$$q = \frac{1}{\omega^2} \|\gamma_{\mathbf{A}} - \gamma_{\mathbf{B}}\|. \quad (4.6)$$

The vectorial subtraction can be easily achieved by analogous signal operation from channel A and channel B in the numeric oscilloscope, as the peak-to-peak value is extracted automatically. A frequency sweeping is applied to the structure under different clamping pressures and shaking intensity, the evolution of displacement obtained will give a clear view of the influence that the pressure and the modal amplitude has on damping.

4.4 Rubber washer's stiffness measurement

In order to estimate the damping property, the clamping pressure on the contact interface must be a known parameter. Since the direct measurement of pressure in such a system is a difficult task, an indirect way to assess the compression force is developed.

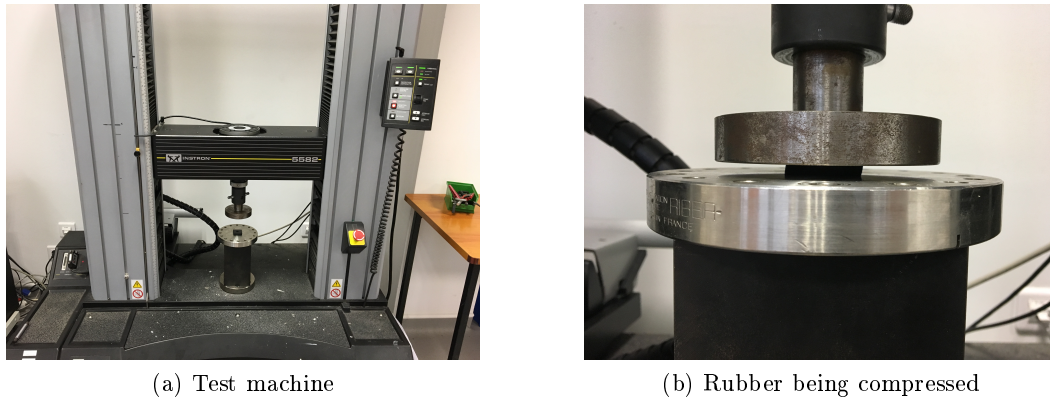


Figure 4.7: Rubber washer's stiffness measurement

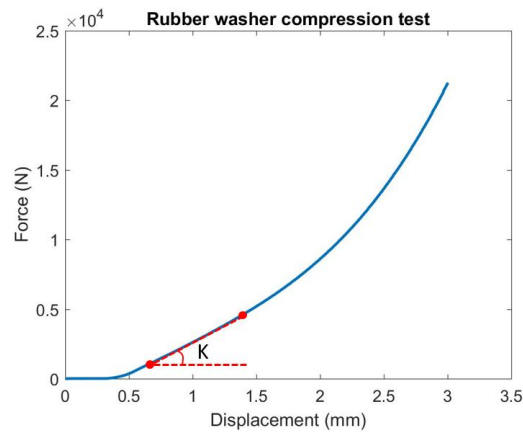


Figure 4.8: Rubber stiffness calculation

Even though the direct measurement of pressure seems unachievable, the compressed distance of the rubber washer can be easily obtained. Once we know the stiffness of the rubber washer, the force applied on the plate can be calculated indirectly by multiplying the compressed distance. The stiffness test was conducted on a traction-compression machine INSTRONTM5582, a maximum compression displacement is fixed at 3 mm. The force-displacement curve obtained is illustrated in figure 4.8. At the beginning of the test, the reaction force is zero due to the existence of gear clearance. The force-displacement curve presents two phases, the first phase is linear which ends at 2 mm, the second phase is in the realm of large displacement and appears to be nonlinear. In the current study, the compression displacement is within the linear phase, whose stiffness can be represented by the slope of the curve.

By picking up two points on the linear part of the curve, the stiffness of the rubber washer is

$$k = \frac{3700 - 1540}{1.221 - 0.7667} = 4754 \text{ N/mm.} \quad (4.7)$$

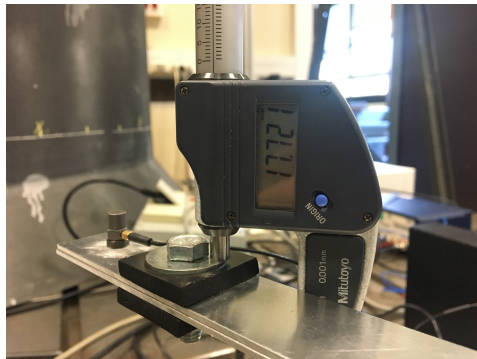
The measured stiffness also justifies the previous interference verification, the actual stiffness is two times bigger than the assumed stiffness, which guarantees that the clamping system moves simultaneously with the vibrating plate and maintains the applied pressure.

4.5 Clamping pressure's calculation

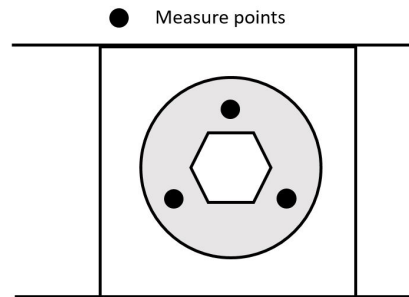
In order to identify the influence of clamping pressure, the application of three different pressures is planned for the experiment. The distance between the two washers is measured by a micrometer. The thickness of each component is listed in the table 4.3.

	Two plates	Metallic washer	Rubber washer
Thickness (mm)	3.98	1.86	5.39

Table 4.3: Components' thickness



(a) Thickness measurement



(b) Measure points

Figure 4.9: Rubber washer's stiffness measurement

The total length of the clamping system with zero pressure is the sum of all the components, which gives 18.48 mm. Since the parallelity between the two washers cannot be guaranteed under the tightened bolt, the distance for pressure calculation is the averaged value of three different points equally positioned on the washer. Three clamping pressures are applied in the experiment. As the structure has two symmetric clamping pads, the pressure finally adopted is the average value of the two clamps.

The pressures on the left clamp is listed in table 4.4.

Case	H_1 (mm)	H_2 (mm)	H_3 (mm)	$Aver.H$ (mm)	Force (N)	Pressure (MPa)
1	17.710	17.685	17.739	17.710	3661	4.06
2	17.996	17.960	17.920	17.960	2472	2.75
3	18.391	18.407	18.460	18.420	285	0.30

Table 4.4: Pressures on the left clamp

The pressures on the right clamp is listed in table 4.5.

Case	H_1 (mm)	H_2 (mm)	H_3 (mm)	$Aver.H$ (mm)	Force (N)	Pressure (MPa)
1	17.719	17.501	17.576	17.600	4184	4.64
2	18.02	17.99	17.879	17.963	2458	2.73
3	18.458	18.204	18.166	18.280	950	1.05

Table 4.5: Pressures on the right clamp

The three different clamping pressures adopted are the average value of the right and the left clamp.

	Case 1 (MPa)	Case 2 (MPa)	Case 3 (MPa)
Pressure	4.35	2.74	0.67

Table 4.6: Pressures chosen

4.6 Dynamic model of seismic system

Since the encastre point B is connected to the shaker and is in constant vibration, the system in figure 4.5 can be interpreted by a dynamic seismic model.

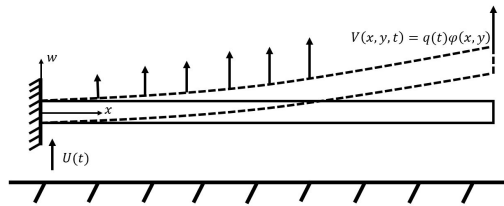


Figure 4.10: Seismic system

The movement of the encastre is denoted as $U(t)$ and this motion is uniform for all the points on the plate. The vibration in the local coordinate system is expressed by the product of the first resonance mode shape and the modal coordinate $q_i(t)\phi_i(x, y)$. The displacement in the fixed coordinate system is written as the superposition of the two movements.

$$w(x, y, t) = U(t) + V(x, y, t). \quad (4.8)$$

The dynamic equilibrium of a plate can be written as

$$\rho \ddot{w}(x, y, t) + D \Delta^2 w(x, y, t) = q(x, y, t) \quad (4.9)$$

where Δ is Laplacian operator whose differential operation is equivalent to $\Delta = \nabla^2$. D is bending rigidity of the plate given by $D = Eh^3/12(1 - \nu^2)$.

Write the displacement field in the modal synthesis form

$$w(x, y, t) = \sum_{i=1}^n q_i(t) \phi_i(x, y) + U(t). \quad (4.10)$$

Substitute equation 4.10 into equation 4.9 with zero exterior force, we can get

$$\rho \sum_{i=1}^n \ddot{q}_i(t) \phi_i(x, y) + D \sum_{i=1}^n q_i(t) \Delta^2 \phi_i(x, y) = -\rho \ddot{U}(t). \quad (4.11)$$

By using Ritz-Galerkin method with the normalized orthogonal mode shape to the mass, multiply equation 4.11 with mode shape $\phi_i(x, y)$ and integrate over the whole calculation domain, the minimized error function can be expressed as

$$\int_{\Omega} D \Delta^2 \phi_i(x, y) \phi_i(x, y) ds q_i(t) + \int_{\Omega} \phi_i(x, y) \rho \phi_i(x, y) ds \ddot{q}_i(t) = - \int_{\Omega} \rho \phi_i(x, y) \ddot{U}(t) ds \quad (4.12)$$

or

$$q_i \ddot{q}_i(t) + \omega^2 q_i(t) = - \int_{\Omega} \rho \ddot{U}(t) \phi_i(x, y) ds. \quad (4.13)$$

The modal force in this case can be regarded as the inertia force introduced into the system by the moving encastre. In order to trace the frequency-response curve, the modal force should remain constant. The expression 4.13 indicates that the acceleration of point B should remain constant for all the sweeping frequencies.

4.7 Alternative method for damping identification

An alternative calculation method of damping value is proposed in the current section. It is based on a curve-fitting method with a simplified mass-spring dynamic model, as illustrated in figure 4.11. The bolted clamps are assimilated to two lumped masses m_A , the stiffness of the plate is simplified as k_A . The mass and stiffness of the shaker is denoted as m_B and k_B .

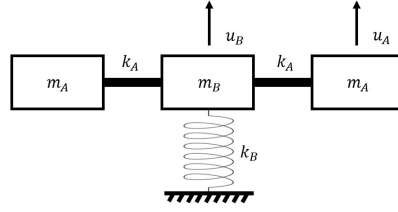


Figure 4.11: Dynamic mass-spring model

The mass and stiffness matrix of the system can be respectively written as

$$\mathbf{M} = \begin{bmatrix} m_A & 0 & 0 \\ 0 & m_B & 0 \\ 0 & 0 & m_A \end{bmatrix}, \quad (4.14)$$

and

$$\mathbf{K} = \begin{bmatrix} k_A & -k_A & 0 \\ -k_A & 2k_A + k_B & -k_A \\ 0 & -k_A & k_A \end{bmatrix}, \quad (4.15)$$

with $k_1 = 12EI/l^3$, l is the distance from the clamp to the excitation point, I is the rotation inertia of the rectangular cross section expressed by $bh^3/12$. The known mass $m_1 = 50$ g. The parameters m_2 and k_2 are still unknown. If hysteresis damping is taken into account by the complex stiffness coefficient $i\eta$, we can express the displacement vector in modal coordinates with mode shapes normalized to the mass matrix. The modal coordinates can thus be solved as

$$q_i = \frac{f_i}{-\omega^2 + \omega_i^2(1 + i\eta)}. \quad (4.16)$$

Since the model amplitude is obtained in a differential system as expressed by equation 4.6, special attention should be paid to the modal force when tracing the frequency-response curve. The dynamic equilibrium of the mass m_A can be written in the following way.

$$m_A \ddot{u}_A + k_A(u_A - u_B) = 0 \quad (4.17)$$

Since the displacement difference $u_A - u_B$ is the studied parameter, it is possible to rewrite equation 4.10 in terms of $Y = u_A - u_B$.

$$\begin{aligned} m_A(\ddot{u}_A - \ddot{u}_B) + k_A(u_A - u_B) &= -m_A \ddot{u}_B \\ m_A \ddot{Y} + k_A Y &= -m_A \ddot{u}_B \end{aligned} \quad (4.18)$$

In order to maintain a constant excitation force with an unchangeable m_A , the acceleration on mass m_B should remain constant, i.e. the acceleration of point B in figure 4.5 is constant for all frequencies in the sweeping. The inertia force $-m_A \ddot{u}_B$

can be regarded as a constant fictive excitation force applied on the lumped mass A in the differential system, which gives the same requirement on excitation force as in equation 4.13.

4.8 Experiment results

In order to trace the frequency-response curve, a frequency sweeping from 20 Hz to 70 Hz with an increment of 1 Hz was applied on the structure. To maintain the constant modal force, the acceleration on the excitation point was adjusted to the same level for each frequency. The objective of the current study is to reveal the relationship between modal amplitude and hysteresis damping, to this end the structure was excited under 7 accelerations from 20 to 80 m/s^2 with an increment of 10 m/s^2 .

The response curve for the case of 4.35 MPa is illustrated in figure 4.12. The resonance frequency is within the realm between 40 Hz and 50 Hz, which is in correlation with the preliminary numerical simulation with zero friction and infinite friction in table 4.2. The curves show that the resonance frequency decreases with an increase in modal amplitude, this phenomenon can be explained by the intuition that under small modal amplitude, the sticking phase is dominant during one complete cycle, so that the participation of stiffness under the configuration of two stucked plates is bigger, the overall stiffness is thus higher. However under big amplitude, the slipping phase is more dominant, the whole structure behaves more as two separate plates whose stiffness is much lower, in this way the resonance frequency will decrease.

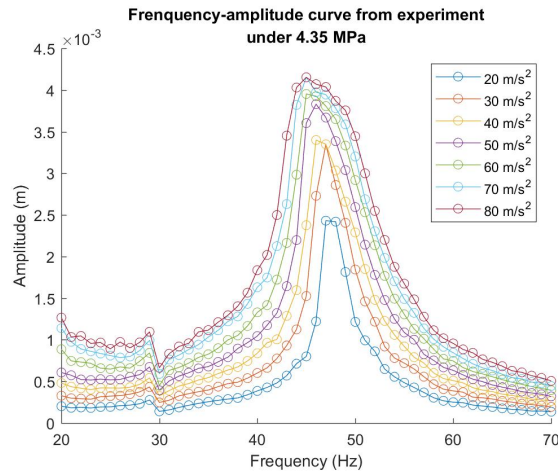


Figure 4.12: Frequency response curve under 4.35 MPa

The same phenomena can be observed in the experiment case with 2.74 MPa and 0.67 MPa. In the case of 0.67 MPa, the maximum acceleration was stopped at

70 m/s² in order not to damage the structure, since under this pressure the damping is very weak.

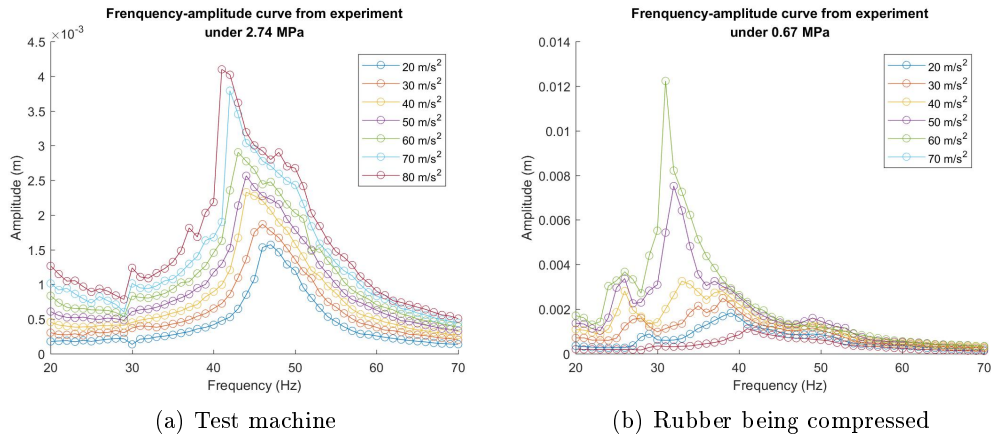


Figure 4.13: Frequency response curve under 2.74 MPa and 0.67 MPa

The the frequency-response curve under 0.67 MPa clearly shows that the vibration behavior of the structure is very similar to that of two separate plates, since the resonance frequency is close enough to $f_{\mu=0}$ in table 4.2, especially under the excitation acceleration of 70 m/s². The preliminary qualitative interpretation of experimental results indicate that the vibration behavior of assembled structures is sensitive to contact friction conditions, the sticking-slipping transition can not only influence the resonance frequency, but also modify the damping property of the structure.

To have a more clarified view on the influence of pressure in the sandwich plate, the next comparison is conducted with the same excitation level but different clamping pressures.

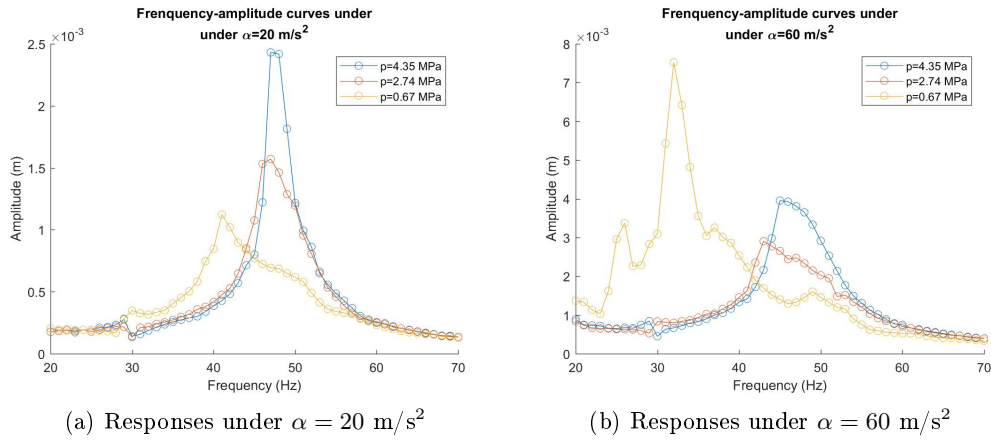


Figure 4.14: Frequency response curve under 2.74 MPa and 0.67 MPa

By comparing figure 4.14a and figure 4.14b, the compounded stiffness is shown to be in positive correlation with the clamping pressure, the structure becomes stiffer with a higher resonance frequency as the clamping force increases. However as to damping capacity, the vibration behaviors suggest that for different excitation forces, there exists different optimal clamping pressures to obtain the most damped response, for example in the case of $\alpha = 20 \text{ m/s}^2$, the pressure 0.67 MPa is proved to be more efficient for energy dissipation, while the pressure 2.47 MPa is qualified as the optimized pressure to reach the highest damping under the excitation of $\alpha = 60 \text{ m/s}^2$. This experimental observation justifies the theoretical deduction that frictional damping is sensitive to clamping pressure.

The damping ratio is calculated by half-power bandwidth method. The amplitude corresponding to a specific damping value is the maximum displacement on the frequency-response curve under a given modal force.

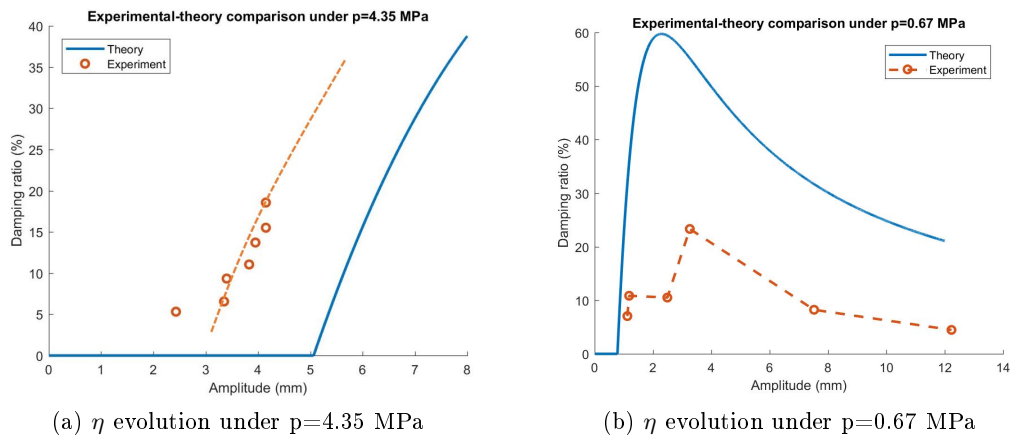


Figure 4.15: Theory-experiment comparison under 4.35 MPa and 0.67 MPa

The comparison between the experimental results and the theory developed in chapter 2 are illustrated in figure 4.15a and figure 4.15b. The comparison case under 4.35 MPa shows that slipping takes place earlier than the theoretical model. This can be explained by the fact that under the real working condition, different from the hypothesis used in the theoretical model, all the points on the contact interface don't slip simultaneously. Some points slip earlier than other points and thus create the partial-slip working condition. Even though not all the points are in the slipping phase, the energy dissipated by the slipping points cannot be neglected, so that the damping appears with a smaller amplitude. The analytical model requires that slipping takes place when the tangential stress reaches saturation for all the contact points, this naturally leads to a bigger amplitude to trigger damping. However, due to the limited power of shaker and the security concern to keep the specimen within the range of rupture, the sandwich plate was not excited to reach the maximum damping, nevertheless, the damping evolution presented by the experiment is in good correlation with the theoretical model: before achieving the damping saturation amplitude, the damping value grows as the amplitude increases.

If the damping value variations under the three different pressures are superimposed on the same figure, the evolution tendency revealed by the analytical model are proved to be reflected by experimental results.

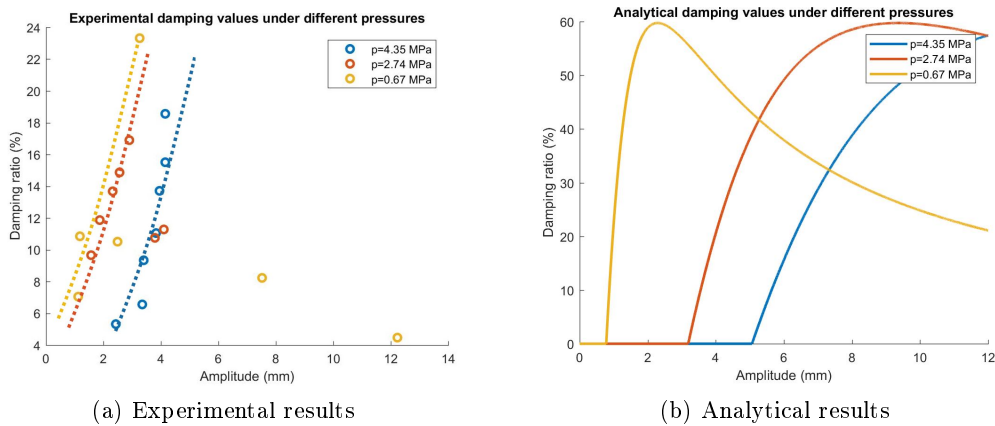


Figure 4.16: Theory-experiment comparison under three different pressures

The experimental results in figure 4.16a justify the analytical predictions. In the first-order damping model, pressure can influence the amplitude beyond which the damping is activated. The amplitude required for maximum damping is also logically increased, so that it can be concluded that bigger clamping pressure will result in a later damping activation, and make the reaching of maximum damping more difficult.

Even though the general damping variation presents the same tendency in both

experiment and analytical derivation, the gap between the two demonstrations are still very large. This error can be contributed by multiple uncertain and uncontrollable parameters. In the real condition, the pressure on the plate is not uniform under the clamping pad, the coefficient of friction is not well measured, and the influence of contact roughness and flatness is not taken into account in the analytical development. All these parameters can cause huge different between experimental verification and theoretical calculation.

4.9 Conclusion

The current section is the experimental verification of the previously developed theories. An academic set-up was designed to quantify the first-order frictional damping in sandwich plate. In order to minimize the influence of encastre fixation, a symmetric structure whose excitation point is situated in the middle was adopted. Since the structure can be assimilated to a seismic system, a constant modal force was guaranteed by maintaining a constant acceleration on the excitation point. Due to the vibrating encastre boundary condition, the absolute modal amplitude in the moving coordinate system was expressed by a subtraction of the two temporal acceleration signals. Three clamping pressures were applied on the sandwich plate to identify its influence on damping activation point. The clamping pressure was derived in an indirect way from the squeezed distance of rubber washer and the measured stiffness in the compression test. The error due to the non-flatness was compensated by an averaging of three points on the washer. For each clamping pressure, different excitation levels were tested to illustrate the variation of damping ratio as a function of modal amplitude.

The frequency-response curves obtained show that the vibration behavior of sandwich plate is strongly nonlinear, the compounded stiffness is sensitive to modal amplitude. For small modal amplitude, the sandwich plate behaves like two stuck-together plates, as the amplitude increases, the stiffness decreases by reason of a more dominant role that the slipping phase plays during the vibration. The experimental results also indicate that the optimal clamping pressure to reach the most damped state depends on the excitation level applied on the structure, the optimal clamping pressure under one modal force may not work for the other. By comparing the experimental results and the analytical models, two frictional damping properties can be confirmed:

- Before reaching the maximum damping value, the damping value increases with the modal amplitude.
- Bigger clamping pressure requires bigger deformation to activate damping and to reach maximum damping capacity.

Even though there presents a certain correlation between experiments and theoretical predictions, the gap separating them cannot be neglected. This is due to the accumulated error in the evaluation of coefficient of friction, clamping pressure and contact surface area. The gap can be minimized if a more sophisticated and feasible measurement method for those parameters is introduced into the test.

Methods for industrial application

Contents

4.1	Introduction	109
4.2	Specimen design	110
4.3	Measurement system	113
4.4	Rubber washer's stiffness measurement	114
4.5	Clamping pressure's calculation	116
4.6	Dynamic model of seismic system	117
4.7	Alternative method for damping identification	118
4.8	Experiment results	120
4.9	Conclusion	124

5.1 Introduction

The design of fatigue endurance is a critical step in product development, especially for automobile and aeronautical industry. A key parameter in fatigue calculation is the stress field in the component, which depends on the displacement's amplitude in vibration, so that an accurate vibrational analysis is the prerequisite for a reliable fatigue design. In the current industrial vibration analysis, the empirical modal damping property is assumed viscous and dependent on speed. For certain cases with the presence of assembled structures, the obtained response with viscous damping doesn't match the experiment. According to the study in chapter 1 and 2, this inconsistency can be explained by the biased understanding of damping property. In assembled structures, there is not only viscous material damping which depends on speed, but also friction-induced damping from the contact surfaces which depends on displacement, the latter may even be 10 to 100 times more dominant. In this section, the modelization method for friction damping in industrial context will be developed from the concept expressed by academic methods, its application method and limitations will be explained.

5.2 Mode shape injection method

Frictional damping is thought to be sensitive to mode shape and modal amplitude. As previously demonstrated on the model of von Kármán plate, the single mode

description of the displacement $q\phi(x, y)$ can be transformed into a in-plane fictive force field as external excitation and it is thus possible to establish the dependency between mode shape and damping ratio. In the case of sandwich plate, the displacement field is transformed into a mid-plane stress field which is then used for the determination of sticking-slipping transition, the relationship between the modal amplitude and the damping ratio can also be obtained by this procedure, hence it is justifiable to infer that the key method to be extracted from the two academic examples is that the modal displacement field should be transformed into some kind of external excitation to generate relative displacement on the contact surface. The induced dissipated energy can be regarded as the damping property of the chosen mode shape.

In real industrial applications, it is difficult to apply the notion of in-plane fictive force field since the contact surface may not be flat and of regular form, so in this case, we propose that the mode shape could be used as an imposed displacement field to generate interface slipping. The clamping pressure can be applied in the prestress step and maintained in the following steps. The illustration of this general idea is presented in figure 5.1. It should be noted that the clamping pressure on the upper plate has no contribution to the contact pressure, since its influence is canceled by the imposed displacement on lower adjacent nodes, the contact pressure is only provided by the lower clamping pressure and is transmitted to the contact surface via the lower plate.

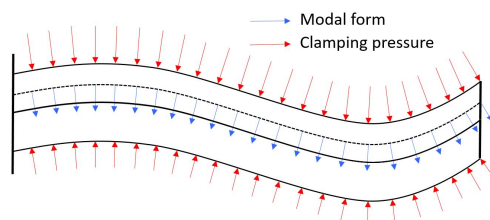


Figure 5.1: Illustration of the load case for industrial application

The imposed displacement field can force the structure to deform in the direction of the mode shape, while the maintained pressure guarantees the contact frictional force, in this way the induced interface relative displacement can contribute to energy dissipation of the whole structure.

Before presenting the solution procedure, two hypothesis are adopted in the industrial application. Firstly, as demonstrated in the experiment, the presence of friction and change in modal amplitude will not result in a drastic modification in resonance frequency and mode shape, accordingly it is reasonable to consider that the mode shape stays constant for all clamping pressures and modal amplitudes, in this way the implementation of single linear mode method is justified. Secondly, the vibration amplitude are considered small compared to the feature size of the

structure, thus the normal vector on the contact surface can be regarded as anchored and unmovable to the initial configuration.

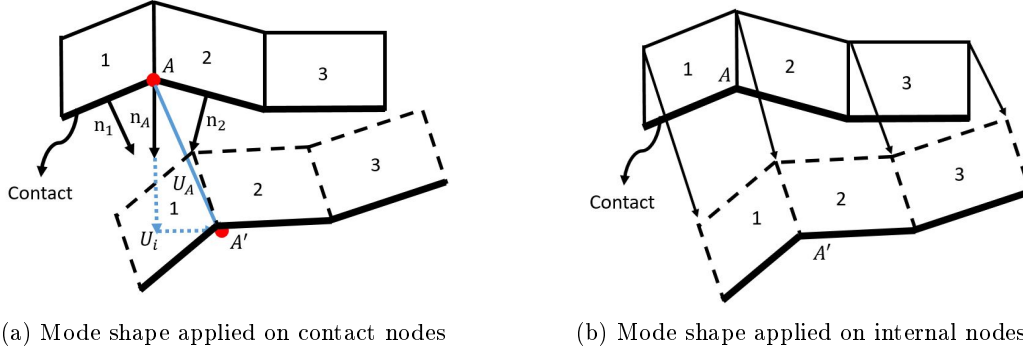


Figure 5.2: Mode shape injection methods

The normal vector of a given contact element can be calculated by the cross product of two non-collinear in-plane vectors. For a contact node that is shared by more than one element, its normal vector is the average of those on surrounding elements, as written by equation 5.1.

$$\mathbf{n}_m = \frac{1}{n} \sum_{i=1}^n \mathbf{n}_i. \quad (5.1)$$

There are two methods for mode shape injection:

1. The mode shape is only projected on the normal direction of contact surface and imposed on contact nodes, as illustrated in figure 5.2a, the mode shape displacement of point A AA' is projected in the direction of n_A .
2. The mode shape is directly applied as imposed displacement on all nodes except those on contact surface and fixed by encastre boundary condition, as illustrated in figure 5.2b.

According to the requirements of the two proposed methods, the imposed displacement is applied to the corresponding DOF by ABAQUSTM subroutine DISP.

$$\mathbf{U}_i = \mathbf{U}_{mode}. \quad (5.2)$$

The reaction force \mathbf{f}_t at a given instant t on the contact nodes can be used for obtaining modal force.

$$q\mathbf{U}_i^T \mathbf{f}_t = qf_{modal} \implies f_{modal} = \mathbf{U}_i^T \mathbf{f}_t, \quad (5.3)$$

where the modal force obtained corresponds to the modal amplitude q .

5.3 Application on infinite flat plate

In order to test the feasibility of the proposed method while keeping a short calculation time, the mode shape injection is in the first place applied on an infinite flat plate. The dimension in the width direction is considered infinite and only the dimension in the length and thickness direction is modeled. The plate is 200 mm in length and 5 mm in thickness, three layers of elements are meshed in thickness direction for a better precision of clamping pressure. The plane strain thickness is fixed at 30 mm.

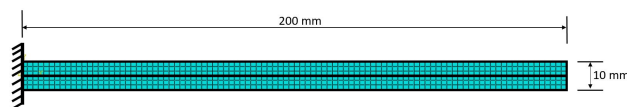


Figure 5.3: Mesh on flat plate

The objective of the current section is to find the relationship between the mode shape and the energy dissipation, as well as its graphical illustration – the form of hysteresis loop. For the convenience of uniform amplification, the mode shape is normalized to displacement, i.e. the biggest value in a mode shape is normalized to 1.

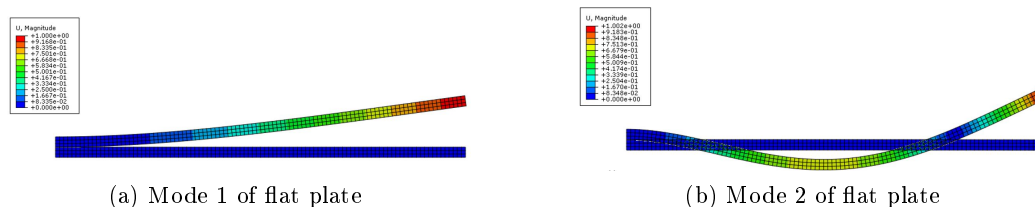


Figure 5.4: Normalized mode shapes to generate interface damping

On the subject of friction property, the coefficient of friction is 0.3, a hard contact is used in the normal direction. As the Coulomb friction law is to be adopted in the current study, the contact elastic slip is suppressed by imposing an admitted elastic sticking distance which is equivalent to $1e-5$ of the characteristic element dimension. In addition, the separation after contact is allowed. Similar to the previous chapters, the calculation is quasi-static with nonlinear geometry. Two loading cycles are applied on the structure, as expressed in equation 5.4, in order to reveal the difference in response between the first loading and the second loading,

$$q = q_{max} \sin(2\pi t), \quad t \in [1, 3] \quad (5.4)$$

where t is the step time.

Before studying the hysteresis property in flat plate, it is necessary to compare the two mode shape injection methods with regards to dissipated energy. If the obtained dissipated energies are of the same magnitude, the two methods can be considered as equivalent. The comparison of the two proposed methods are presented in figure 5.5, the red line corresponds to the method in which the mode shape is imposed on all non-contact nodes in the x and y direction. The blue line corresponds to the case where the mode shape is only projected in the normal direction of the contact surface and applied only on the contact nodes. As indicated in the figure, the case with loading on non-contact nodes has more energy dissipation, but the two methods can be regarded as having the same effect on damping generation. Considering the difficulty in normal vector calculation in case of curved contact surface, the mode injection on non-contact nodes has less limitations and is easier to be applied on complex geometries. In the following study cases, the mode shape is only applied on internal nodes.

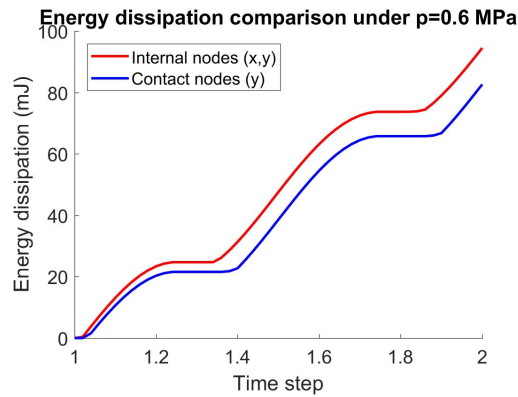
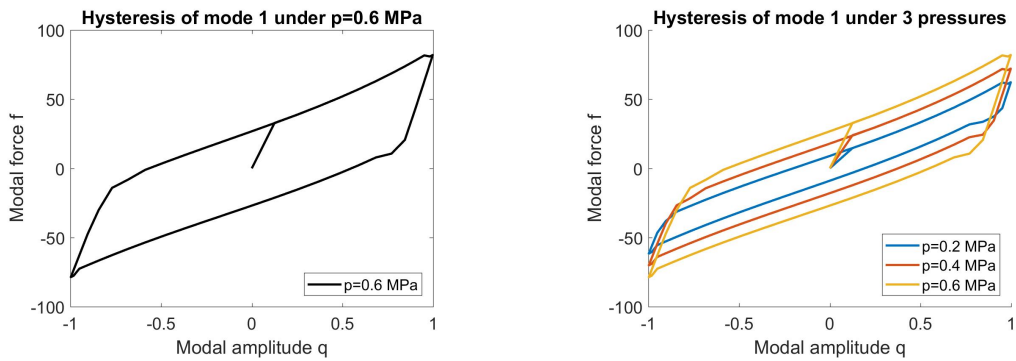


Figure 5.5: Mesh on flat plate

The hysteresis loop is drawn in modal space, with modal amplitude on x axis and modal force on y axis. The modal force is calculated by non-contact node injection method proposed in equation 5.3. The hysteresis loop of the first mode as well as its variation under different pressures are illustrated in figure 5.6a and 5.6b.



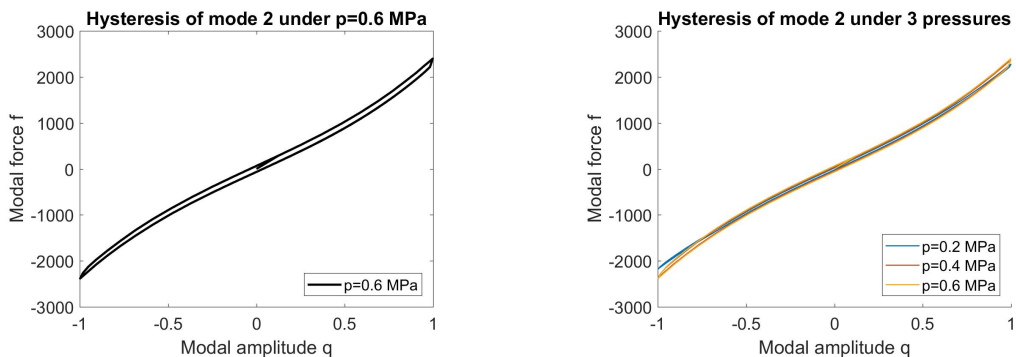
(a) Hysteresis loop of first mode under 0.6 MPa

(b) Hysteresis loop of first mode under 3 pressures

Figure 5.6: Hysteresis loops of first mode

The hysteresis loop in figure 5.6a shows that global stiffness is a function of modal amplitude. When the two plates are stuck together under small modal amplitude, the stiffness is bigger with a steeper slope on the hysteresis curve. As the modal amplitude reaches 0.2, we can notice a significant stiffness drop which implies the beginning of slipping. From the figure 5.6b, we can notice that the slipping arrives later under a bigger clamping pressure, this observation is in correlation with the previous analytical studies. This reduced stiffness will be maintained until the turning point of modal amplitude, on which the structure reenters into the sticking phase and the stiffness regains its value at the beginning of the loading. When the modal amplitude reaches the end of one loading cycle, structure will not reenters into sticking, but keeps the stiffness of slipping phase and starts a new cycle.

The hysteresis loops of second mode are illustrated in figure 5.7a and 5.7b. The much bigger modal force compared to the first mode squeezes the hysteresis loop to a curved line, however it doesn't mean that there is no energy dissipation.



(a) Hysteresis of mode 2 under 0.6 MPa

(b) Hysteresis of mode 2 under 3 pressures

Figure 5.7: Hysteresis loops of second mode

The accumulated energy dissipation can be extracted from the ABAQUSTM .odb file. The evolution of the frictional dissipation for mode 1 and mode 2 under 3 different pressures are illustrated in figure 5.8a and 5.8b. The evolution of accumulated energy dissipation follows the same pattern, the alternative transition between sticking and slipping makes that the evolution is stepwise. In addition, by comparison between the two figures, it is evident that the sticking phase takes a bigger proportion in one cycle under the first mode shape, however its resulting modal force is smaller than that of the second mode under the same modal amplitude. The evolution of dissipated energy also reveals that bigger clamping pressure will result in more dissipated energy and a later slipping activation, but for transition from slipping to sticking during the shift from loading to releasing, both figures show that clamping pressure has no influence on this transition moment, the slipping always stops at the same amplitude whatever pressure is applied. This observation is valid for both mode shapes.

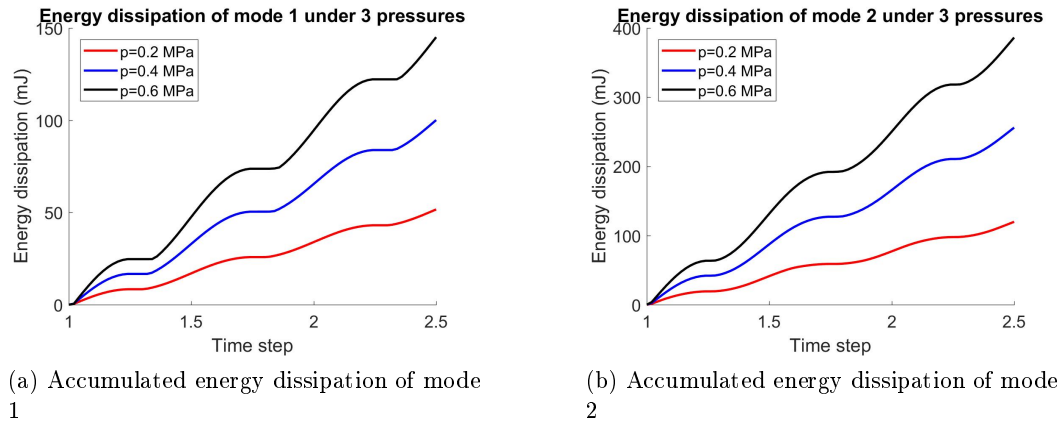


Figure 5.8: Accumulated energy dissipation of mode 1 and mode 2

Another way to estimate dissipated energy is to calculate the area encircled by the hysteresis loop in the modal space. Similar to figure 1.5b, the input and recovered energy can be represented by the loading and unloading curve. For the purpose of calculation time reduction, it is possible to perform only a half cycle of loading, as illustrated in figure 5.9 and the dissipated energy is approximately 50 % of the dissipation in one full cycle, as expressed in equation 5.5.

$$\Delta W = \int_0^T f(q) dq \approx 2 \int_0^{T/2} f(q) dq. \quad (5.5)$$

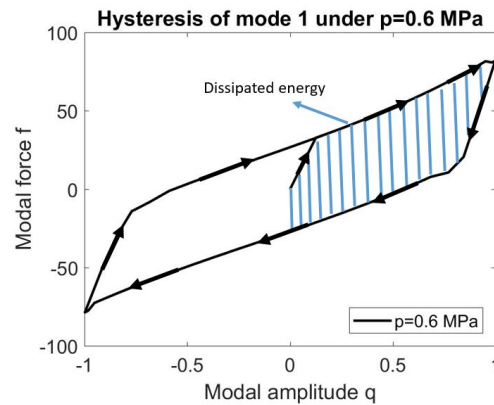


Figure 5.9: Energy dissipation on hysteresis loop

The mode shape injection method is tested with success on the flat infinite plate, the impose of mode shape on non-contact nodes is shown to be able trigger slipping and sticking transition on the contact surface as well as its subsequent energy dissipation. This transformation of linear mode shape into contact nodes' excitation is an applicative embodiment of damping formation from a modal view. The energy dissipation, or the corresponding damping property, is directly associated with the mode shape together with its amplitude, from which the modal nonlinear friction damping can be established. The next section will deal with the damping property of a structure with a slightly more complex geometry.

5.4 Application on infinite curved plate

One of the difficulties in damping modelization is the involvement of complex geometries, curved surface may suggest non-convergence of the calculation. This section will test the robustness of mode shape injection on an infinite plate with an arbitrary curvature. The same with the flat plate, the mesh in the thickness direction also has three layers of elements. The plane strain thickness stays 30 mm.

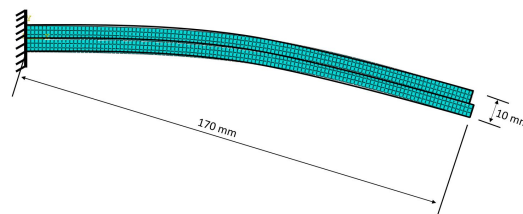


Figure 5.10: Mesh on curved plate

The same with the previous section, the first two linear modes are retained for damping calculation. The mode shapes are illustrated in figure 5.11a and 5.11b. The projected mode shape is only applied on the upper plate.

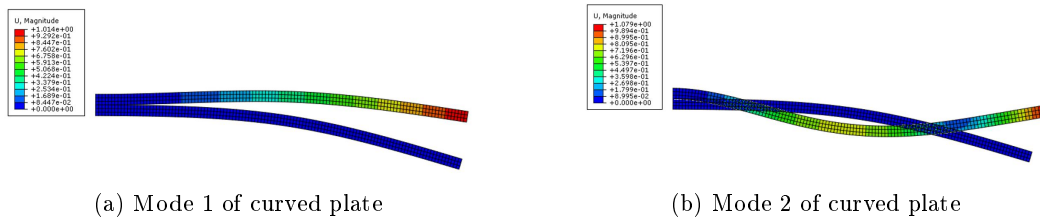


Figure 5.11: Mode shapes of curved infinite plate

The hysteresis loops under the excitation of first and second mode shape are respectively traced in figure 5.12a and 5.12b. The same with the flat plate, the resulting modal force associated with the second mode is much bigger, so that the hysteresis loop is squeezed to a curved line. We also notice that clearance may be created during the loading when the clamping pressure is not big enough.

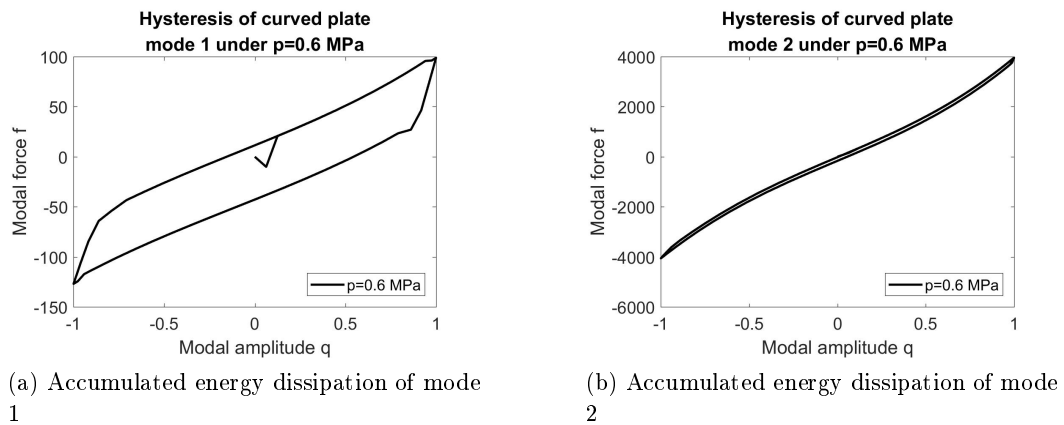


Figure 5.12: Hysteresis loops of curved plate

As regards the accumulation of dissipated energy, the stepwise evolution can also be noted on curved plate in figure 5.13a and 5.13b. Similar to the case of flat plate, the dissipated energy induced by second mode shape is bigger than that of the first mode. The sticking-slipping transition under the pressure of 0.2 MPa is not obvious in both mode shapes, especially in the second mode, this may be caused by the contact separation due to weak clamping pressure.

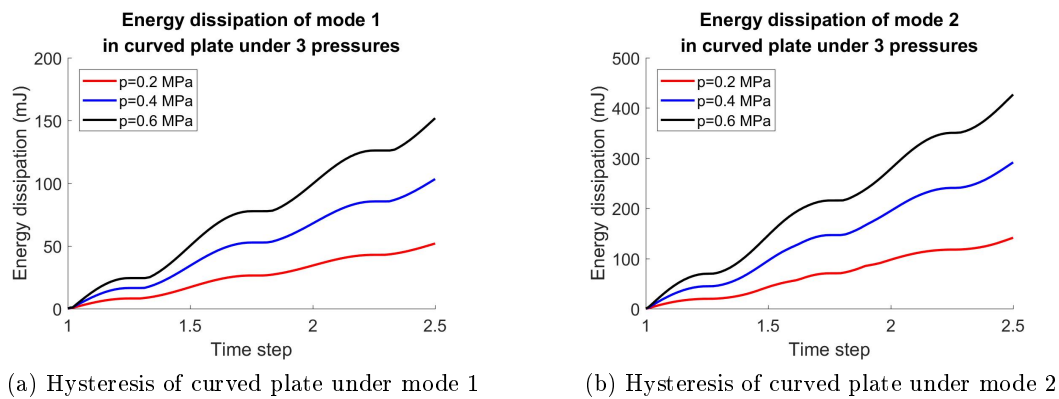


Figure 5.13: Accumulated energy dissipation in curved plate

Based on the test in the current section, the mode shape projection method is shown to be operational on 2D structure with curved contact interface. It is thus prepared to be extended to a 3D structure with more complex mode shapes and contact conditions.

5.5 Application on 3D structure

In order to approximate the geometry in real industrial applications, the mode shape injection method should be tested on 3D structures meshed by hexahedral elements. The geometry of the test model is illustrated in figure 5.14a and 5.14b. The structure is created by extrusion of the cross section to a length of 100 mm.

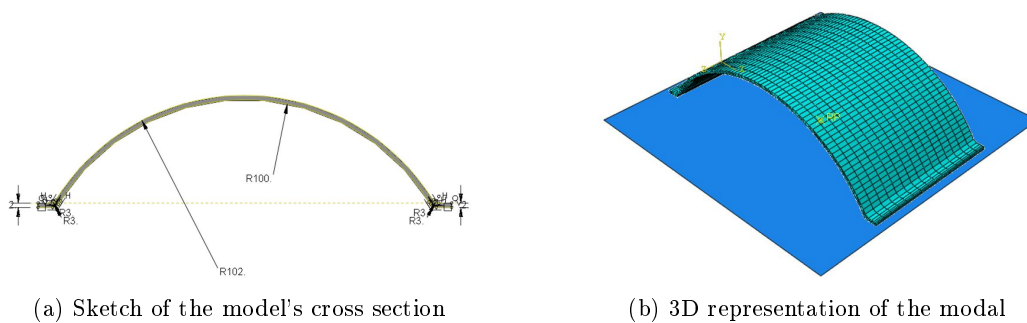


Figure 5.14: Geometry of the 3D model

The blue surface is an analytical rigid plane for contact with the green deformable body. In the ABAQUSTM modeling, the rigid surface must be defined as master surface in the contact modelization. The mode shape to be injected is illustrated in figure and it is only applied on the upper skin for the purposed of calculation time reduction.

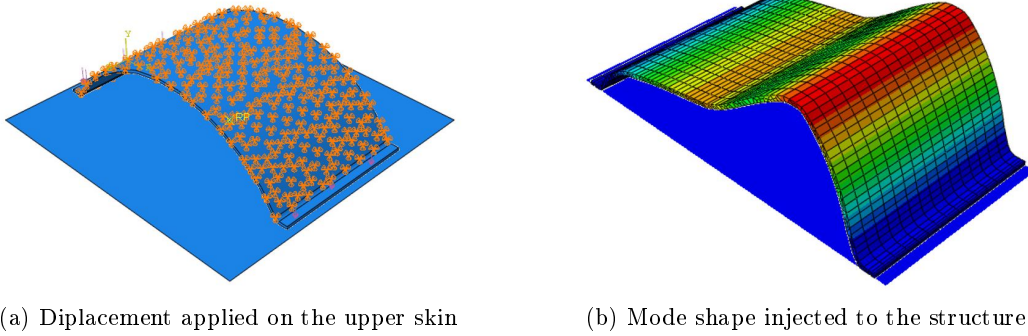


Figure 5.15: Mode shape and imposed displacement region

In the current analysis, the mode shape is normalized to displacement for convenience, but for the response calculation in the frequency domain, the mode shape should be normalized to mass matrix. A sweeping of maximum physical displacement from 0 to 2 mm is applied on the structure, the energy dissipation versus physical amplitude presents the characteristic of first order damping. By the use of curve fitting, the expression of energy dissipation in terms of q can be expressed with 95% confidence bounds as

$$\Delta W = f(q^2, q) = aq^2 + bq = 0.05873q^2 - 0.1725q. \quad (5.6)$$

The damping ratio can thus be written as

$$\eta(q) = \frac{1}{2\pi} \frac{\Delta W}{E_{max}} \approx \frac{0.05873q^2 - 0.1725q}{\pi\omega^2(q/q_{max})^2}. \quad (5.7)$$

where q_{max} is the coefficient between the mode shape normalized to mass and the mode shape normalized to displacement.

$$\phi(x, y, z)_{mass} = q_{max}\phi(x, y, z)_{displacement}. \quad (5.8)$$

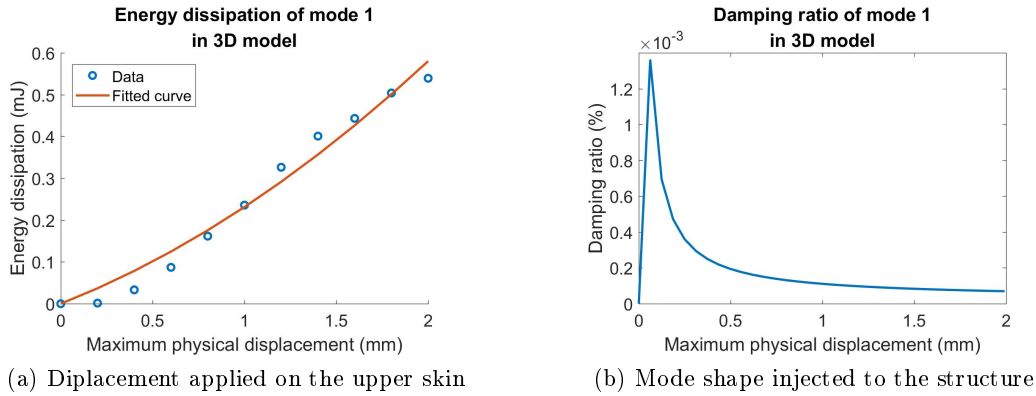


Figure 5.16: Mode shape and imposed displacement region

The equation 5.7 indicates that the damping pressure is not only a function of modal amplitude, but can also be influenced by resonance frequency ω . The weak damping ratio in the current case is due to a very high fist resonance frequency which is 255.09 Hz. The $\eta - q$ curve in figure 5.16b shows that damping ratio will converge to a constant for big modal amplitude.

5.6 Conclusion

The current chapter has proposed an operational method for damping modelization in the industrial context. The method is based on the assumption that the mode shape doesn't encounter significant change compared to linear mode shape with the presence of friction contact. According to the conclusion in Chapter 3 that friction damping is associated with the mode shape and modal amplitude, the mode shape is thus regarded as external excitation to generate contact slipping. The structure is deformed under the pressing of the imposed displacement in the direction of mode shape, the induced energy dissipation on the contact surface implies the damping property associated with the chosen mode shape. From the numerical experiment on 2D sandwich plate, it is found that the choice of DOFs on which the displacements are imposed can influence the energy dissipation. It is recommended to apply the mode shape on internal DOFs in order to avoid the interference with the applied clamping pressure on contact DOFs. The results on 3D structures presents a second-order damping behavior under the excitation of the first mode shape, the energy dissipation can be expressed in an semi-analytical way based on the energy dissipation in the FEM calculations. For complex structures, it is not possible to determine the order number of energy dissipation beforehand, a modal amplitude sweeping is necessary to trace the $\eta - q$ curve.

General conclusion

The modelization of friction damping in assembled structures is one of the major difficulties in vibration mechanics. It has perplexed the automobile engineers of Groupe PSA in terms of fatigue resistance design, since damping is the key factor which regulates the amplitude of vibration with which the fatigue behavior is directly associated. As have been verified by many previous researches, friction damping is more dominant than material damping with an order of 10 to 100 times. So that a reliable estimation of friction damping is critical for a correct vibration calculation and subsequently a competitive design on the market. In order to overcome this engineering problem, a scientific research project has been launched and constitutes the subject of the current thesis.

Friction-induced damping is considered to be independent of frequency but dependent on displacement, which differentiates it from viscous damping. The studies on friction damping can be divided into two categories: analytical modelization and numerical simulation. The analytical modeling is more direct in revealing the basic quantity relationship between controlling parameters, but it is limited to simple structures. Numerical simulation can on the contrary deal with omplex geometries but the calculation is time-costing. The previous works based on these two methods have both pointed out the displacement dependency of friction damping and that it is sensitive to parameters like clamping pressure or internal stress field. The studies in the current research have followed the two modeling methods in the literature and have applied them to more complex phenomena.

Three analytical models have been proposed for the purpose of the elucidation of energy dissipation mechanism in simple jointed structures. Based on the order of modal amplitude q in the expression of energy dissipation, the frictional damping is categorized into first-order damping and second-order damping. The first-order damping is present in the model of sandwich plate and rotational joint, the second-order damping exists only in the von Kármán plate. The order of damping implies the possibility of damping optimization. For example in the first-order damping, there exists an optimal modal amplitude under a given pressure to achieve the maximum damping value. There are also interesting discoveries like the optimal bolt position for a partially clamped plate or the optimum thickness ratio in a sandwich structure. However, there is no optimal displacement in the second-order damping model, since the damping value will increase monotonically with the modal amplitude. All the phenomenological studies have unified the different

damping models under the same objective function—the $\eta - q$ curve and have laid a theoretical foundation for numerical studies as well as industrial applications.

Another important part of the current thesis is dedicated to the numerical solution of von Kármán plate with friction boundary. Due to the difficulty of non-linearity in the continuous formulation, FEM and FDM are employed to discretize the calculation domain. With the introduction of fictive-force field, a 3D problem is planarized and the response of the plate can be solved in a quasi-static way. The in-plane force field is shown to play a critical role in the hardening/softening of the structure. It is found that if the two opposite boundaries are encastred, the structure is under a hardening effect with an increase in modal amplitude, however if one boundary is subjected to dry friction, the stiffness decreases if the clamped boundary is released for slipping. Furthermore, the nonlinear mode coupling is analyzed with the help of multi-mode method. The participation factor of higher order modes is shown to be a function of modal amplitude. For small amplitude, the participation of other modes is weak and the main mode shape can be considered as unchanged. This conclusion justifies the use of single mode method for industrial applications.

The experimental verification is also conducted in the current study. A symmetric sandwich beam is used for damping measurement under different clamping pressure. Even though there is no perfect correlation with the theoretical estimation, the experimental results have shown the same damping evolution tendency with the analytical model, i.e. the optimal damping can be influenced by the clamping pressure and bigger clamping pressure requires a bigger modal amplitude to reach maximum damping.

The methods for industrial application is developed in the ABAQUSTM environment. The simplified single mode method is realized by the subroutine DISP which imposes the mode shape on internal DOFs to generate relative slip on the contact surface. The displacement imposing is shown simple and efficient for a coarse-grained estimation of energy dissipation associated with a given mode shape. But there are still potential improvements that can be expected. The calculation time on 3D structures is still very long, if the model size continues to increase, the time spend by the current method will be unbearable. The optimization in the reading of the mode shape file can be a future direction. In addition, the interference between the displacement imposing and the application clamping pressure is not well understood, for the purpose of a faster and more reliable estimation of energy dissipation, the search for optimal displacement-imposing DOFs can be the subject for future research.

The current thesis gives a complete study on dry friction damping in assembled structures from literature review to real applications by passing through analytical modelings and numerical simulations. The basic properties of dry friction damping

are elucidated and a simplified method is proposed for industrial usage. I hope my work can contribute to the understanding of dynamic complexity of dry friction damping and inspire more in-depth research in this domain.

Second order derivatives schemes

	$\frac{\partial^2 w}{\partial x^2}$	$\frac{\partial^2 w}{\partial y^2}$	$\frac{\partial^2 w}{\partial x \partial y}$
Encastre	$\frac{w_{i+1,j}^2}{dx^2}$	0	0
Friction	$\frac{w_{i-1,j}^2}{dx^2}$	0	0
Upper free nodes	$\frac{w_{i+1,j} - 2w_{i,j} + w_{i-1,j}}{dx^2}$	0	$\frac{\partial_y w_{i+1,j} - \partial_y w_{i-1,j}}{2dx}$
Lower free nodes	$\frac{w_{i+1,j} - 2w_{i,j} + w_{i-1,j}}{dx^2}$	0	$\frac{\partial_y w_{i+1,j} - \partial_y w_{i-1,j}}{2dx}$
Other nodes	$\frac{w_{i+1,j} - 2w_{i,j} + w_{i-1,j}}{dx^2}$	$\frac{w_{i,j+1} - 2w_{i,j} + w_{i,j-1}}{dy^2}$	$\frac{w_{i+1,j+1} - w_{i+1,j-1} - w_{i-1,j+1} + w_{i-1,j-1}}{4dxdy}$

Table A.1: Second order derivatives schemes

List of publications

International Journals

- **Y. Yang**, L. Jézéquel, O. Dessombz, P. Bristiel, O. Sauvage (2019), Modelization of boundary friction damping induced by second-order bending strain. Journal of Sound and Vibration, 446 (2019) 113-128.

International Conferences

- **Y. Yang**, L. Jézéquel, Experimental verification of nonlinear damping induced by slipping interfaces, EngOpt 2018, 17-19 September 2018, Lisbon, Portugal.
- **Y. Yang**, L. Jézéquel, Parametric study of frictional damping in jointed beams, COMPDYN 2017, 15-17 June 2017, Rhodes Island, Greece.

Bibliography

- [1] Nicolas Merlette. *Amortissement des caisses automobiles par des films minces viscoélastiques pour l'amélioration du confort vibratoire*. PhD thesis, Ecully, Ecole centrale de Lyon, 2005. (Cited on page 6.)
- [2] Singiresu S Rao. *Mechanical vibrations fifth edition*. miami: Pearson education, 2011. (Cited on pages 8 and 10.)
- [3] Masami Masuko, Yoshimi Ito, and Keizo Yoshida. Theoretical analysis for a damping ratio of a jointed cantibeam. *Bulletin of JSME*, 16(99):1421–1432, 1973. (Cited on pages 10 and 15.)
- [4] HGD Goyder, DPT Lancereau, P Ind, and D Brown. Friction and damping associated with bolted joints: results and signal processing. In *Proceedings of the ISMA 2016 International Conference on Noise and Vibration Engineering, Leuven*, 2016. (Cited on page 11.)
- [5] Hugh Goyder, Philip Ind, and Daniel Brown. Development of a method for measuring damping in bolted joints. In *ASME 2011 International Design Engineering Technical Conferences and Computers and Information in Engineering Conference*, pages 1253–1262. American Society of Mechanical Engineers, 2011. (Cited on page 12.)
- [6] Hugh Goyder, Philip Ind, and Daniel Brown. Measurement of damping in bolted joints. In *ASME 2012 International Design Engineering Technical Conferences and Computers and Information in Engineering Conference*, pages 399–408. American Society of Mechanical Engineers, 2012. (Cited on page 12.)
- [7] Hugh Goyder, Philip Ind, and Daniel Brown. Measurement of damping due to bolted joints. In *ASME 2013 International Design Engineering Technical Conferences and Computers and Information in Engineering Conference*, pages V008T13A017–V008T13A017. American Society of Mechanical Engineers, 2013. (Cited on page 12.)
- [8] DJ Mead and DCG Eaton. Interfacial damping of riveted joints. Technical report, Report, 1960. (Cited on page 13.)
- [9] Ashkan Hashemi, Reza Masoudnia, and Pierre Quenneville. A numerical study of coupled timber walls with slip friction damping devices. *Construction and Building Materials*, 121:373–385, 2016. (Cited on page 13.)
- [10] LE Goodman and JH Klumpp. Analysis of slip damping with reference to turbine blade vibration. *Journal of Applied Mechanics*, 23(2):421–429, 1956. (Cited on page 13.)

- [11] D Williams. Method of damping out bending vibrations of beam-like structures by dry (or coulomb) friction. *Journal of Mechanical Engineering Science*, 2(2):77–87, 1960. (Cited on page 13.)
- [12] SWE Earles. Theoretical estimation of the frictional energy dissipation in a simple lap joint. *Journal of mechanical engineering science*, 8(2):207–214, 1966. (Cited on page 14.)
- [13] Nobuhiko Nishiwaki, Masami Masuko, Yoshimi Ito, and Ichiro Okumura. A study on damping capacity of a jointed cantilever beam: 1st report; experimental results. *Bulletin of JSME*, 21(153):524–531, 1978. (Cited on page 15.)
- [14] Nobuhiko Nishiwaki, Masami Masuko, Yoshimi Ito, and Ichiro Okumura. A study on damping capacity of a jointed cantilever beam: 2nd report, comparison between theoretical and experimental values. *Bulletin of JSME*, 23(177):469–475, 1980. (Cited on page 15.)
- [15] Scott W Hansen and Ruben D Spies. Structural damping in laminated beams due to interfacial slip. *Journal of sound and vibration*, 204(2):183–202, 1997. (Cited on page 16.)
- [16] Herbert Hirsch Gould and Borivoje Budimira Mikic. Areas of contact and pressure distribution in bolted joints. *Journal of Engineering for Industry*, 94(3):864–870, 1972. (Cited on page 16.)
- [17] HH Ziada and EL LATIF ABD. Load, pressure distribution and contact area in bolted joints. *Institution of Engineers(India), Journal, Mechanical Engineering Division*, 61:93–100, 1980. (Cited on page 16.)
- [18] BK Nanda and AK Behera. Study on damping in layered and jointed structures with uniform pressure distribution at the interfaces. *Journal of Sound and Vibration*, 226(4):607–624, 1999. (Cited on pages 16 and 30.)
- [19] JE Shigley. *Machine design*, 1956. (Cited on page 16.)
- [20] O Damisa, VOS Olunloyo, CA Osheku, and AA Oyediran. Static analysis of slip damping with clamped laminated beams. *European Journal of Scientific Research*, 17(4):455–476, 2007. (Cited on page 17.)
- [21] BK Nanda. Study of the effect of bolt diameter and washer on damping in layered and jointed structures. *Journal of Sound and Vibration*, 290(3-5):1290–1314, 2006. (Cited on page 17.)
- [22] O Damisa, VOS Olunloyo, CA Osheku, and AA Oyediran. Dynamic analysis of slip damping in clamped layered beams with non-uniform pressure distribution at the interface. *Journal of Sound and Vibration*, 309(3-5):349–374, 2008. (Cited on page 17.)

- [23] Bhagat Singh and Bijoy Kumar Nanda. Identification of damping mechanism in layered and welded structures. *International Journal of Mechanical Sciences*, 63(1):37–47, 2012. (Cited on page 17.)
- [24] Bhagat Singh and Bijoy Kumar Nanda. Dynamic analysis of damping mechanism in welded multilayered mild steel beams. *Aerospace Science and Technology*, 29(1):58–73, 2013. (Cited on page 17.)
- [25] L Jezequel. Structural damping by slip in joints. *Journal of vibration, acoustics, stress and reliability in design*, 105(81):497–504, 1983. (Cited on page 18.)
- [26] Earl H Dowell. Damping in beams and plates due to slipping at the support boundaries. *Journal of Sound and Vibration*, 105(2):243–253, 1986. (Cited on page 19.)
- [27] WE Whiteman and AA Ferri. Displacement-dependent dry friction damping of a beam-like structure. *Journal of Sound and Vibration*, 198(3):313–329, 1996. (Cited on page 19.)
- [28] N Peyret, J-L Dion, G Chevallier, and Pierre Argoul. Micro-slip induced damping in planar contact under constant and uniform normal stress. *International Journal of Applied Mechanics*, 2(02):281–304, 2010. (Cited on page 20.)
- [29] Nicolas Peyret. *Dissipation de l'énergie mécanique dans les assemblages: effet du frottement en sollicitation dynamique*. PhD thesis, Université Paris-Est, 2012. (Cited on page 20.)
- [30] S Bograd, P Reuss, A Schmidt, L Gaul, and M Mayer. Modeling the dynamics of mechanical joints. *Mechanical Systems and Signal Processing*, 25(8):2801–2826, 2011. (Cited on page 21.)
- [31] Christian Ehrlich, André Schmidt, and Lothar Gaul. Microslip joint damping prediction using thin-layer elements. In *Dynamics of Coupled Structures, Volume 1*, pages 239–244. Springer, 2014. (Cited on page 21.)
- [32] L Gaul and J Lenz. Nonlinear dynamics of structures assembled by bolted joints. *Acta Mechanica*, 125(1-4):169–181, 1997. (Cited on page 21.)
- [33] Sergey Bograd, André Schmidt, and Lothar Gaul. Joint damping prediction by thin layer elements. *Proceedings of the IMAC 26th Society of Experimental Mechanics Inc. Bethel, CT*, 2008. (Cited on page 21.)
- [34] Eric E Ungar. Energy dissipation at structural joints; mechanisms and magnitudes. Technical report, BOLT BERANEK AND NEWMAN INC CAMBRIDGE MA, 1964. (Cited on pages 24 and 26.)
- [35] Jerome Montgomery. Methods for modeling bolts in the bolted joint. In *ANSYS User's Conference*, volume 5. Orlando, 2002. (Cited on page 24.)

- [36] Alexandra Korolija. Fe modeling of bolted joints in structures, 2012. (Cited on page 24.)
- [37] Matthew Oldfield, Huajiang Ouyang, and John E Mottershead. Simplified models of bolted joints under harmonic loading. *Computers & Structures*, 84(1-2):25–33, 2005. (Cited on page 24.)
- [38] Jeong Kim, Joo-Cheol Yoon, and Beom-Soo Kang. Finite element analysis and modeling of structure with bolted joints. *Applied mathematical modelling*, 31(5):895–911, 2007. (Cited on page 24.)
- [39] Norman Knight, Dawn Phillips, and Ivatury Raju. Simulating the structural response of a preloaded bolted joint. In *49th AIAA/ASME/ASCE/AHS/ASC Structures, Structural Dynamics, and Materials Conference, 16th AIAA/ASME/AHS Adaptive Structures Conference, 10th AIAA Non-Deterministic Approaches Conference, 9th AIAA Gossamer Spacecraft Forum, 4th AIAA Multidisciplinary Design Optimization Specialists Conference*, page 1842, 2008. (Cited on page 25.)
- [40] Yu Luan, Zhen-Qun Guan, Geng-Dong Cheng, and Song Liu. A simplified nonlinear dynamic model for the analysis of pipe structures with bolted flange joints. *Journal of Sound and Vibration*, 331(2):325–344, 2012. (Cited on page 25.)
- [41] Eiji Shamoto, Yohei Hashimoto, Miki Shinagawa, and Burak Sencer. Analytical prediction of contact stiffness and friction damping in bolted connection. *CIRP Annals-Manufacturing Technology*, 63(1):353–356, 2014. (Cited on page 25.)
- [42] W Chen and Xiaomin Deng. Structural damping caused by micro-slip along frictional interfaces. *International Journal of Mechanical Sciences*, 47(8):1191–1211, 2005. (Cited on page 25.)
- [43] MA Scavullo and DG Stephens. Investigation of air damping of circular and rectangular plates, a cylinder, and a sphere. 1965. (Cited on page 26.)
- [44] WS Griffin, Herbert H Richardson, and S Yamanami. A study of fluid squeeze-film damping. *Journal of Basic Engineering*, 88(2):451–456, 1966. (Cited on page 26.)
- [45] LD Landau, EM Lifshitz, Fluid Mechanics, and Pergamon Press. Massachusetts, 1959. (Cited on page 26.)
- [46] Gideon Maidanik. Energy dissipation associated with gas-pumping in structural joints. *The Journal of the Acoustical Society of America*, 40(5):1064–1072, 1966. (Cited on page 26.)
- [47] Minhong Bao, Heng Yang, Hao Yin, and Yuancheng Sun. Energy transfer model for squeeze-film air damping in low vacuum. *Journal of Micromechanics and Microengineering*, 12(3):341, 2002. (Cited on page 27.)

-
- [48] MM Altuğ Bıçak and MD Rao. Analytical modeling of squeeze film damping for rectangular elastic plates using green's functions. *Journal of Sound and Vibration*, 329(22):4617–4633, 2010. (Cited on page 28.)
- [49] Robert B Darling, Chris Hivick, and Jianyang Xu. Compact analytical modeling of squeeze film damping with arbitrary venting conditions using a green's function approach. *Sensors and Actuators A: Physical*, 70(1-2):32–41, 1998. (Cited on page 28.)
- [50] Giorgio De Pasquale, Timo Veijola, and Aurelio Somà. Modelling and validation of air damping in perforated gold and silicon mems plates. *Journal of Micromechanics and Microengineering*, 20(1):015010, 2009. (Cited on page 28.)
- [51] R.M. Kirby and Z. Yosibash. Solution of von-kármán dynamic non-linear plate equations using a pseudo-spectral method. *Computer Methods in Applied Mechanics and Engineering*, 193(6):575 – 599, 2004. (Cited on page 54.)
- [52] Xingrong Huang. *Optimization of dynamic behavior of assembled structures based on generalized modal synthesis*. Theses, Université de Lyon, November 2016. (Cited on page 78.)